Ingvild Bjerke

Parvalbumin Positive Basket Terminals in Layer II of the Rat Medial Entorhinal Cortex: Postnatal Development Studied by Immuno-electron Microscopy

Master's thesis in Neuroscience
Supervisor: Nina Berggaard
Trondheim, June 2016

Norwegian University of Science and Technology
Faculty of Medicine
Department of Neuroscience

Acknowledgements

The work presented in this thesis was conducted at the Cellular and Molecular Imaging Core Facility, NTNU.

A heartfelt thanks goes to my supervisor Nina Berggaard, PhD fellow in the EM-lab. All the practical work for this thesis was done in close collaboration with her. I am immensely thankful for all your help, advice and encouragement throughout this entire process, but not least for your cheerful presence.

I also want to thank professor Johannes van der Want for allowing me this journey through science, for all your advice, and for always being so enthusiastic and supportive.

My thanks also go to Nan Skogaker and Linh Hoang, for patiently training me in the lab and for your excellent technical advice during the project. Also, I would like to thank Gunnar Kopstad and Gro Møkkelgjerd at the EM-lab for always being so positive and helpful.

I also owe a great thank you to my best friend, study buddy, and fellow master student on this project, Anna Paulsen. Thank you for keeping me happy and (somewhat) sane, for always complimenting my work (even when I don't deserve it), and for all the interesting discussions during the analysis and interpretation of the data. The roller-coaster ride that has been this thesis would not have been half as memorable without you.

Lastly, my gratitude goes to to my parents and my two sisters, for always listening to my endless monologues about this project when I suspect you might not find it as interesting as I do. Also, your unconditional faith in my abilities have been of immense value throughout this year.

Abstract

Layer II (LII) of the adult medial entorhinal cortex (MEC) is highly involved in making up animals' sense of space, and the intrinsic wiring of this network is thought to underlie the very specific firing patterns of its constituent cells. A key component of this network is the parvalbumin positive (PV+) basket cell, which provides rapid inhibition of local principal cells by targeting their perisomatic region, thus making them intimately involved in regulating the spatial codes of these cells. Also, PV+ basket cells target other interneurons in the local network. Because information about how these connections are refined is scarce, the current study was undertaken to investigate the ultrastructural and cytochemical development of the local output from LII PV+ basket cells. After establishing satisfactory protocols, brains from rats of postnatal day (P) 10, P15 and P30 were immunostained for PV and investigated at the light- and electron microscopic level. The results show that while PV+ cells are already abundant in LII of the MEC at P10, their local connectivity changes considerably over the next couple of weeks. First, the density of PV+ somatic terminals increases significantly between P10 and P15, but then decreases from P15 to P30. Secondly, the boutons themselves change in several respects: their size displays a U shaped trend across age groups; in terms of shape, they get more ellipsoid after P10; and the number of mitochondria increases significantly after P15. The extensive maturation of these features thus mainly occurs between P15 and P30. These results indicate that PV+ boutons in LII of the developing rat MEC undergo periods of overshoot and pruning, with concurrent strengthening of remaining terminals during the latter phase.

Table of contents

Abbreviations

General

CA	Cornu ammonis
Ca^{2+}	Calcium
CALB+	Calbindin positive
Cl^-	Chloride
CNS	Central nervous system
DG	Dentate gyrus
EC	Entorhinal cortex
EM	Electron microscope
FS	Fast spiking
GABA	γ-amino butyric acid
HD	Head direction cell
HF	Hippocampal formation
HR	Hippocampal region
L	Layer
LM	Light microscope
LEC	Lateral entorhinal cortex
MEC	Medial entorhinal cortex
P	Postnatal day
PaS	Parasubiculum
PER	Perirhinal cortex
PHR	Parahippocampal region
POR	Postrhinal cortex
PrS	Presubiculum
PV+/-	Parvalbumin positive/negative
Reelin+	Reelin positive
Sub	Subiculum

Chemicals and antibodies

ABC	Avidin-biotin complex
DAB	3,3-diaminobenzidine
GA	Glutaraldehyde
PB	Phosphate buffer
PBS	Phosphate buffered saline
PFA	Paraformaldehyde
PV	Parvalbumin
NHS	Normal horse serum
TrX	Triton X-100

1 Introduction

One of the most astonishing features of the brain is the exquisite specificity of intrinsic and extrinsic connectivity of neural networks. A notable example of such a network is the one found in layer II (LII) of the medial entorhinal cortex (MEC). The MEC, together with surrounding areas of the hippocampal region (HR), is highly involved in making up the brain's sense of space (O'Keefe & Dostrovsky 1971; Hafting et al. 2005; Boccara et al. 2010; Moser et al. 2014), thus helping fulfil a pivotal task for all animals. From a bat's flying hunt to a mouse locating its nest; from a rat scavenging for food to your mother picking you up at a friend's place – the everyday tasks of our own and of numerous other diverse species converge on their dependence of this sense of space. Knowing that this ability arises from several interconnected and meticulously organized circuits in the brain, an intriguing question becomes how the specificity of their connectivity is achieved through development. Understanding the details of the developmental processes that lead to adult connectivity will be indispensable in understanding the functioning and premises of that network.

1.1 The rat CNS develops extensively during the first postnatal month

During the early developmental stages of the central nervous system (CNS), hard-wired molecular cues guide the growth and migration of cells and axons, as well as initial synaptogenesis. Rearrangement and pruning of synapses in an experience-dependent manner is then needed to build the highly specific connectivity patterns seen in adults.

1.1.1 Early postnatal development

In rodents, neurogenesis is generally completed by the time of birth (Bayer 1980; Caviness et al. 1995; Takahashi et al. 1995), although these early neurons are far from mature. Notably, γ-amino butyric acid (GABA)-ergic neurons are formed prior to glutamatergic ones (Soriano et al. 1986). Later, these cells will come to form the major inhibitory and excitatory cell types of the CNS. There are two important consequences of their sequential development: (1) GABAergic synapses are established prior to glutamatergic ones, and (2) GABAergic cells are themselves the target of these early synapses (Tyzio et al. 1999; Hennou et al. 2002; Gozlan & Ben-Ari 2003). The synaptogenesis onto both GABAergic and glutamatergic cells, although occurring earlier in the case of the former, further follows a sequential pattern: the dendrites are

targeted first and the somatic regions only later. These processes are thought to be guided by hard-wired molecular cues and take place perinatally in rodents (Tyzio et al. 1999).

Ultrastructurally, neurons change in many respects during the first three postnatal weeks (Miller & Peters 1981). There are several changes in the cytoplasmic content of the cell during this period, leading to a far richer amount of organelles. Small somatic spines are often seen between postnatal day (P) 9 and P12, but are rare from P15 onwards. An important change is the increased size of the cell body and nucleus, which in rodents mainly takes place during the second and third week of life (Eayrs & Goodhead 1959; Miller 1981; Miller & Peters 1981). Interestingly, Tyzio and colleagues (1999) demonstrated that growth and morphological development of cells correlated with the types of input they received, so that a cell only receive glutamatergic input when it displays an apical dendrite.

How can the nervous system grow at the earliest postnatal stages when only GABAergic cells are active? An important feature of the most immature nerve cells is that they react to GABA stimulation with depolarization (Ben-Ari et al. 1989), often including a transient increase in calcium (Ca^{2+})-levels (Ganguly et al. 2001). The reason for this is that immature cells have a higher intracellular than extracellular concentration of chloride ions (Cl^-), a situation that is reversed in adults. During development, this is changed by the appearance of a potassium-chloride co-transporter (KCC2) which starts actively pumping Cl^- out of the cell (Rivera et al. 1999; Rivera et al. 2005). It has been suggested that the depolarizing activity by GABA itself contributes to the expression of this co-transporter (Ganguly et al. 2001). This event is commonly referred to as a developmental 'GABA switch', and it ultimately results in the neurotransmitter acquiring the hyperpolarizing effect that is so essential in the adult nervous system (for reviews, see Ben-Ari 2002; Rivera et al. 2005). The time point of this maturational step might vary between areas and between cells, depending largely on when individual cells are born; however, there is general agreement that in rodents, the GABA switch finishes by the end of the second postnatal week (Ganguly et al. 2001; Ben-Ari 2002).

1.1.2 Experience-dependent refinement of neural networks

Not only the size and contents of the cell body changes through development. The synapse is a key component in neural networks that certainly needs to be considered when discussing the wiring of the brain. In the adult, synaptic contacts are made with astounding precision onto dendritic processes, somata or even axon initial segments of target cells; these specific patterns of synaptic innervation are instrumental in shaping region-specific activity of neural networks. The synaptogenesis seen during early postnatal days (Blue & Parnavelas 1983; Tyzio et al.

1999), does not lead to such sophisticated patterns of connectivity. Extensive processes of synapse reorganization and pruning have thus been observed in several parts of the developing nervous system (Lichtman & Colman 2000), and have been extensively studied in the mammalian neuromuscular junction (Brown et al. 1976; Walsh & Lichtman 2003), the cerebellum (Crepel 1982; Kano & Hashimoto 2009) and in the visual system (Chen & Regehr 2000; Jaubert-Miazza et al. 2005).

Ultrastructural studies have also given clues about the pruning of synapses in various regions of the CNS. In a quantitative study of synapses in the visual cortex of the rat (Blue & Parnavelas 1983), an initial overshoot of symmetrical (i.e. inhibitory) synapses was seen, the peak occurring around P16, before an extensive pruning occurred after P20. Meanwhile, the number of asymmetrical (i.e. excitatory) synapses increased steadily through development without any overshoot (Blue & Parnavelas 1983). However, Bähr and Wolff (1985) investigated visual cortex axosomatic synapses specifically, and found no significant reductions in the numbers of symmetrical synapses targeting them through development. Studying the quantity of synapses in the motor cortex of the macaque monkey, Zecevic and colleagues (1989) revealed a peak density and a subsequent decline that was mostly due to loss of asymmetrical synapses on dendritic spines. Studies have further demonstrated that synaptic terminals mature significantly after P15, in terms of size, mitochondrial content, and vesicle numbers (Dyson & Jones 1980), indicating that while some terminals are pruned, others mature.

Refinement by synaptic pruning and maturation, then, seems to be a common developmental theme within and between several CNS regions. The diverging results from ultrastructural studies detailed above (Blue & Parnavelas 1983; Bähr & Wolff 1985; Zecevic et al. 1989) nevertheless indicate that significant differences exist in the extent and main targets of these processes. Indeed, recent evidence suggests that in the monkey prefrontal cortex, basket and chandelier cells, two types of GABAergic interneurons, have distinct and quite opposite modes of maturation; specifically, the number of chandelier cell terminals decreased while the number of basket terminals remained unchanged (Fish et al. 2013). Such differences might mask changes when all symmetrical synapses are considered regardless of the class of the cell of origin, as has often been the case in early ultrastructural studies. Still, microcircuits of the CNS are likely to go through extensive rearrangements of immense importance for the ontogeny of adult network functions. In figuring out further details about specific microcircuits through development, it will thus be important to carefully address these processes separately for specific cell types and possibly also for different targets.

1.2 The adult brain contains an intricate spatial system

Several highly specialized cell types localized to a number of brain regions collectively termed the HR collaborate to form our internal sense of space. These regions provide excellent examples of the intricacy of microcircuits in the adult brain, and sorting out the detailed features of these networks is thus a major goal of neuroscientists today.

1.2.1 Anatomy and connectivity of hippocampal region

The term HR is a collective term for the hippocampal formation (HF) and the parahippocampal region (PHR; Boccara et al. 2015). A basic understanding of the anatomy and connectivity of these areas is required for anyone seeking to learn about spatial cognition. The rat brain will be emphasized here as it is the model used in the present study.

1.2.1.1 The hippocampal formation. In the rat, the HF is C-shaped and located in the caudal half of the hemisphere, and its dorsal region extends medially. It is subdivided along its transverse axis into the dentate gyrus (DG), the cornu ammonis (CA, 1 through 3), and the subiculum (Sub; Boccara et al., 2015). Furthermore, it has a long axis referred to as the dorsoventral or septotemporal axis in rodents (the corresponding axis in primates is termed anteroposterior; Strange et al. 2014). The subfields of the HF have three layers and are as such considered archicortex, the evolutionarily oldest type of cortex (Witter et al. 2000).

1.2.1.2 The parahippocampal region. The PHR comprises a group of cortical regions easily separated from the HF in that they have six layers instead of three. However, as they all have a very cell-sparse LIV, they represent a transition zone between the archicortical HF and the evolutionary newer neocortex (Witter et al. 2000). In rodents, the subregions of the PHR include the presubiculum (PrS) and parasubiculum (PaS), as well as the entorhinal (EC), perirhinal (PER) and postrhinal (POR) cortices, and they are all reciprocally connected to the HF and each other (Boccara et al. 2015). The areas of the PHR are not described along a septotemporal axis, but rather in terms of a dorsoventral one. Figure 1 shows an overview of the areas making up the HF and PHR.

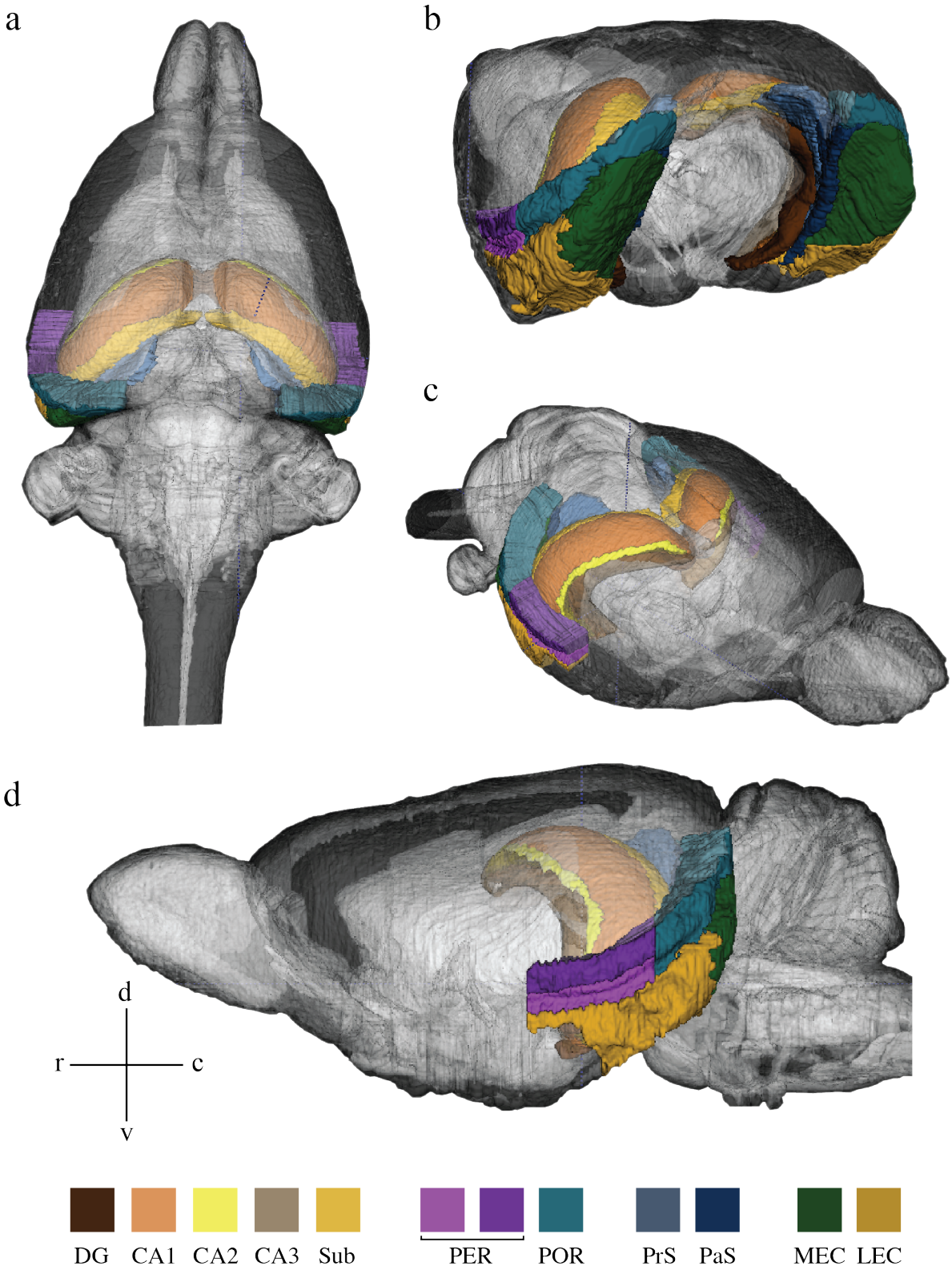

Figure 1. Representation of the HR in three dimensions. The HR seen from the **a)** dorsal, **b)** oblique occipital, **c)** oblique frontal and **d)** lateral perspective. The cerebellum and brain stem have been removed in image **b)**. The anatomical directions given apply only to image **d)**. Images are obtained by use of the Waxholm Space Atlas (Papp et al. 2014; Boccara et al. 2015; Kjonigsen et al. 2015).

The EC lines the caudal convexity of the rat hemisphere and has borders to all other divisions of the PHR. It is the main source of cortical information to the HF and is hence considered the central portion of the PHR (Boccara et al. 2015). For decades, the EC has been subject to several attempts of comprehensive subdivision. For example, Insausti, Herrero, and Witter (1997) distinguished six regions of this cortical area. However, the EC is most commonly divided into two main sub-divisions, the lateral and medial entorhinal cortices (LEC and MEC, respectively), and this is the scheme that will be used here. This division is not simply based on their respective ventrolateral and dorsomedial anatomical locations, but also on major input-output differences (Boccara et al. 2015). Both regions are reciprocally connected with the HF, but the MEC preferentially connects to the POR, PrS, as well as occipital and retrosplenial areas (Burwell & Amaral 1998). The LEC, on the other hand, is connected to the PER, the amygdala, as well as olfactory and insular cortices (Burwell & Amaral 1998). Functionally, the MEC and LEC are very different: several spatially selective cell types reside in the MEC (Hafting et al. 2005; Sargolini et al. 2006), while cells in the LEC have been shown to respond to objects (Tsao et al. 2013). These regions have thus been proposed to provide the HF with the context and content of an experience, respectively (Knierim et al. 2014).

1.2.1.3 Architecture and wiring of the entorhinal cortex. The lamination of the EC is based on cytoarchitectonic features, and these have been comprehensively studied by Insausti et al. (1997). There are six layers, of which four are cellular. LI is rich in dendritic arborizations from cells in other layers and relatively free of cell bodies. LII, on the other hand, is densely packed with cells of large and medium sizes. LIII is a heterogeneous layer, with cells of varying size. An almost cell-free strip separates LIII from the deeper layers and is considered a LIV, but it is most commonly called the lamina dissecans (Insausti et al. 1997). LV mainly contains pyramidal cells and LVI is very heterogeneous (Insausti et al. 1997; Canto & Witter 2012).

The EC is extensively connected to the HF; in the classical view, there are two major, parallel loops through this hippocampal-parahippocampal system (Witter et al. 2000). These pathways start with cortical input reaching the LEC and MEC via the PER and POR, respectively. A subset of the principal cells in layers II and III of the EC then project to the HF, their axons travelling via the perforant pathway. LII cells project to the DG and CA3, while cells in LIII reach the Sub and CA1. Output from the HF mainly target the deeper layers V and VI of the EC, and these cells in turn make up the major cortical and subcortical output from the EC (Witter et al. 2000). There are certain input-output relationships that are not mentioned in this simplified scheme, but it nevertheless provides a useful overview of the main features of

hippocampal-parahippocampal connectivity. The EC is heavily connected to other areas of the PHR as well. Apart from its connections with the HF, the MEC receive input from the PrS, PaS, POR and from retrosplenial areas. These connections have lamina-specific output patterns. The main connections between the MEC and other regions of the HR are summarized in Figure 2. Likely, wiring within and between these regions underlie their unique functions (Canto et al. 2008); as we shall see, the MEC is greatly involved in making up our sense of space.

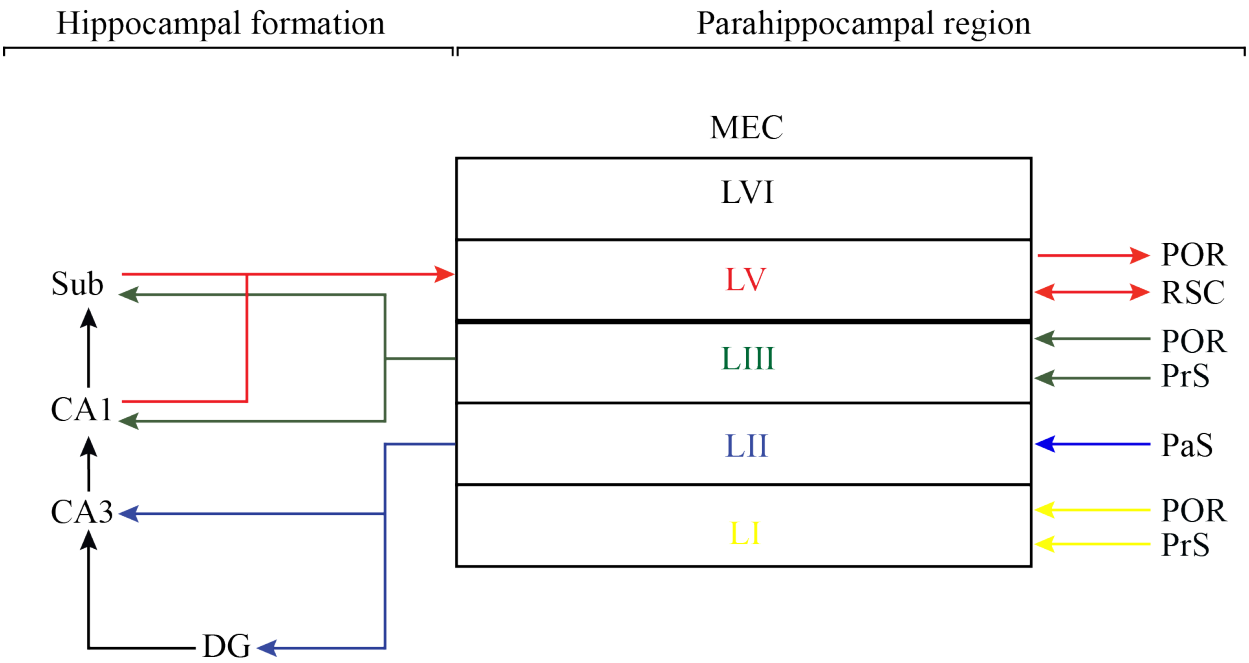

Figure 2. Simplified scheme of the connectivity of the MEC with other parts of the HR. The thick black line between LIII and LV represents the lamina dissecans. Modified from figures in Moser et al. (2010) and Witter et al. (2014).

1.2.2 Cells of the spatial system

1.2.2.1 Grid cells. In 2005, a cell type was discovered in the MEC with some quite unique spatial properties (Hafting et al. 2005). When an animal moves in a given environment, such a cell will have multiple firing fields that make up a regular triangular array covering the entire space available – consequently these cells are termed grid cells. Grid cells are found in all cellular layers of the MEC but are most abundant in LII, where they make up approximately 50% of the principal cell population (Sargolini et al. 2006; Boccara et al. 2010). Also, there are grid cells in the adjacent PrS and PaS (Boccara et al. 2010).

There are three basic parameters on which grid cell responses vary: these are phase, orientation, and spacing. The phase of the grid is the x-y locations of the firing vertices. Grid

cells with similar phases are not topographically arranged in the EC; rather, cells with different phases are scattered across the EC without any known pattern (Hafting et al. 2005). The orientation is the tilt of the grid relative to an external axis. Nearby grid cells show similar orientations, but the cells vary on this parameter along the dorsoventral axis (Hafting et al. 2005). The grid spacing is most easily understood as the 'coarseness' of the grid pattern, which increases topographically from dorsal to ventral parts of the MEC (Hafting et al. 2005; Stensola et al. 2012).

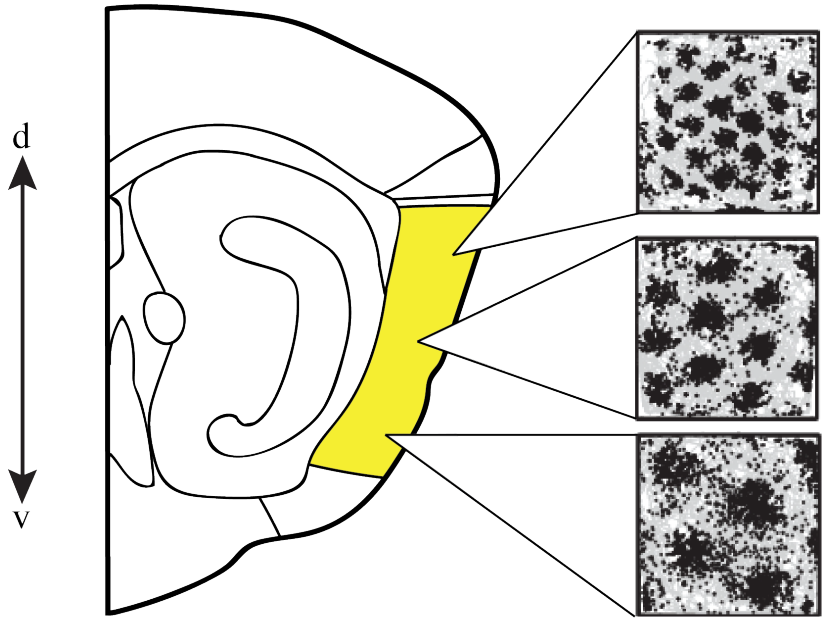

Figure 3. Grid scale along the dorsoventral axis of the MEC. Schematic sagittal section of the rat brain, revealing the dorsoventral extent of the MEC (yellow). Grid cells along this axis have progressively increasing grid scales, exemplified by the the firing rate patterns (adapted from Stensola et al. (2012)) on the right.

When an animal is exposed to a new environment, the scaling and orientation of individual grid cells remain constant, but their phases are slightly shifted. Remarkably, though, grid cells with similar phases in one environment retain their relationship across environments (Fyhn et al. 2007). Grid cell patterns are stable in the dark and are not affected by removal of external landmarks, suggesting they are not dependent on visual input. These unique properties are thought to allow grid cells to make up a general spatial metric, dependent on self-motion information rather than external cues, that the brain can apply to any environment (Hafting et al. 2005).

1.2.2.2 Other cells. The grid cell population is not the only component of the brain's spatial system. At least three other spatially selective cell types, as well as a class of speed selective cells, contribute to animals' perception of space and ability to navigate.

The first type of spatial cell to be discovered was the place cell of the hippocampus, cells that respond to a particular place in the environment called their place field (O'Keefe and Dostrovsky 1971). Place cell ensembles form different spatial maps for different environments, a process called remapping; the place field of a cell in one environment does not predict its place field in another environment (Muller & Kubie 1987; Fyhn et al. 2007), so the remapping is random. This multi-representational nature of the hippocampus is optimal for storing many memory traces separately in long term memory (Colgin et al. 2008), such as a high number of familiar places.

Head direction (HD) cells are tuned to particular allocentric directions of the animal's head, irrespective of the animals position, trunk direction, and behavior; their basic properties were first described for cells in the deep layers of the dorsal PrS (often referred to as the postsubiculum; Taube et al. 1990). However, similar cells are now known to ex in several other areas as well (Taube 2007). Both regular HD cells and cells with conjunctive HD and grid properties are found in the MEC, but exclusively in layers deeper than LII (Sargolini et al. 2006).

Border cells have firing fields aligned to particular geometric borders in the environment (Solstad et al. 2008). They react to a wide variety of boundaries, from regular walls to sudden drops in the environment. Different border cells keep their relative orientations in different rooms (Solstad et al. 2008). Border cells are scattered across all layers of the MEC and the PaS, where they make up 5-10% of the local principal cell population and typically intermingle with HD and grid cells (Solstad et al. 2008; Boccara et al. 2010).

Recently, cells with a robust and selective response to speed were reported in the MEC, where they make up about 15% of the total cell population across layers (Kropff et al. 2015). Their firing rate increases linearly with running speed, independently of visual information; thus, these cells are well-suited to update grid cells on the animal's position (Kropff et al. 2015).

1.2.2.3 Spatial cells through development. Only in the past few years have studies been conducted to investigate the physiological properties of spatial cells through development. Langston and colleagues (2010) found that HD-cells with adult-like properties are present from the outset of outbound experience, right after eye-opening (approximately P15). However, HD-cells have subsequently been recorded as early as P11, days before the eye-lids unseal (Bjerknes et al. 2015). Border cells also mature early, with consistent responses from around the time of eye-opening (Bjerknes et al. 2014). Some rudimentary place cells have been detected around P15, but the stability of these cells as well as the proportion of cells fulfilling place cell criteria

increased from P16 to P24 (Langston et al. 2010). Interestingly, cells with multiple firing fields were also observed from the very beginning of outbound experience, but their periodic properties were not strictly grid-like and evolved extensively throughout the first two weeks of outbound experience. After four weeks, however, the authors could not detect any further increase in grid scores, indicating that the cells had become mature grid cells (Langston et al. 2010). Grid cells, thus, show the most protracted development of the spatial cell types.

1.3 The intrinsic wiring of the MEC layer II may underlie grid cell firing

The adult MEC LII network consists of several diverse cell groups, and a large number of the cells in this layer are grid cells (Sargolini et al. 2006). To produce the stable patterns and rigid relationships of grid cells (Hafting et al. 2005; Fyhn et al. 2007), the intrinsic connectivity between the cells in the network is likely important.

1.3.1 Principal neurons of the layer II network

Principal cells are excitatory neurons, usually using glutamate as their transmitter; the vast majority of them send projections outside the area in which they reside (Harris & Mrsic-Flogel 2013). There are two main principal cell types in LII of the MEC. Most abundant are the stellate cells, mainly located in the superficial part of the layer (Klink & Alonso 1997). Their somata come in various sizes with several primary dendrites emerging; these branch widely into spiny processes that reach the molecular LI. A thick, primary axon emerges from one of the primary dendrites and travels towards the white matter, giving off occasional collaterals that mainly ramify within LII and superficial LIII (Klink & Alonso 1997; Canto & Witter 2012). The classic stellate cell is typically reelin positive (reelin+; Tang et al. 2014; Fuchs et al. 2015).

The other principal cell type in LII is the pyramidal cell, which has a characteristic, pyramidal-shaped soma (Canto & Witter 2012). A single, prominent apical dendrite, somewhat spiny, reaches superficially and branches just above the border with LI (Klink & Alonso 1997). The pyramidal cell has basal dendrites that are also spiny, but short, thin and straight; these branch extensively in LII and sometimes reach LIII (Canto & Witter 2012). The axon originates from the soma and gives off collaterals that branches in layers I through III as it travels towards the white matter. Generally, pyramidal cells are calbindin positive (calb+; Tang et al. 2014; Fuchs et al. 2015).

In addition to these two most abundant cell types, other non-stellate morphologies of principal cells that are not classical pyramidal have been described. Such intermediate types mainly vary on the orientation of their somata with respect to the pial surface and their number

of primary dendrites (Klink & Alonso 1997; Canto & Witter 2012). In a recent report, Fuchs et al. (2015) described a comprehensive study of the morphology, electrophysiology and cytochemical content of primary neurons in LII of the mouse MEC. Their conclusion was that there are two intermediate cell types in addition to the classic pyramidal (calb+) and stellate (reelin+) types, which they termed intermediate stellate and intermediate pyramidal cells.

The classic stellate and pyramidal morphological properties of principal cells in MEC LII (Klink & Alonso 1997) thus correspond largely to different electrophysiological profiles (Canto & Witter 2012) and cytochemical content (Fuchs et al. 2015); although not perfect, these differences are quite striking. Furthermore, reelin+ cells have been demonstrated to send axons to the DG via the perforant path, while calb+ cells generally project outside the HF (Varga et al. 2010). Thus, it is generally believed that two largely non-overlapping populations of principal cells exist in LII of the MEC, although some smaller populations of intermediate types are clearly present (Klink & Alonso 1997; Canto & Witter 2012; Fuchs et al. 2015).

Striking differences like these naturally lead researchers to search for functional correlates. Notably, grid cells and border cells are found in LII, and so these functional characteristics could in theory map onto the cytochemically and electrophysiologically different phenotypes. The stellate cells have long been key suspects for the grid cells (Giocomo et al. 2007; Couey et al. 2013). On the other hand, Tang and colleagues (2014) recently demonstrated that pyramidal cells are often grid cells while stellate cells are more often border cells. The structure-function relationship of the principal neuron classes in MEC LII, then, is still a matter of debate.

1.3.2 Interneurons of the layer II network

Interneurons are non-principal cells that provide inhibition throughout the CNS, mainly by use of GABA; these cells come with a tremendous variation with respect to their morphology, cytochemistry, electrophysiology, and connectivity, reflecting their unique roles in serving countless functions (Freund & Buzsáki 1996). Interneurons that are similar on one of these parameters can vary on others, e.g. cells that target the same postsynaptic region can have different cytochemical contents (Pawelzik et al. 2002). This makes it hard to reach a comprehensive taxonomy of IN subtypes that is useful and sufficient for all purposes.

In LII of the MEC, interneurons account for approximately 13% of the cell population (Tang et al. 2014) and can be classified morphologically as bipolar, multipolar, chandelier, or basket cells (Canto et al. 2008). The calcium-binding protein parvalbumin (PV) is found in chandelier cells and in a subset of basket cells, which together constitute about half of the

GABAergic population in the EC (Miettinen et al. 1996). The present focus will be the parvalbumin positive (PV+) basket cell.

1.3.2.1 The parvalbumin positive basket cell. Basket cells are axosomatic interneurons – that is, they target the somata of other cells, forming rich 'baskets' of terminals around them (Gulyas et al. 1993; Hu et al. 2014). In LII of the MEC, basket cell bodies are small and spherical, and their widespread axonal arbor is generally confined to the same layer; their extensive dendrites, however, often ramify widely into LI (Jones & Bühl 1993; Canto et al. 2008). Wouterlood et al. (1995) investigated the ultrastructural features of PV+ cells in the MEC by use of EM, and found that PV+ basket cells made up to six boutons per cell body per ultrathin section.

Several features make the PV+ basket cells a very interesting class of interneurons. Firstly, PV+ cells are known to be fast spiking (FS) cells, which is to say that they convert an excitatory input to an inhibitory output with astonishing rapidity – within a millisecond (Kawaguchi et al. 1987; Geiger et al. 1997). Secondly, they target the perisomatic domain of other cells (Wouterlood et al. 1995), making them well suited to control the target cell's output, hence yielding their rapid inhibition especially powerful. Lastly, they do not accommodate and are thus reliably activated during high-frequency stimulation (McCormick et al. 1985; Jones & Bühl 1993). These properties of PV+ basket cells make them well-suited to integrate input from large ensembles of principal cells and provide feedback that will lead to their synchronization, and so they have an instrumental role in oscillatory network activities (Sohal et al. 2009).

1.3.3 Intrinsic connectivity of the layer II network

Although PV+ basket cells do contact other interneurons, at least other PV+ ones (Wouterlood et al. 1995), their connectivity with the principal cells have been more extensively studied (Buetfering et al. 2014; Fuchs et al. 2015). It seems that of the two main principal cell types in LII, PV+ basket cells preferentially target pyramidal (calb+), non-perforant path-projecting cells (Armstrong et al. 2016). Still, PV+ baskets also reach the reelin+ stellate cells that project to the perforant path (Armstrong et al. 2016); this is in contrast to other types of interneurons such as cholecystokinin positive basket cells (Varga et al. 2010), indicating that they exhibit a relatively higher level of control over reelin+ cells compared to other types of interneurons.

Couey and colleagues (2013) demonstrated that the LII stellate cells are embedded in a highly recurrent, inhibitory network of FS interneurons. These recurrent connections, by which stellate cells preferentially target FS cells and vice versa, were shown to be sufficient to generate

grid patterns in a computational model. Subsequently, Buetfering and colleagues (2014) found that PV+ interneurons in the mouse MEC are strongly activated by local spatial cells, and that they are preferentially targeted by grid cells. Furthermore, activation of PV+ cells led to inhibition of most cells in the MEC on a time-scale that is consistent with monosynaptic connections, suggesting that the PV+ interneurons provide rapid feedback inhibition onto different types of spatial cells (Buetfering et al. 2014). The monosynaptic connectivity indicated by these recordings is consistent with the morphological study by Wouterlood and colleagues (1995), in which somatic PV+ terminals onto virtually all parvalbumin negative (PV–) cells in LII were observed. Together, these observations highly suggest that PV+ cells are somehow involved in regulating the activity of the local, spatially selective principal cells. They also indicate that stellate cells, controlled by PV interneurons, make up a large portion of the grid cells in LII. Less is known about the connectivity between PV cells and pyramidal cells. Fuchs et al. (2016) demonstrated that at least some of them lack connectivity with FS cells and are hence less likely candidates for grid cells. However, as mentioned, Armstrong et al. (2015) reported that calb+ cells, thought to be pyramidal cells, are heavily innervated by PV+ cells. These diverging findings probably result from different classification schemes. The central microcircuit of MEC LII is illustrated in Figure 4.

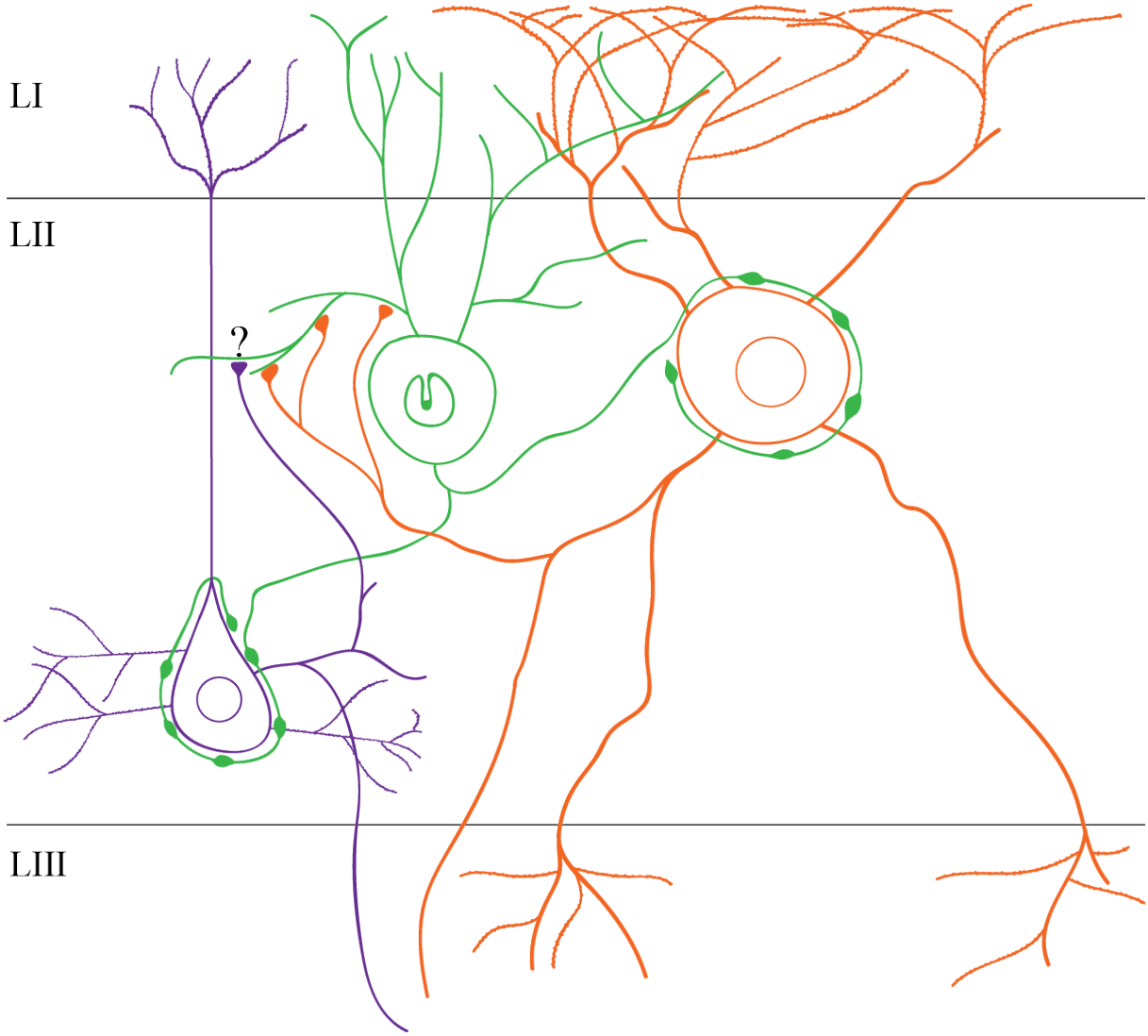

Figure 4. Illustration showing the basic microcircuit between PV+ basket cells and local principal cells in MEC LII. PV+ basket cells (green) target the somata of both calb+ pyramidal cells (purple) and reelin+ stellate cells (orange), forming several somatic 'basket terminals' around them. Stellate cells send axon collaterals that form local connections with PV+ basket cells, while the relationship between pyramidal cells and PV+ cells is less clear.

Beed and colleagues (2013) reported a gradient in PV inhibition in the juvenile MEC: not in the number of cell bodies, but rather in the number of local connections made onto LII stellate cells. Since grid spacing increases along the dorsoventral axis (Stensola et al. 2012), these results suggest that inhibition by PV+ interneurons is especially prominent in the regions where small-scale spatial representations are found. In any case, this further adds to the complexity of inhibitory microcircuits controlling the principal cells of LII MEC.

1.3.4 Layer II microcircuitry through development

Canto and Witter (2012) found that the basic morphological and electrophysiological properties of principal cells in MEC LII are already present in rats aged P14. However, in a recent study of LII principal cell development, Ray and Brecht (2016) showed a more protracted developmental timeline of LII pyramidal cells in particular. Furthermore, they noted a dorsoventral gradient in the maturation of LII pyramidal cells. Such a pattern might indicate that the small-scale spatial representations, localized to the dorsal MEC, mature prior to the ventrally situated coarse representations. Pyramidal cells throughout the dorsoventral extent of MEC showed adult-like features around P20 (Ray & Brecht 2016).

There is limited knowledge of the ultrastructural and cytochemical development of MEC interneurons in particular. However, some evidence is available from studies of comparable cells in the hippocampus and neocortex. Examining the postnatal development of basket cells in the DG, Seress and Ribak (1990) observed substantial ultrastructural maturation between P5 and P10. At ten days, the basket cells had long dendrites, the cytoplasm had become richer with organelles, and the number of axosomatic symmetric synapses made onto other cells had more than doubled. By the age of sixteen days, the ultrastructural features of the basket cells were considered adult-like (Seress & Ribak 1990). In the visual cortex of rats, axosomatic synapses onto pyramidal cells were first seen at P6, and their numbers increased approximately three-fold over the next weeks (Miller & Peters 1981). Similar timelines might exist for PV+ basket cells and their axonal arbors in the EC.

Couey and colleagues (2013) studied the connectivity between stellate cells and FS cells in LII of the MEC through postnatal development by recording responses from clusters of cells, and revealed that no recurrent connections were yet in place in rats aged P10-P15. In rats aged P28 and older, the rate of recurrent connectivity between these cell types had increased to 66%. In another study, Langston et al. (2010) demonstrated an increase in network synchrony between LII stellate cell during this time interval as well. Thus, extensive development of the intrinsic connections of FS (presumably PV+) cells in LII of the MEC takes place during the second and third postnatal weeks in rats. Yet, the development of these connections has never been investigated from an ultrastructural perspective.

1.4 Aim

The aim of this study is to further explore the developmental processes of the MEC LII network at the ultrastructural and cytochemical level. Specifically, changes in the local connectivity of a key component of this microcircuitry – the PV+ basket cell – will be investigated. There are

likely several changes in the microcircuit as the network matures. The focus of this thesis will be the development of PV+ basket terminals made onto parvalbumin negative (PV–) cell bodies, the vast majority of the latter which are principal cells with spatial properties. The aim is to provide quantitative data on the numbers and morphometric measurements of these local PV+ basket terminals.

The question will be approached by use of immunohistochemical methods combined with light- and electron microscopy (LM and EM, respectively). Part of the aim will therefore be to work out a satisfactory protocol for immunohistochemistry at the LM- and EM-level.

2 Methods

Detailed protocols, recipes for solutions, as well as a list of chemicals and antibodies are included in appendices IV, V, and VI respectively.

2.1 Methodological testing

Several experiments were performed to find optimal protocols that would result in sufficient labelling and good structural preservation for LM and EM. What was needed were sections of 35 and 60 µm for LM and EM, respectively. Furthermore, an immunohistochemical protocol for LM that yielded good visualization of axonal and dendritic arbors was desired. Lastly, a protocol for immunohistochemistry at the EM level was needed that gave sufficient penetration of labelling while preserving the ultrastructural integrity of the tissue. Based on these needs, tests of protocols for fixation and vibratome sectioning were performed, as well as tests of different immunohistochemical protocols for both LM and EM. The optimized methods will be presented next, while results from the testing itself will be reported in the results section.

2.2 Animals and perfusion

In total, 19 Long Evans hooded rats, received from the Kavli Institute, were used for this study. This included four rats aged P10 and P15, two aged P20, six aged P30, and three rats aged P90. All rats were used for methodological testing for both LM and EM. Only those from the P10, P15 and P30 groups, however, were used for the final protocols and analysis. Of these, five were used for LM analysis and five for EM analysis. The animals were treated in compliance with the regulations set by the Norwegian Animal Research Authority (NARA).

The animals were anesthetized with 4-5% of Isofluorane gas and subsequently given an overdose of pentobarbital. The youngest animals, i.e. those from the age groups P10 and P15, were not given pentobarbital but were kept anesthetized with Isofluorane only. Upon absence of reflexes, the animals were transcardially perfused with a solution of 4% paraformaldehyde (PFA) and 0.1% glutaraldehyde (GA) in 0.1M PBS. The brains were then removed from the skull and transferred to the same fixative. Brains intended for LM were stored on the same fixative at 4°C for one week until sectioning. Those meant for EM, on the other hand, were kept on the fixative at 4°C for two weeks and then sectioned.

2.3 Vibratome sectioning

Prior to vibratome sectioning, the hemispheres were separated, and the rostral half of the forebrain and most of the cerebellum were cut off (see Figure 5a). The remaining tissue block

was washed 3x10 minutes in 0.1M phosphate buffered saline (PBS; Oxoid). The tissue block was then put in a well and immersed in gelatin (porcine skin gelatin (Sigma), 10% in 0.1M Sørensen's PB). The whole well was put in the oven at 37°C for 30 minutes for infiltration, and was then left at 4°C for a minimum of 30 minutes to set. The gelatin embedded tissue block was then cut with a Leica VT 1000S vibratome. Tissue for EM was not immersed in gelatin, since this tissue had undergone a longer immersion-fixation. Sagittal sections of 35 µm and 60 µm were cut for LM and EM, respectively, all the while being kept in chilled 0.1M PBS. Sections containing MEC were chosen based on the atlas provided by Boccara et al. (2015; selected areas are illustrated in Figure 5b), and transferred to wells with cold 0.1M PBS.

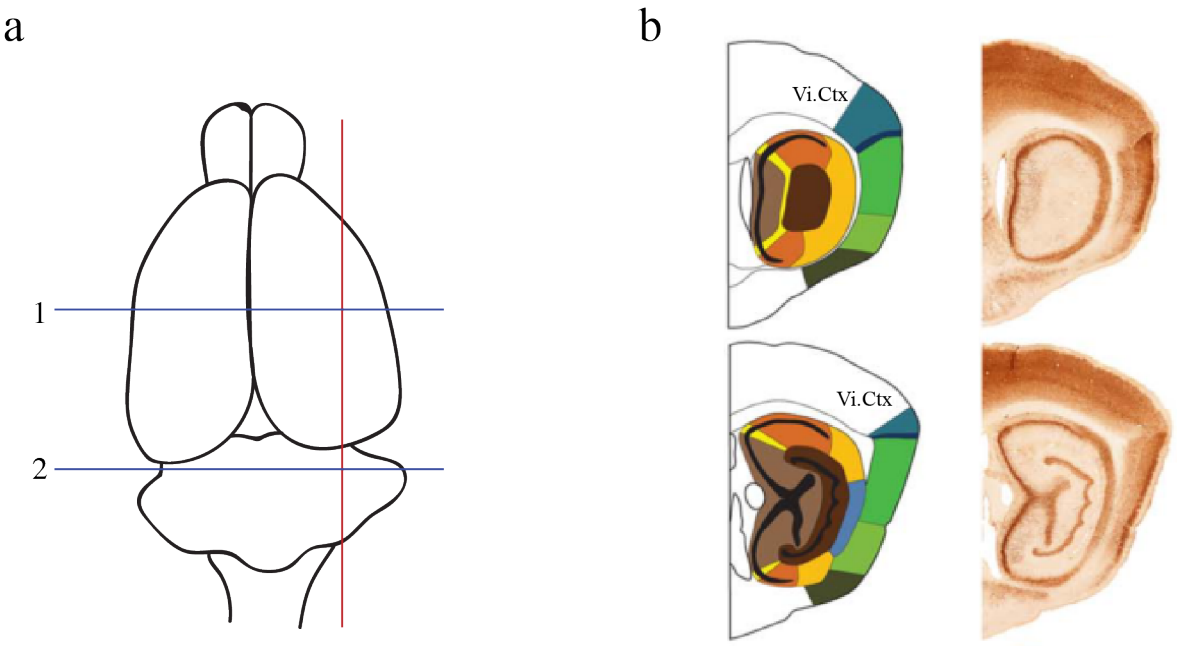

Figure 5. Sectioning plane and choice of area. **a)** The sagittal sectioning plane is illustrated by the red line. The rostral half of the hemisphere and the cerebellum, separated from the area of interest by blue lines 1 and 2, respectively, were cut off prior to sectioning. **b)** Adapted from Boccara et al. (2015). Schematic and PV stained sagittal sections from a rat brain showing the areas selected for LM and EM processing in this study. The MEC is color-coded green. Vi. Cx, visual cortex.

Sections intended for EM were kept on fixative overnight, again in 4% PFA and 0.1% GA in 0.1M PBS. All tissue sections were kept on PBS and stored at 4ºC until they were used, which was within three weeks after sectioning.

2.4 Light microscopy

2.4.1 Preparation of tissue

All sections processed for LM were treated at the same time and in the same way. 12-well plates were used and four sections were processed in each well. The plate was placed on a shaker during all steps. Incubations were done in a humidified chamber and at room temperature, unless specified otherwise. Incubation solutions had a pH between 7.4 and 7.5. Rinsing steps were carried out in 0.1M PB. Milli-Q (MQ) water was used to dilute solutions. Negative controls were included and underwent all steps except incubation with primary antibody.

Sections were first rinsed 3x15 minutes, before permeabilization was done for 2x10 minutes in 0.1M PB and 1% triton X-100 (TrX). Endogenous peroxidase activity was blocked by incubating sections for 30 minutes with a solution of 1% hydrogen peroxide (H_2O_2) in 50% methanol in 0.1M PB. After rinsing for 3x15 minutes again, non-specific binding to endogenous epitopes was blocked by incubation in 0.1M PB with 1% TrX and 5% normal horse serum (NHS). After this, sections were incubated with the primary antibody, polyclonal goat anti-PV (PVG-214, Swant), diluted 1:40 000 in 0.1M PB with 1% TrX and 5% NHS. Incubation was done at 4ºC overnight (a total of 22 hours).

The next day, sections were rinsed for 4x15 minutes and then incubated with the secondary antibody, biotinylated horse anti-IgG (BA-9500, Vector Laboratories), diluted 1:200 in 0.1M PB and 1% TrX. This incubation was done overnight at 4ºC.

After incubation in secondary antibody, sections were rinsed for 4x15 minutes, before 60 minutes of incubation in an avidin-biotin complex (ABC; PK-4100, Vector laboratories). Sections were then rinsed again, before being stained with 3,3-diaminobenzidine (DAB). Specifically, 0.05% DAB and 0.01% H_2O_2 in 0.1M PB was used, where the H_2O_2 was added within a couple of minutes before use. This step was done in the dark. After 8 minutes, the reaction was stopped in 0.1M PB and the sections were rinsed for 3x10 minutes.

Next, sections were rinsed for 2x10 minutes in MQ-water. They were then mounted on glass slides and left to dry in room-temperature for 30-40 minutes. Lastly, sections were cover-slipped using tissue mount and left to dry in a fume hood overnight.

2.4.2 Image acquisition and observations

Sections prepared for LM were scanned with an Olympus VS120 Virtual Slide Microscope, using a 10X objective for the whole section and a 40X objective for areas of interest. The

scanned sections, two from each animal, were then inspected and images were obtained using the imaging software OlyVia 2.8 (Olympus). Due to this limited number of sections, quantitative assessments were not made. Nevertheless, a number of observations were made. Sections from each age group were inspected for labelled cells, keeping in mind their laminar distribution, the shape of their somata, the density and arborizations of their axons and dendrites, and the visibility of basket complexes around PV– cell bodies.

2.5 Electron microscopy

Vibratome sections prepared for EM were treated in two separate rounds; the first round included the sections from P10, while the ones from P15 and P30 animals were processed two weeks after. The methods for preparing tissue for EM are summarized in Figure 6, and the complete protocol can be found in appendix IV.

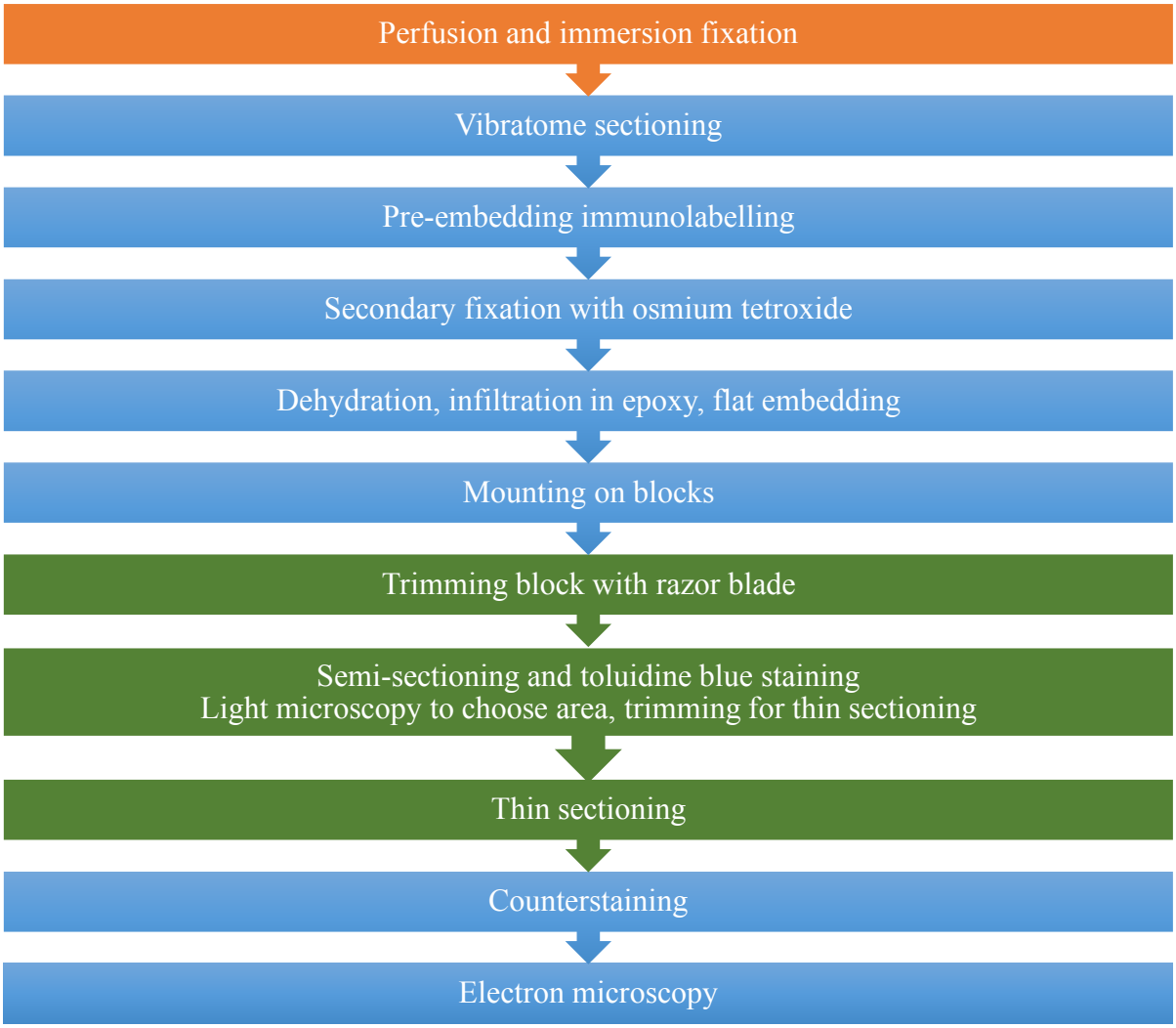

Figure 6. Flowchart for preparation of tissue for EM. Fixation (in orange) was performed by technicians at the Kavli Institute. Steps in green were performed by technicians at the EM-lab.

2.5.1 Immunohistochemistry

During immunohistochemistry for EM rinsing steps were carried out for 5x7 minutes in 0.1M PB unless otherwise specified. Apart from this point, the same conditions regarding pH, temperature, etc. apply as for the LM protocol (see section 2.4.1).

Sections were first rinsed. All sections were then permeabilized with a solution of 0.05% TrX in 0.1M PB, and subsequently rinsed again. Endogenous peroxidase activity was blocked by use of 1% H_2O_2 and 50% methanol in 0.1M PB. Sections were then rinsed again. Blocking of non-specific endogenous epitopes was achieved by incubating sections for 90 minutes in a solution of 1% NHS and 1% bovine serum albumin (BSA) in 0.1M PB. For sections from age P15 and P30, but not for sections from P10, 0.05% TrX was included in this solution. Sections were incubated with the primary antibody – polyclonal goat anti-PV (PVG-214, Swant), diluted 1:40 000 in 0.1M PB with 1% NHS and 1% BSA – overnight (a total of 19 hours) at 4ºC.

The next day, sections were first rinsed before being incubated with the secondary antibody – biotinylated horse anti-IgG (BA-9500, Vector Laboratories), diluted 1:400 in 0.1M PB. Incubation was done for 2 hours. After rinsing, sections were incubated with ABC (PK-4100, Vector laboratories) for one hour. Sections were rinsed, and then stained with 0.03% DAB and 0.01% H_2O_2 in 0.1M PB in the dark. The reaction was stopped in 0.1M PB after five minutes (P15 and P30 sections) or seven minutes (P10 sections), and rinsed again.

Images to use for selection of areas later were obtained by use of a Zeiss axiophot LM; images were obtained with a 10X objective. Prior to proceeding, sections were moved to a new, sterile set of wells to prevent precipitates from the silver development that was to be used the next day. In addition, all glassware used from this point and until the secondary fixation step had been rinsed for 30 minutes with 10% hydrochloric acid. This was also the case for the glassware used for making solutions to be used within this time window. Also, the MQ water used to dilute these solutions had been boiled. After obtaining images, the sections were then rinsed for 3x10 minutes with a 2% solution of sodium acetate (pH 8.7). After the rinsing in sodium acetate, sections were incubated in a 10% solution of sodium thioglycolate at 4ºC overnight (a total of 13.5 hours) to suppress tissue argyrophilia.

Next, sections were rinsed again 3x10 minutes in 2% sodium acetate. A gold-substituted silver-peroxidase (GSSP) protocol was subsequently used to enhance the DAB-staining. Physical development was carried out with a mixture of fresh silver solution. The solution consisted of three different parts (see appendix V for details), and these were mixed immediately before use. The development was carried out for 7-8 minutes in the dark before being stopped in a 1% solution of acetic acid. After 2 minutes in acetic acid, sections were

rinsed 3x10 minutes in 2% sodium acetate. The silver stains were stabilized and enhanced by incubating sections in 0.05% gold chloride in 0.1M PB for 15 minutes, also in the dark. Lastly, sections were rinsed with 2% sodium acetate, treated with a 3% solution of sodium thiosulphate for ten minutes, and rinsed 3x10 minutes in 2% sodium acetate.

2.5.2 Further processing for electron microscopy

Prior to secondary fixation, the sections were rinsed in a 0.1M cacodylate buffer for 2x10 minutes and transferred from wells to dram glasses. Secondary fixation was then carried out for 15 minutes with a solution of 1% osmium tetroxide and 1.5% potassium ferrocyanide in 0.1M cacodylate buffer. Sections were kept in the dark during this treatment. After post-fixation, sections were again rinsed for 2x10 minutes in cacodylate buffer.

A graded series of ethanol was used to dehydrate sections; specifically, 50%, 70% and 90% ethanol were used for ten minutes each, followed by four rounds of 15 minutes in absolute ethanol. Acetone was used as a transitional solvent for two rounds of 15 minutes. Sections were then infiltrated with three rounds of epoxy resin mixed with acetone. Immediately before use, 0.15 ml of the accelerator DMP-30 was added to the epoxy. Sections were left for two hours in a 2+1 acetone-epoxy ratio and then in 1+1 acetone-epoxy for two hours. Lastly, a 1+2 ratio of acetone-epoxy was used overnight (a total of 11.5 hours) and the dram glasses were transferred from the shaker to a rotator. The next day, infiltration was continued with pure epoxy for eight hours, during which the epoxy was replaced with a fresh mixture once, after six hours.

After infiltration was complete, sections were put on a small drop of epoxy between two sheets of Aclar film, and then in between two microscope slides. They were left to polymerize overnight at 60ºC (in total 11.5 hours). The next day, the Aclar films were removed, and areas of interest were selected and cut out under the stereomicroscope. The selected pieces were glued onto epoxy blocks with a drop of epoxy. Cuts were made from the dorsal-most region of the MEC, based on the atlas by Boccara et al. (2015; see figure 5b), and two pieces from each section were mounted on individual blocks. An example section with indications of where cuts were made is depicted in Figure 7.

Figure 7. Selection of areas to mount on blocks. The image shows an example of a sagittal section from P30, with indications (black outlines) of selected areas that were mounted on blocks to use for EM.

The blocks were polymerized at 60ºC for 3 days. LII of the MEC was identified and blocks trimmed accordingly with a razor blade. The deeper layers of the MEC, as well as part of LIII were trimmed away. Semi-thin sections of approximately 500 nm were first cut by use of a Leica EM UC6 ultramicrotome and stained with toluidine blue. These were used for orientation, and a trapezoid block face was made. Approximately 55-60 nm thick sections were then cut and collected on copper grids: either on a slot grid with a support formvar film, or on 200 mesh thinbar grids. Counterstaining was done with 4% uranyl acetate (8 minutes in the dark) and 1% lead citrate (3-4 minutes). A detailed counterstaining protocol is included in appendix IV.

2.5.3 Data acquisition and analysis

The grids were investigated with a transmission electron microscope (TEM; JEM JEOL 1011). The sections that were finally used for analysis originated from four blocks each from P10 and P15, and six blocks from P30.

2.5.3.1 Sampling and image acquisition. Under the EM, whole sections were investigated at a low magnification to identify LII. LI is easily distinguished as it is relatively cell free. The border between LII and LIII is less prominent, but LII is generally slightly denser with cells (Boccara et al. 2015). Often, looking at the block under the stereomicroscope or inspecting the toluidine blue-stained sections could aid in recognizing the border in the EM. Once identified, rigorous attention was paid to stay within LII when going to higher magnifications. Only PV– cell bodies receiving PV+ synaptic input were sampled. Furthermore, a cell body was only

included if it displayed a nucleus. Images were obtained of PV+ basket terminals targeting the cell bodies at 8000X for overview, 15 000X for a closer look, and at 25 000X for the individual terminals. Also, images were obtained of the cell body at the highest magnification that could include it as a whole, most often at 5000 or 6000X.

2.5.3.2 Measurements. The number of PV+ somatic boutons making synaptic contact per cell body per thin section were counted. Only synaptic contacts made strictly onto the soma were counted, i.e. those on perisomatic regions such as proximal dendrites or the axon hillock were not. PV+ neurons make symmetric contacts with their targets, hence they lack a prominent post-synaptic density. Because vesicles were usually obscured by the labelling, a synapse was defined here by (1) two closely apposing membranes; (2) a narrow synaptic cleft and (3) a darkening of the extracellular space within this cleft (Gray & Guillery, 1966). Bouton density was considered in addition to the absolute number of boutons, calculated by dividing the perimeter of the soma by the number of terminals.

The size of somata and nuclei was measured by calculating their mean axis based on their longest and shortest axes (i.e. (long axis + short axis)/2). Size measurements (long axis, short axis, and area) of individual boutons were also made. For each terminal, the aspect ratio (long axis/short axis) was calculated and the number of mitochondria noted. The imaging software iTEM 5.0 was used for all size measurements.

2.5.3.3 Categorization of putative interneurons versus principal cells. To attempt a categorization of interneurons and principal cells, the cells were divided into two groups: those with and without a deeply indented nucleus. Those with shallow indentations were excluded from this categorization. Because so few cells had indented nuclei at P10, and because findings indicate that this is a feature of interneurons that appears later than this stage (Seress & Ribak 1990), this was not done for the cells from P10.

2.5.3.4 Statistical analysis. A one-way analysis of variance (ANOVA) was performed to compare the mean values across age groups for the size of the soma, the number of boutons targeting the soma, and the bouton densities. Similarly, a one-way ANOVA was conducted on the mean values for the bouton measurements, i.e. area, aspect ratio, and number of mitochondria. Games-Howell post-hoc tests were used after each ANOVA for pairwise comparisons of all means. A Student's t-test was conducted to look for differences between the animals in the P10 and P30 groups. Results were considered statistically significant at $p < .05$.

3 Results

3.1 Methodological testing

3.1.1 Testing of fixation protocol and vibratome sectioning

Immersion fixation of the P10 brains (in 4% PFA and 0.1% GA in 0.1M PBS) for a week after perfusion fixation was not sufficient and yielded sections of uneven thickness when using the vibratome. Capsuling the brains in gelatin prior to sectioning was thus tried, and this worked well for getting sections as thin as 35 μm. However, because this was a time consuming process and because the sections with gelatin were more difficult to handle afterwards, an extended time of immersion-fixation was subsequently tested for tissue intended for EM processing. The sectioning problems were resolved by leaving the brains on the fixative for two weeks instead of one, resulting in good quality and reproducible sections of 60 μm.

3.1.2 Testing of immunohistochemistry protocols

A number of variables were tested to work out optimal immunohistochemistry protocols for both LM and EM.

3.1.2.1 Testing for light microscopy. The regular protocol used in the lab for EM was tested as a protocol for LM. This yielded labelling in cell bodies only, and no visualization of dendrites or other processes. A protocol regularly used for fluorescence at the Kavli Institute was adapted to DAB and tested instead (the original and adapted protocols are detailed in appendix IV). The main changes were that the new protocol had no sodium borohydride, used fewer ingredients for the antibody diluent buffer, and that it used phosphate buffer (PB) rather than tris buffered saline (TBS). The use of this protocol proved to label dendrites to a much larger extent. Within the frame of this new protocol, different DAB reaction times were also tested, specifically 4 and 8 minutes. Lastly, primary antibody concentrations of 1:20 000 and 1:40 000 were compared. It was concluded that an primary antibody concentration of 1:40 000 combined with 8 minutes of DAB reaction time would give the best result.

3.1.2.2 Testing for electron microscopy. The new immunohistochemistry protocol for LM was far less elaborate than the one that had previously been used for EM. Thus, it was tested as a protocol for EM (the only change being use of 0.05% TrX instead of 1% and an antibody

concentration of 1:20 000 instead of 1:40 000) to see if it worked as well as the old one. For adult animals, this protocol yielded just as good results in terms of morphology and labelling. Due to a suspicion that the younger brains would not handle as much of the permeabilizing agent TrX, the number of steps that included TrX was slightly reduced before testing this new protocol for P10, P15, P20, P30 and P90 brains. Even so, this did not yield the desired results. Especially the material from the youngest brains showed reduced morphology after this treatment. This material showed loss of membrane integrity, severe loss of ultrastructural detail, and loss of cytoplasm. In other words, the material was unrecognizable and the morphology did not allow for any analysis.

Because of the limited time frame, only three age groups – P10, P15 and P30 – were used for further testing. The theory was that the poor morphology mainly had to do with the amount of TrX still being too high, as this is known to dissolve lipids and thus will damage membrane integrity. However, a certain amount would be needed for proper antibody penetration. Sections were prepared for LM with various numbers of steps including TrX and different antibody concentrations to determine how few steps could be used and still yield labelling. Based on these results, new experiments were designed for EM. Apart from reducing the number of steps including TrX, 1% BSA was added to the blocking medium and antibody diluent buffer because parallel testing in the lab had concluded that this would help protect the morphology. Also, other tests had shown that 1% NHS would suffice, so that was the final concentration used. Rinsing steps were changed so that more steps of shorter time were used. Finally, the DAB reaction time and the antibody concentration were lowered. One section from each animal was also embedded without undergoing immunohistochemistry to rule out perfusion artifacts or other causes of morphological damage apart from the immunohistochemistry. At last, satisfactory compromises for the three age groups were found.

The material from P10 had to be treated differently than that from the others. With only one 20-minute step of permeabilization in 0.05% TrX in 0.01M PB, good morphology with satisfactory labelling was obtained. However, it should be noted that perfusion of young animals is very challenging, and that the morphology of the P10 animals was slightly poorer than that of the other age groups even prior to the immunohistochemistry protocol.

The tissue from animals aged P15 and P30 handled treatment with TrX slightly better than the P10 tissue, but the morphology suffered a great deal after the first protocol. However, when TrX was completely omitted or limited to one step of 20 minutes only, the labelling was so limited that the material was useless. Even though high numbers of labelled cells could be seen at the LM level after these treatments, it seemed that the antibody had not penetrated the

tissue sufficiently; consequently, at the EM level, labelling was only seen at the very surface of the tissue. For P15 and P30 material, then, 0.05% TrX was included in two individual steps: one 20-minute step of permeabilization in 0.01M PB, and one 90-minute blocking step with 1% BSA and 1% NHS in 0.01M PB. With this treatment, the amount of labelling increased and still yielded good morphology. Since the penetration of label seemed to be limited compared to what had obtained with tougher treatments previously (i.e. the first protocol), this compromise between morphology and labelling was probably not optimal. However, in light of the time frame and purpose of this project, it was deemed satisfactory. Detailed protocols and electron micrographs of material obtained by their use can be found in appendix IV and II, respectively.

3.2 Light microscopic results

An Olympus slide scanning microscope was used to scan sections, and the imaging software OlyVia 2.8 was used during inspection of sections and for obtaining images. Observations were made from two sections from P10 and four sections each from P15 and P30 (i.e. two sections from each animal).

3.2.1 Postnatal day 10

At P10, PV+ cell bodies could already be observed in the HF and in the PHR. In the MEC, these cells were mainly located superficially, i.e. in layers II and III. Few cells were seen in deeper layers. In the ventral region, there was a band of stained cells deeper in the cortex that might correspond to the PaS. The dendritic arbors were more developed in the dorsal part of the MEC, in the sense that LI appeared more densely packed with dendrites in this region. This did not seem to have to do with an increased number of labelled cell bodies, but LII also looked slightly more heavily stained with immunoreactive fibers in the dorsal region. A light micrograph depicting the superficial layers of MEC at P10 can be seen in Figure 8.

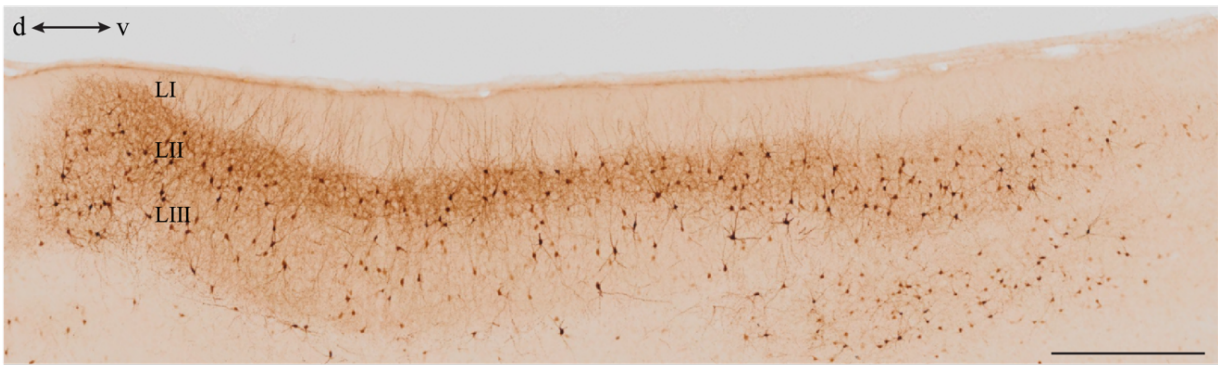

Figure 8. Micrograph of the superficial MEC from a P10 sagittal section. Scale bar: 500 μm.

In LII, the PV+ cell bodies generally had round or multipolar appearances, and differed in the intensity of labelling – from very lightly brown to pitch black. The tissue was quite lightly stained at P10, which in many cases made it easy to follow the dendritic tree of a cell. Virtually all cells had more than one dendrite radiating from the soma, reaching towards and into the molecular LI, and those that branched did so close to the soma. PV+ dendrites were smooth in appearance. Presumed basket complexes around PV– cell bodies could be seen, at least in the dorsal LII, but they were not unambiguously identified. The extent of PV immunoreactivity in superficial layers of MEC contrasted an absence of labelling in corresponding layers of neocortical areas; in the visual cortex, only a deep band of immunoreactive cells was visible, probably corresponding to layer V. A PV stained section from P10 is depicted in Figure 9.

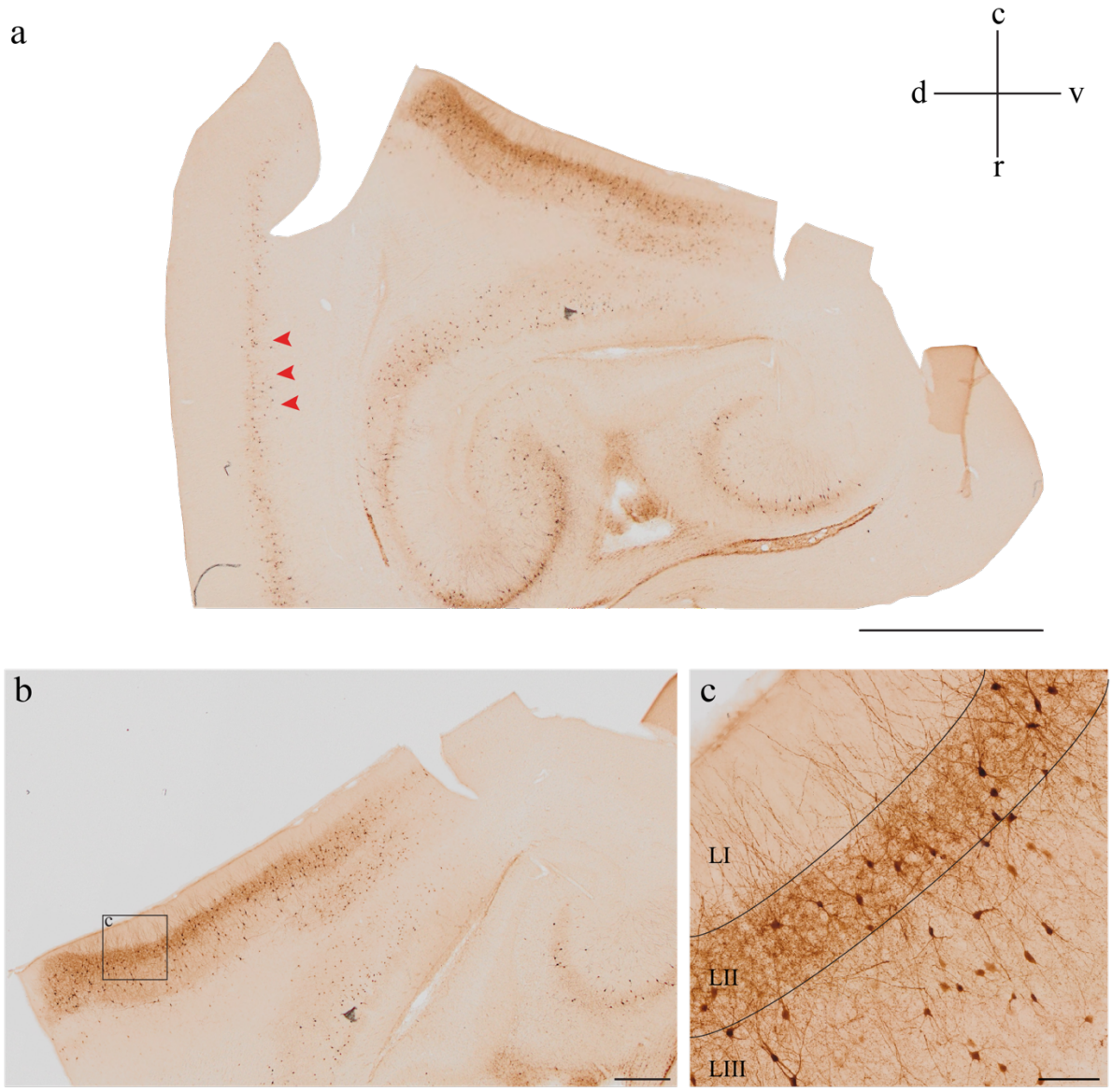

Figure 9. PV stained section at P10. Red arrows in **a)** indicates the visual cortex, where cells are only seen deeper in the cortex. Scale bars are **a)** 2mm, **b)** 500 μm, and **c)** 100 μm.

3.2.2 Postnatal day 15

At P15, far more PV+ cells were seen in the regions surrounding the MEC, e.g. the HF, other areas of the PHR, and in neocortical regions. Within the MEC, there were generally more PV+ profiles than at P10. The deeper layers were richer in PV+ cells and arborizations than before, and the deep layers V and VI could easily be distinguished from the superficial ones by a clear lamina dissecans. However, layers II and III were no longer as easily distinguished from each other as they had been at P10. Figure 10 displays a section from P15.

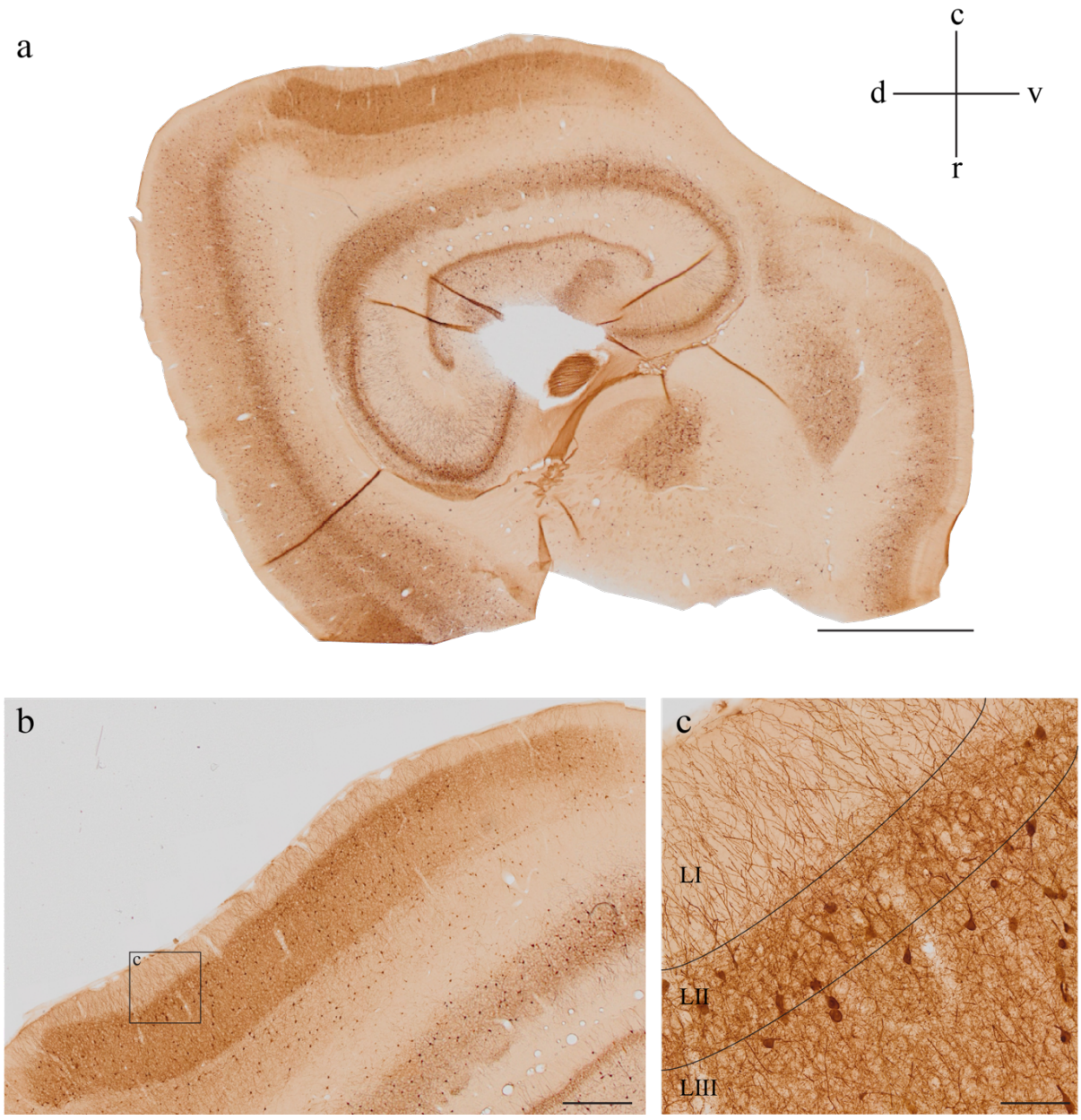

Figure 10. PV stained section at P15. Scale bars are **a)** 2mm, **b)** 500 µm, and **c)** 100 µm.

In terms of somatic shapes, the same basic forms could be identified as at P10; some were round, some multipolar, and some were slightly pyramidal. The labelling intensity varied, and for some cells there was also a difference in staining intensity between nucleus and cytoplasm – some nuclei were more lightly stained than the cytoplasm and some were darker. The tissue was more heavily stained at P15 than at P10, giving it a darker brown appearance. Especially LII and LIII were very densely stained with cell bodies, and the increase in immunoreactivity seen in these layers mainly seemed due to increased amounts of dendritic and axonal arbors. In these layers, basket synapses were easily distinguished, surrounding PV– cell bodies. Because of the darker appearance of the tissue, it was difficult to follow the dendrites and to determine their branching patterns. However, at least some dendrites were very long. There was no apparent gradient in the density of PV+ dendritic arborizations, as LI appeared evenly packed with dendrites along the dorsoventral axis.

3.2.3 Postnatal day 30

At P30, PV+ cell bodies in the MEC displayed a clear laminar distribution. Especially the lamina dissecans was more prominent than it had been at P15, which made it easy to distinguish the superficial from the deep layers of the MEC. A section from P30 is displayed in Figure 11.

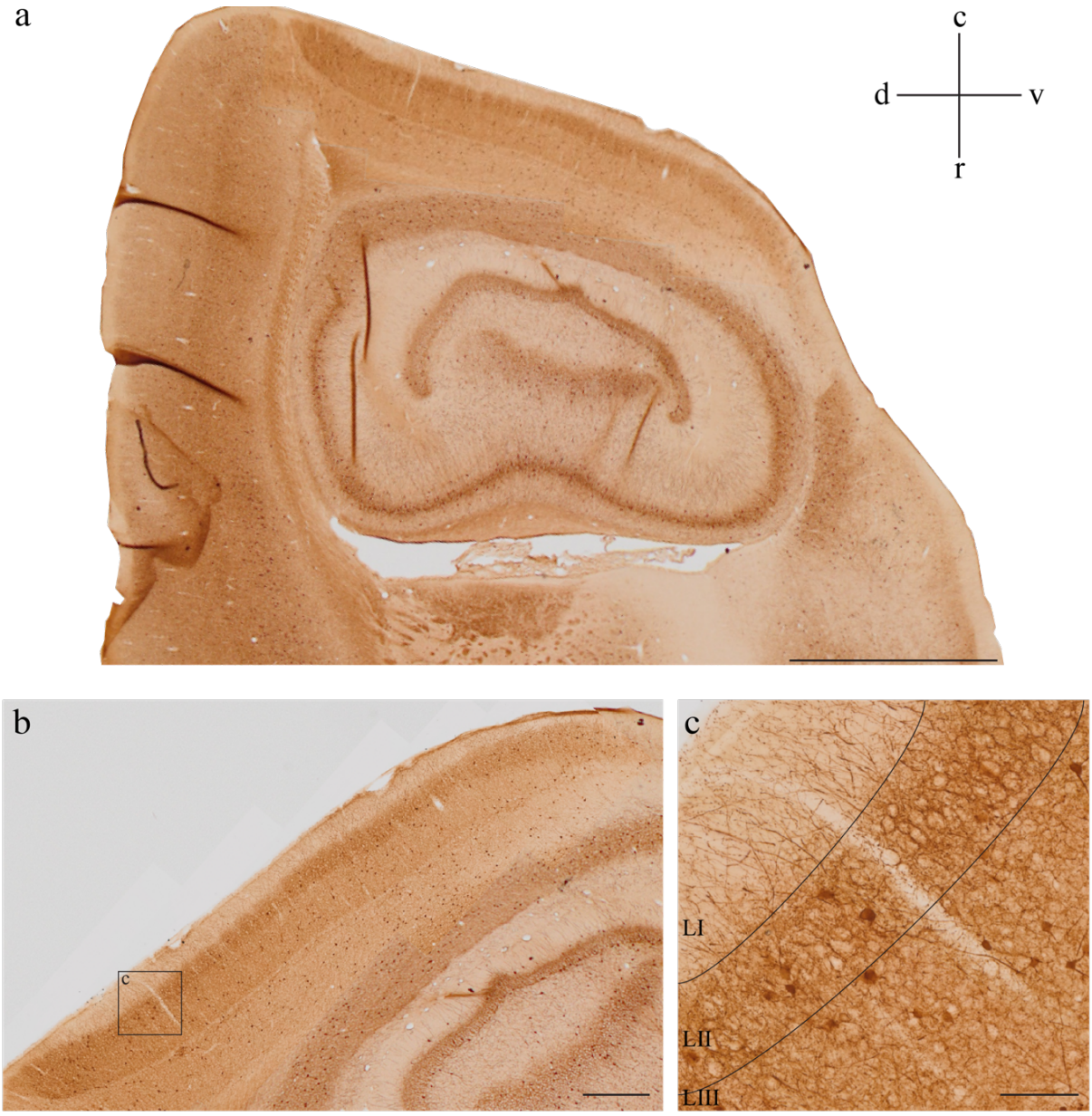

Figure 11. PV stained section at P30. Scale bars are **a)** 2mm, **b)** 500 μm, and **c)** 100 μm.

The same round, multipolar and pyramidal-like somatic shapes were seen as described for earlier ages. A similar variance in labelling intensity across cells was observed. Because the tissue was generally darkly stained, it was hard to follow the dendritic arborizations for a single cell. No dorsoventral gradient was seen in the density of dendrites in LI; as at P15, the layer was uniformly and densely stained with PV+ dendrites. PV+ basket synapses around PV– cell bodies were abundant and clearly discernible, even more so than at P15, making clear, dark circles around immunonegative cell bodies. Sometimes axonal varicosities were also discernible. Figure 12 depicts a comparison of the visibility of basket complexes around PV– somata between the different age groups.

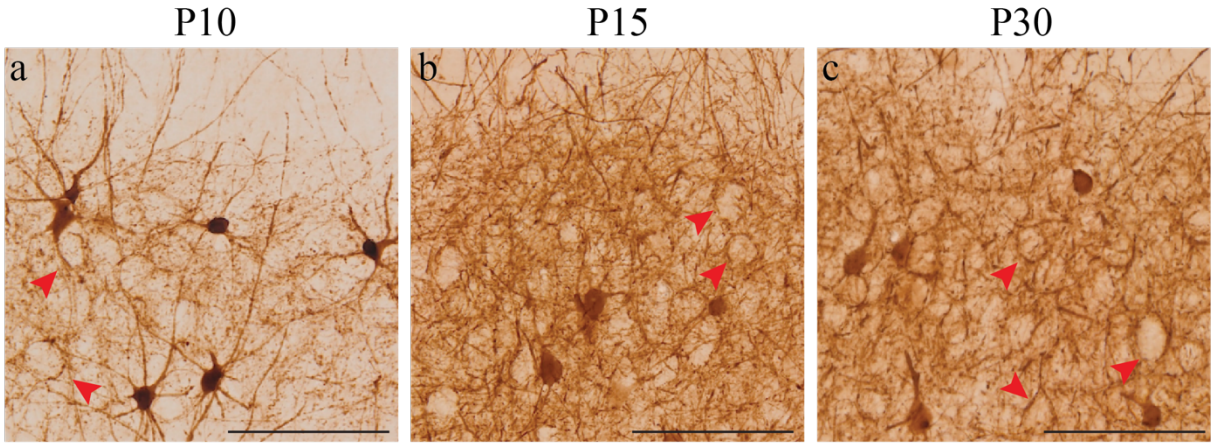

Figure 12. PV+ basket complexes around PV– somata at different ages. Light micrographs are obtained from dorsal regions of the MEC in sagittal sections. Examples of PV+ basket complexes around PV– cell bodies are indicated by red arrows. Scale bar: 100 μm.

3.3 Electron microscopic results

For EM analysis, the focus was exclusively on PV+ basket terminals made onto the somata of PV– cells, and features of these somata.

3.3.1 Somatic variables

Across all age groups, most of the cell bodies were categorized as round, ovoidal or elongated in shape, and less frequently as multipolar, pyramidal or fusiform. At P10, the cytoplasm of many of the cell bodies were slightly more electron dense than what is usually seen in adult tissue, giving them a darker appearance in the EM. Such an appearance was much less common at P15 and P30.

A one-way Analysis of Variance (ANOVA) was carried out to look at age-related changes in the somatic variables, i.e. soma mean axis, nucleus mean axis, number of PV+ boutons per cell body per thin section, and density of PV+ boutons (number of terminals per μm membrane per thin section, referred to hereafter as bouton density). This test revealed that the mean axis of the soma varied significantly with age, F (2, 235) = 7.16, p = .001, and so did the mean axis of the nucleus, F (2, 230) = 8.07, p < .001. Levene's test indicated unequal variances between groups in the number of somatic boutons; similarly, variances in the bouton density were unequal (the results from this test are detailed in appendix III). Still, Welch's test revealed significant differences in the number of PV+ somatic boutons per soma per thin section, F = 77.07, p < .001, and in the bouton density, F = 75.93, p < .001.

A Games-Howell post hoc test was carried out for pairwise comparisons between all groups, to determine the groups between which the means were significantly different.

The soma mean axis was on average significantly smaller at P10 (N = 78, M = 15.24, SEM = 0.37) than at both P15 (N = 80, M = 17.32, SEM = 0.45), p = .001, d = 0.57, and P30 (N = 80, M = 16.84, SEM = 0.39), p = .010, d = 0.47. The mean axis was larger at P15 than P30, but this difference was non-significant, p = .700, d = 0.13. At P10, ~31% of the cells displayed one or more somatic spine. Their frequency decreased across age groups, and were observed at ~26% of the cells at P15 and at 15% of the cells at P30.

The nuclei were round or ovoidal in shape across all age groups. At P10 the nuclei had smooth membranes. Although some of the nuclei had what resembled indentations, these were very shallow. At P15, approximately 6% displayed a deeply indented nucleus and 10% did so at P30. The mean axis of the nucleus increased throughout the period. P10 nuclei (N = 77, M = 8.95, SEM = 0.25) were significantly smaller than those at P15 (N = 80, M = 10.28, SEM = 0.34), p = .005, d = 0.50. Furthermore, P10 nuclei were significantly smaller than those at P30 (N = 76, M = 10.49, SEM = 0.28), p < .001, d = 0.66. The nuclei at P30 were marginally larger than those at P15, but this difference did not reach significance, p = .879, d = 0.08.

The number of PV+ somatic boutons per cell per thin section was significantly lower at P10 (N = 80, M = 2.44, SEM = 0.16) than at P15 (N = 80, M = 6.78, SEM = 0.37), p < .001, d = 1.69. However, the cells at P15 received contact from significantly more PV+ somatic boutons than did P30 cells (N = 80, M = 5.38, SEM = 0.32), p = .013, d = 0.45. Nevertheless, the number of boutons targeting P30 cells was significantly higher than that for P10 cells, p < .001, d = 1.30. The same pattern was seen when comparing the means for bouton density: P10 cells (N = 75, M = 0.04, SEM = 0.003) had significantly lower bouton density than cells at both P15 (N = 80, M = 0.11, SEM = 0.005), p < .001, d = 1.72, and P30 (N = 79, M = 0.09, SEM = 0.004), p < .001, d = 1.38. Furthermore, P15 cells had a significantly higher bouton density than did P30 cells, p = .036, d = 0.40.

The means and their standard errors for all the somatic variables, with significance levels indicated, are represented in Figure 13. Tables displaying the descriptive statistics and confidence intervals for each variable for each age group, as well as the complete results from the Games-Howell post hoc analysis, including data on changes in somatic perimeter, are included in appendix III. Figures depicting cell bodies with apposing PV+ terminals from each age group is included in appendix I.

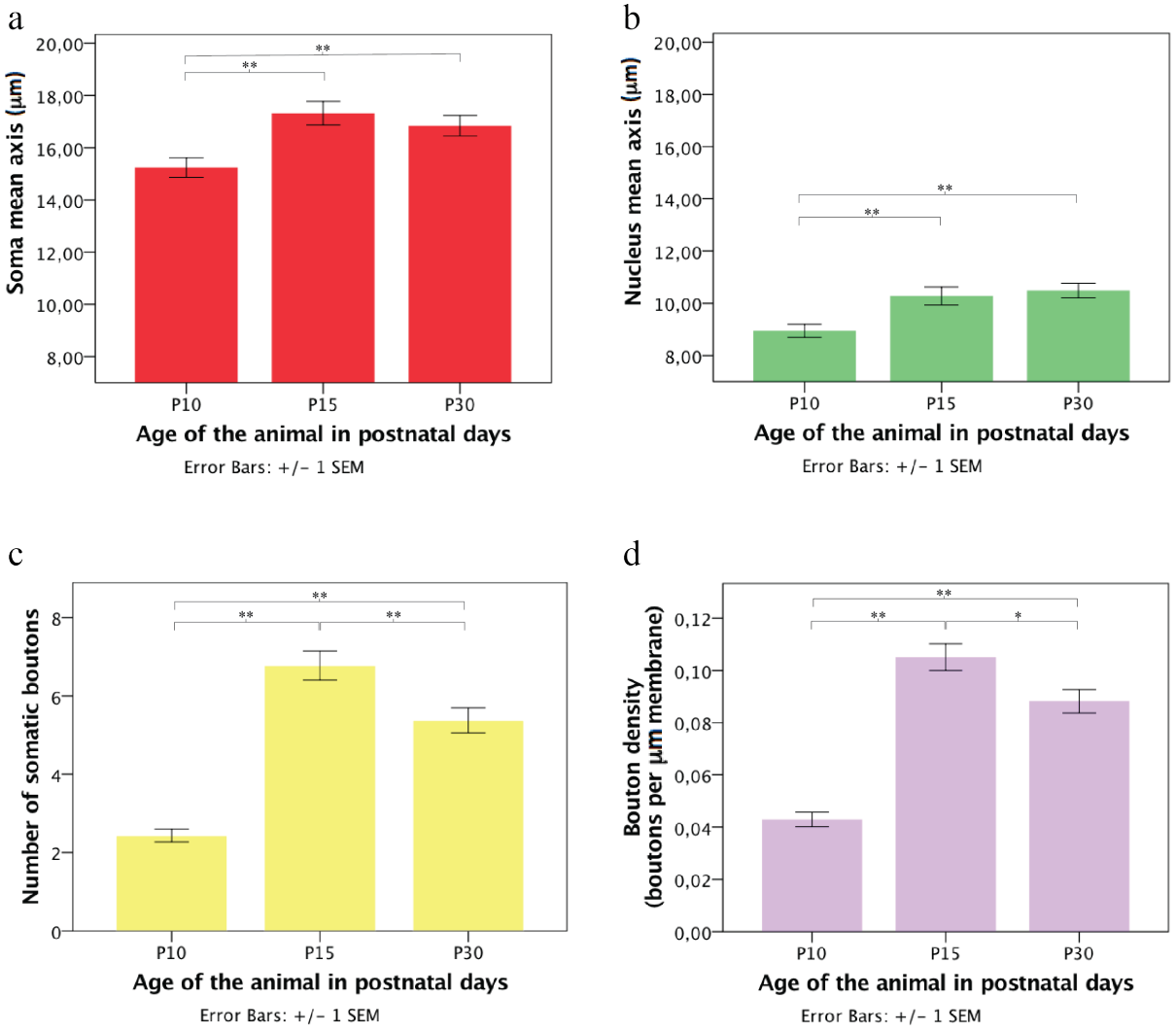

Figure 13. Bar charts showing the means and standard errors for somatic variables across age groups. The average somatic and nucleus mean axis for each age group is represented in **a)** and **b),** respectively. **c)** shows the average numbers of PV+ boutons per somata. In **d)**, the bouton density for each group is shown. * $p < .05$ ** $p < .01$

3.3.2 Bouton variables

A one-way ANOVA was carried out to look for age-related changes in the bouton variables, i.e. area, aspect ratio, and number of mitochondria. Levene's test showed unequal variances between the groups for all these measures (details can be found in appendix III), and consequently Welch's F is reported here. The analysis revealed significant differences between the age groups in terms of bouton area, F (2, 461) = 29.95, $p < .001$. The same was true for aspect ratio, F (2, 615) = 49.93, $p < .001$, and number of mitochondria, F (2, 561) = 34.96, $p < .001$. Again, a Games-Howell post hoc analysis was performed for pairwise comparisons between all groups.

The mean area of boutons from P10 (N = 188, M = 0.53, SEM = 0.03) was larger than that of P15 boutons (N = 526, M = 0.36, SEM = 0.01), and this difference was significant, p < .001, d = 0.49. The mean bouton area at P15 was also significantly smaller than that at P30 (N = 427, M = 0.48, SEM = 0.01), p < .001, d = 0.44. Although boutons from P30 were slightly smaller than those at P10, this difference was non-significant, p = .287, d = 0.14.

The aspect ratio of boutons was smaller at P10 (N = 190, M = 1.71, SEM = 0.05) than at P15 (N = 527, M = 2.29, SEM = 0.05), p < .001, d = 0.65 and P30 (N = 427, M = 2.33, SEM = 0.05), p < .001, d = 0.71. The slightly larger aspect ratio of boutons from P30 as compared to those at P15 was non-significant, p = .870, d = 0.03.

P30 boutons had on average significantly more mitochondria (N = 430, M = 0.76, SEM = 0.04) than boutons at P10 (N = 195, M = 0.35, SEM = 0.04), p < .001, d = 0.62, and boutons at P15 (N = 542, M = 0.44, SEM = 0.03), p < .001, d = 0.46. While P15 boutons had on average slightly more mitochondria than P10 boutons, this difference did not reach significance, p = .183, d = 0.15. The mitochondria seen in P10 and P15 boutons generally seemed smaller and less developed in terms of their cristae than those at P30.

An additional observation was that PV+ axonal varicosities linking the somatic terminals seemed more abundant at P30 than at both earlier stages. Terminals from each age group are depicted in Figure 14, and more images are included in appendix I.

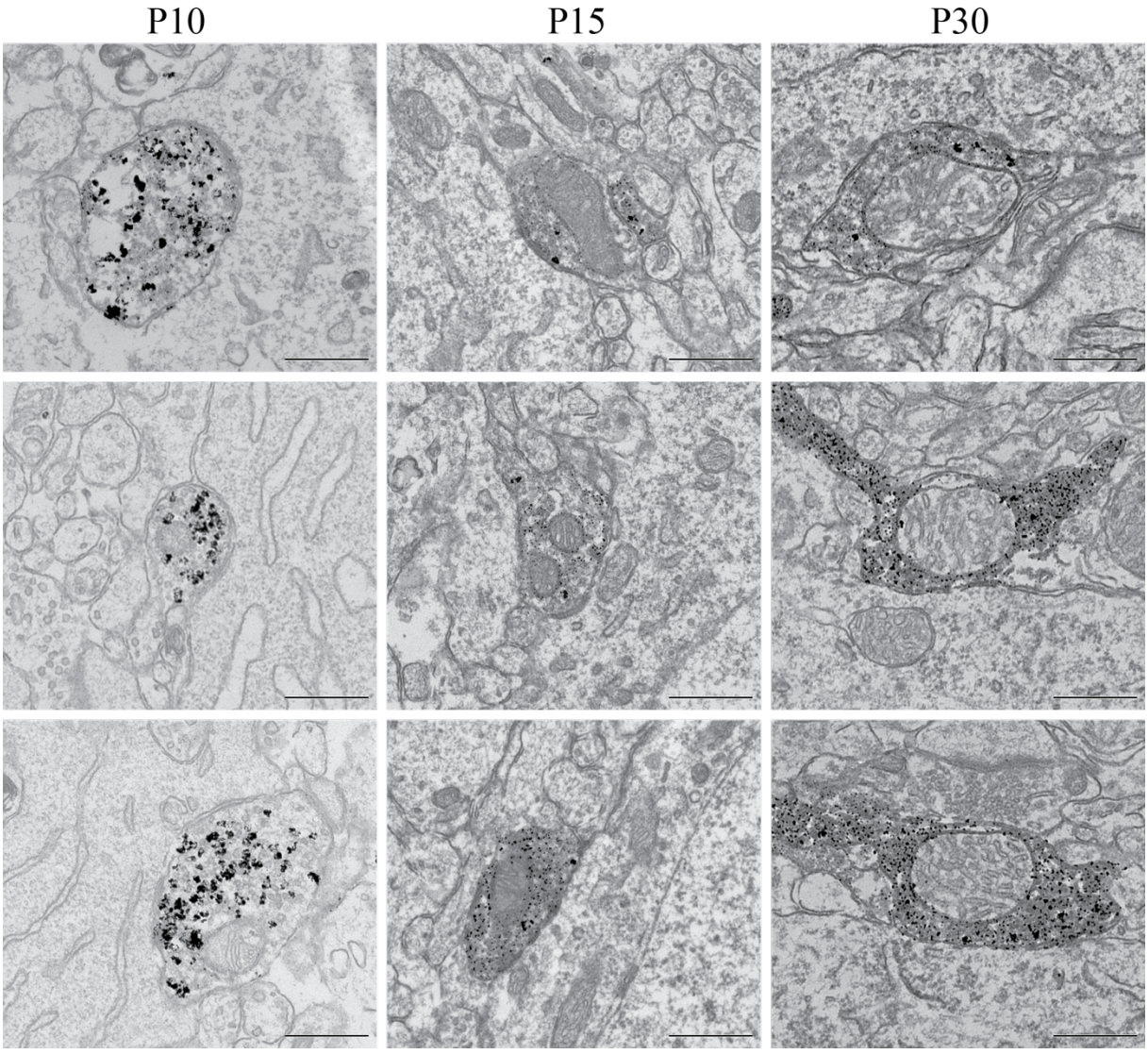

Figure 14. PV+ somatic terminals from different age groups. Scale bars are 500 nm. More images of terminals from all age groups are included in appendix I.

The means and their standard errors for the bouton variables, with significance levels indicated, are represented in Figure 15. A table of the descriptive statistics and confidence intervals for each variable for each age group, as well as the complete results from the Games-Howell post hoc analysis, including data on changes in long and short axis of boutons, are included in appendix III.

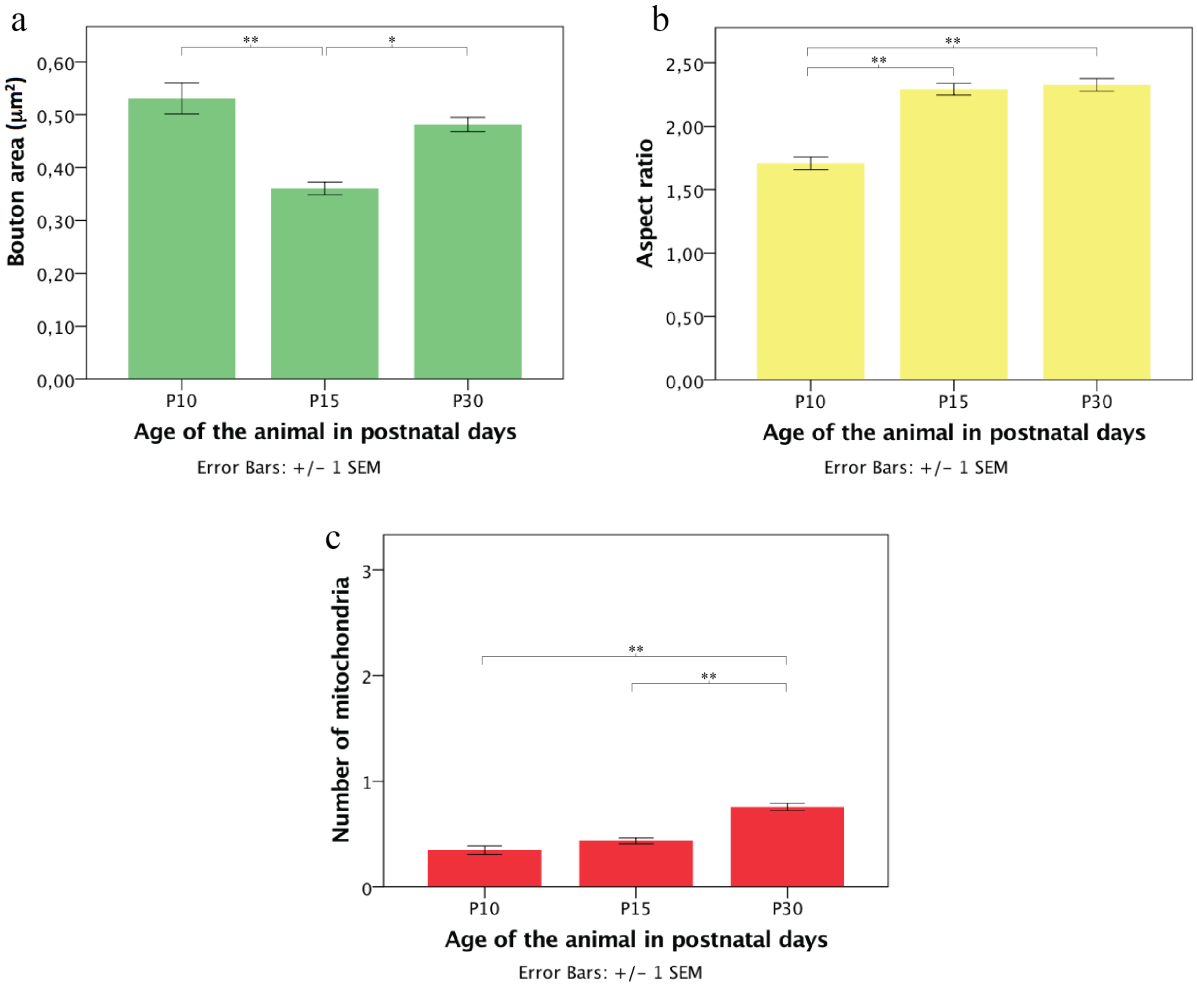

Figure 15. Bar charts showing the means and their standard errors from the bouton variables across age groups. The bar charts display means across age groups for **a)** bouton area, **b)** bouton aspect ratio and **c)** number of mitochondria per bouton. * $p < .05$ ** $p < .01$

3.3.3 Comparison of putative interneurons versus principal cells

Because the presence of deep nuclear indentations is a typical ultrastructural feature of interneurons, an attempt was made to subdivide the material in this study on this basis. Cells that had deeply indented nuclei were categorized as interneurons, cells with smooth nuclear membranes as principal neurons, and those with shallow indentations were excluded. This gave ~6% and 10% interneurons and ~72% and ~65% principal cells for P15 and P30, respectively. Thus, unclassified cells comprised ~22% of cells at P15 and ~27% at P30. The groups of interneurons were so small that statistical analyses became problematic. Nevertheless, one key observation was made when inspecting the descriptive statistics: at P15, the average number of PV+ boutons targeting interneurons, $M = 10.20$ was high ($N = 5$, $SD = 3.56$) compared to the average for principal cells, $M = 6.33$ ($N = 57$, $SD = 3.05$). At P30, however, the mean number

of PV+ boutons were more similar between the groups; specifically, $M = 6.13$, $SD = 2.36$ for interneurons ($N = 8$) versus $M = 4.90$, $SD = 2.56$ for principal cells ($N = 50$).

3.3.4 Comparison of animals within age groups

To check for differences between animals within the P10 and P30 groups, an independent Student's t-test was carried out on all soma and bouton variables of the two animals in each of these groups. Only significant differences will be reported here, but tables summarizing all the results from these t-tests can be found in appendix III.

In the P30 group, size measurements from one of the animals, P30-4, were on average smaller than those made from the other one, P30-6. The mean axis of the soma of cells from P30-4 ($N = 44$, $M = 15.71$, $SEM = 0.48$) was smaller than that of cells from P30-6 ($N = 36$, $M = 18.22$, $SEM = 0.57$). The mean difference, –2.51, was significant $t(78) = –3.40$, $p = .001$, $d = 0.77$. Also, the mean axis of the nucleus was smaller in cells from P30-4 ($N = 42$, $M = 9.65$, $SEM = 0.36$) than in cells from P30-6 ($N = 34$, $M = 11.53$, $SEM = 0.38$), and the mean difference, –1.88, was significant, $t(74) = –3.59$, $p = .001$, $d = 0.83$. Lastly, the boutons from P30-4 ($N = 254$, $M = 0.44$, $SEM = 0.02$) were on average smaller than that of those from P30-6 ($N = 173$, $M = 0.54$, $SEM = 0.02$); the mean difference, –0.11, was significant $t(425) = –3.95$, $p < .001$, $d = 0.36$. Furthermore, the bouton density of cells from P30-4 ($N = 43$, $M = 0.10$, $SEM = 0.01$) was higher than that for P30-6 ($N = 36$, $M = 0.07$, $SEM = 0.01$), yielding a mean difference of 0.03. This difference was significant $t(77) = 3.64$, $p < .001$, $d = 0.82$.

Between P10 animals, no significant differences in soma or bouton variables were found except for a difference in aspect ratio. The aspect ratio of boutons from P10-3 ($N = 78$, $M = 1.60$, $SEM = 0.06$) was slightly smaller than that of P10-4 ($N = 112$, $M = 1.78$, $SEM = 0.07$), and the mean difference, –0.19, was just significant, $t(188) = –1.97$, $p = .050$, $d = 0.27$.

4 Discussion

4.1 Methodological considerations

4.1.1 Chemical fixation and ultrastructure

Fixation of biological specimen is instrumental in electron microscopy, and traditional methods of fixation uses chemicals, such as GA and PFA. For brain tissue, this treatment is known to cause shrinkage and loss of extracellular space, thus distorting tissue ultrastructure (Korogod et al. 2015). This is a serious problem for quantitative assessments, and also indicates that what is seen in the EM can be quite different from the situation in the CNS *in vivo*.

4.1.2 Labelling issues for electron microscopy

Proper penetration of antibody is a common issue in electron microscopy, due to the concurrent need to preserve the ultrastructural integrity of the tissue. Because of the delicate nature of tissue from very young brains, treating the material from P10 the same way as that from the others was not an option. In theory, the penetration of the antibody could have been relatively poorer compared to that of the other age groups, but the P10 tissue appeared to be easier to penetrate to begin with. The myelin is less developed at this age (Downes & Mullins 2014), which possibly accounts for this effect. Tissue from P15 and P30 was treated in the same way, but it is possible that P15 tissue is easier to penetrate than that from P30. These factors could have led to differences in labelling between age groups, but as the extent of antibody penetration was no more than approximately 3-4 μm across age groups, differences seemed small. To minimize potential differences in penetration, attention was paid to consistently sample cells near the surface of the tissue across all age groups.

Due to a fault in the protocol, the material from the P10 brains was insufficiently rinsed between the steps of ABC incubation and DAB reaction. As such, excess ABC-complexes were not completely removed, causing the enzyme reaction to occur in the solution as well as at antibody binding sites. This seemed to result in some unspecific gold deposits. These deposits were larger than the label should be (the gold particles should be approximately 10 nm in size), and thus a terminal was not considered labelled unless it contained such small grains of gold. The material from P15 and P30 was processed in another experiment, and were properly rinsed between ABC incubation and DAB staining. The level of background labelling in this material, as assessed by inspecting the negative control, was negligible.

Aggregated vesicles in the presynaptic profile is an important criterion for identifying a synapse (Gray & Guillery 1966), but this feature was generally obscured by the dense labelling in this study. Therefore, errors in synapse counting cannot be ruled out. However, as all counts are done in the same way by the same investigator, the relative numbers should be accurate.

4.1.3 Cell size differences between P30 animals

The cells from one of the two animals aged P30 had an average mean axis that was lower than the average for cells from P15. In fact, these cells' mean axes were on average almost as small as those from P10 cells, which might not reflect the real size relationship of cells from these age groups. Cells sampled from the other animal aged P30 had a slightly larger mean axis than the average for P15 cells. Other size measurements showed similar patterns, including the mean axis of the nucleus and the area of the apposing boutons.

The reason for this has to be considered. Each thin section only contained layers I-III of the dorsal MEC. Cells in LII are bigger than cells in LIII, as well as cells of surrounding (non-MEC) regions (Boccara et al. 2015). LI is virtually acellular, and therefore easily recognizable in the EM. Occasional cells from LIII might have been sampled by mistake, so the smaller cells of the one animal could be the result of a systematic sampling from LIII instead of LII. Given the meticulous attention that was paid to identifying and sampling from LII throughout the process, a systematically larger sampling from one of these layers in one of the animals nevertheless seems highly unlikely.

It should be mentioned that the two P30 animals were not from the same litter. Still, it is unlikely that individual differences, even in animals from different litters, can account for such a variation in cell size within a layer of the MEC (GM Olsen, personal communication, 2016). The variations are therefore more likely related to the treatment of the tissue. One of the brains had been received months before the other one, and had consequently been stored on the fixative (4% PFA and 0.1% GA in 0.1M PBS) for approximately two months prior to sectioning. As mentioned, shrinking of tissue is a problem with chemical fixation (Korogod et al. 2015), and prolonged storage on fixative causes secondary shrinking (Bahr et al. 1957). Although no obvious shrinking artifacts were seen in the tissue from the brain that had been stored the longest, size measurements might have been affected. This is supported by the finding that not only the average sizes of the somatic measurements, but also the average size of the terminals, was significantly smaller in the tissue that had been stored the longest.

4.1.4 Limited dataset

The final data used for analysis in this project is limited, originating from a total of 10 animals. Five of these were used for EM (two each from the ages of P10 and P30, and one from P15), and five were used for LM (two each from the ages of P15 and P30, and one from the age of P10). Thus, the results will need to be verified in a study with more animals, and conclusions are at this point very tentative.

4.2 Light microscopic findings

4.2.1 Parvalbumin immunoreactivity at P10 and laminar pattern of development

General features of the PV development, such as overall amount of labelled profiles and their laminar distribution, were investigated by use of immunohistochemistry for LM. PV immunoreactivity is quite delayed compared to other cytochemical contents; it was noted by Solbach and Celio (1991) around P4 in some regions of the hippocampus, but was only clearly visible by P7. This is slightly earlier than the emergence of PV immunoreactivity in the neocortex, where the first stained cell bodies have been seen at P8 and immunoreactive fibers have been noted earliest at P11 (Alcántara & Ferrer 1994).

In the current study, extensive PV immunoreactivity was observed in the MEC at P10, and this labelling was largely limited to the superficial layers I-III. This is in contrast to early studies of the development of PV immunoreactivity in the rat and mouse neocortex, where PV+ cells were first found in LV and only progressively developed in more superficial layers and LVIa. Even at P12, the superficial layers in neocortical regions were only very faintly stained (Soriano et al. 1992; Alcántara et al. 1993; del Río et al. 1994), and similar patterns have been demonstrated in the neocortex of the cat (Alcántara & Ferrer 1994) and monkey (Erickson & Lewis 2002). An inside-out gradient in the emergence of PV+ cells, resembling the traditional laminar pattern of cortical development, has been reported in the human neocortex (Honig et al. 1991). These results indicate that although the exact laminar route might vary, PV+ cells in the neocortex first appears in deeper layers across a number of species. Certainly, only a narrow band of labelled cells deep in the cortical thickness, probably corresponding to LV, was observed in the visual cortex at P10 in this study. In contrast, the MEC at this age exhibited a thick, dark band of cells in LII, and a less dense yet even broader band of cells in LIII. Only in the ventral-most region was there a clear lamina dissecans and PV+ cells deeper in the cortex, but based on comparisons with the atlas provided by Boccara et al. (2015) this deeper region likely corresponds to the PaS. Since we did not capture the beginning of PV immunoreactivity

in the MEC in our study, it cannot be concluded here when and where PV is first expressed in the MEC. However, the current findings suggest that the MEC follows a laminar ontogenetic route of PV immunoreactivity that does not mirror the one reported in the phylogenetically newer neocortex (Soriano et al. 1992; Alcántara et al. 1993). In the EC of fetal monkeys, the first PV+ neurons were found in layers III-V, and only later in LII (Berger et al. 1999), suggesting that the laminar pattern of PV development might be less similar across species in the EC than in the neocortex.

Alcantara and colleagues (1993) did not report PV+ fibers in any neocortical region of the rat before the age of P11. In the current study, PV+ axonal and dendritic arborizations was seen in the MEC at P10, and putative boutons identified at the LM level at P10 was later confirmed at the EM level. This suggests that PV+ cells and arbors might appear relatively earlier in the MEC than in the neocortex. Still, a prominent increase in PV immunoreactivity in the MEC was observed here between P10 and P15, and in superficial layers this increase in labelling mainly seemed related to the general amount of PV+ arbors. Thus, important changes might occur in the local connectivity of PV+ cells during this time. Some of these changes were addressed here by EM and will be detailed below.

4.2.2 Dorsoventral gradient

In this study, a dorsoventral gradient was visible at P10 in the density of PV+ dendrites reaching into LI, and LII also looked more heavily stained with PV+ arbors in the dorsal region. This gradient was not apparent at later stages. Beed and colleagues (2013) reported a gradient in the amount of PV+ axonal arborizations and terminals in LII of the juvenile (P15-25) rat MEC. If there is a corresponding gradient in the PV+ dendritic processes reaching LI, it might be visible here at P10 because the tissue is lightly stained overall. This gradient is most likely not discernible at later stages due to the increased amount of labeled dendritic profiles across the dorsoventral axis. Recently, Ray and Brecht (2016) reported a dorsoventral gradient in the maturation of several aspects of pyramidal cells in LII. It would thus also be conceivable that the gradient seen in density of immunoreactivity at P10 reflects a dorsoventral gradient in the maturation process. If so, this would strengthen the suggestion put forward by Ray and Brecht (2016) that small-scale grid representations – located to the dorsal MEC – mature on an earlier time scale than large-scale ones. Future studies might be designed to investigate this possibility further. As only the dorsal-most MEC was selected for EM analysis in this study, further discussion relates to this region only.

4.3 Electron microscopic findings

Changes in the local output from PV+ basket cells in MEC LII were investigated in ultrathin sections by use of EM. The somata were selected from all PV– cells in MEC LII. The samples will thus include principal cells of the stellate and pyramidal type, and interneurons classified as multipolar cells, bipolar cells, and cholecystokinin positive basket cells (Canto et al. 2008). Given that about 13% of the MEC LII cell population are interneurons (Tang et al. 2014), and that half of these are PV+ (Miettinen et al. 1996) and thus not sampled here, the vast majority of the cells should represent the principal cell population. Since it is easier to define the border between LI and LII than the one between LII and LIII under the EM, it is possible that superficial cells are relatively more represented than those deeper in LII. Stellate cells are preferentially located to the superficial part of the layer, meaning they might have been sampled here to a greater degree than pyramidal cells.

The analysis revealed several significant differences in ultrastructural and connectional features across age groups. These include changes in the size of PV– somata and nuclei; changes in both the absolute number and the density of PV+ boutons approaching the PV– somata; a U-shaped trend for the size of the boutons; changes in the shape of the boutons as measured by aspect ratio; lastly, changes were seen in the number and size of mitochondria in the boutons. The main differences are illustrated in Figure 16 and will be discussed in the following text.

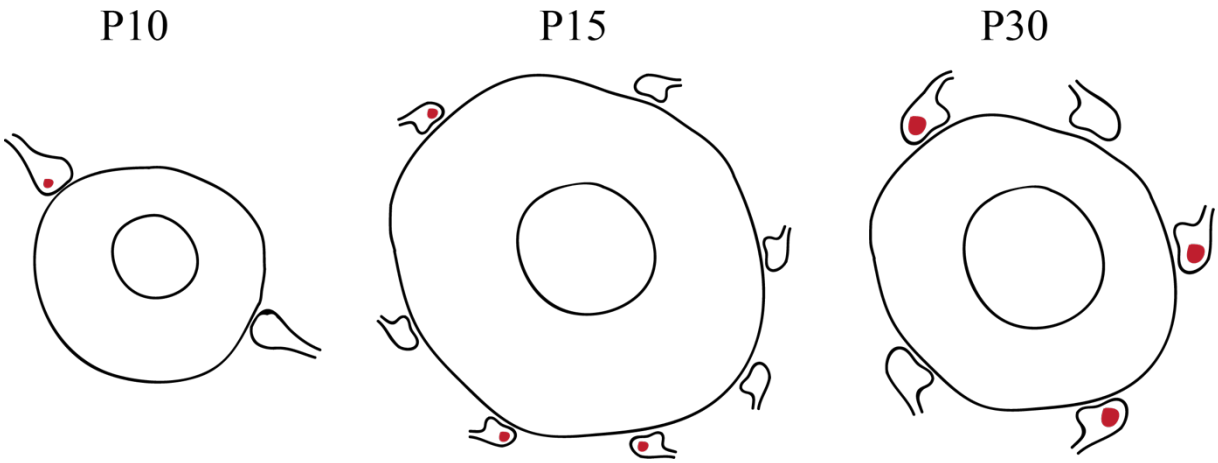

Figure 16. The average observations for PV+ terminals and their target PV– cell bodies across age groups. Mitochondria are illustrated as red circles.

4.3.1 Changes in the somata receiving parvalbumin positive input

The somata were morphologically heterogeneous across age groups, but most commonly round, ellipsoid or multipolar. The variation within groups seemed larger than that between them. The

relatively low number of pyramidal cells noted could reflect a bias of sampling to the more superficial part of the layer, as mentioned above. Because the PV– cells sampled in this study represent such a diverse group of cells, it would likely be better to approach the question of their morphological development with identified cell classes.

Previous studies of neocortical areas have demonstrated a steady increase in cell size throughout the first three postnatal weeks with the steepest growth prior to P15 (Eayrs & Goodhead 1959; Miller 1981; Miller & Peters 1981). Therefore, the increased cell size seen here between P10 and P15 was expected, but the slight decrease in cell size between P15 and P30 was not (see Figure 16). The fact that continuous growth has been seen in earlier studies suggests that the shrinking of the cells seen in the current study is likely due to different treatment of one of the P30 brains (see section 4.1.4). The size of the nucleus increases steadily throughout the period investigated here (Figure 16), but becomes significantly larger only between P10 and P15. Somal growth and morphological elaboration of the dendritic tree is thought to occur in concert with synaptogenesis, and only the most developed cells receive all the synaptic types seen in adult cells (Tyzio et al. 1999). Thus, the increase in somal size seen here between P10 and P15 is likely to be required for maturation of the cell's input.

Somatic spines were observed quite frequently at P10, but less often at P15 and rarely at P30. These structures are though to be relatively transient as they are abundant during development but rare in adult rats, and their decreased abundance seen here is in accordance with what has been reported for principal cells in the cerebellum and visual cortex of rats (Altman 1972; Miller & Peters 1981). The presence of spines is thought to reflect high physiological activity (Seress & Ribak 1992), and their relative abundance in immature cells may thus be a result of the large-scale activity occurring in the developing brain (Ben-Ari et al. 1989).

While deep nuclear indentations were not observed at P10, a portion of the cells displayed them at P15. Five cells, or 6%, had deep indentations at P15. The subgroup with indented nuclei increased both in number and in the depth of the indentations after P15, and at P30 approximately 10% of the cells displayed deep indentations. As previously mentioned, this is thought to be a feature common to interneurons (Parnavelas & Lieberman 1979). Such a geometry is induced upon high levels of activity, forming small compartments of cytoplasm within the space of the indentation that facilitate rapid exchange of Ca^{2+} between the cytoplasm and nucleus (Wittmann et al. 2009). Ca^{2+} signals are important in translating synaptic activity into changes in gene expression, and both their amplitude and temporal precision are elevated in indented nuclei (Wittmann et al. 2009; Queisser et al. 2011). As interneurons in the adult

CNS are known to be highly active cells (Buzsáki et al. 2007), it is conceivable that the appearance of nuclear indentations is a sign of increased and more adult-like activity patterns of these cells. The developmental timeline of nuclear indentations seen here is similar to that of basket cells in the hippocampus (Seress & Ribak 1990) and PV+ cells in LII of the MEC (Paulsen 2016), where they also appeared approximately at P15.

4.3.2 Changes in parvalbumin positive somatic boutons

4.3.2.1 Synaptic overshoot and pruning. Refinement is commonly achieved by synapse pruning in the developing nervous system (Blue & Parnavelas 1983; Li et al. 2011). However, the timeline of pruning, as well as which types of connections are pruned and to what degree, seems to be highly area and even cell type-specific (Fish et al. 2013). In this study, a significant increase in PV+ somatic boutons between P10 and P15 was observed. The number and density of PV+ somatic terminals subsequently decreased between P15 and P30 (see Figure 16).

The increase in PV+ boutons between P10 and P15 could be due either to an increase in the number of terminals, or to the emergence of the PV protein in already existing boutons. The latter alternative could be favored based on the observation that somatic terminals are present before immunoreactivity to PV emerges (Seress & Ribak 1990). However, studies using *in-vivo* imaging have demonstrated that growth and pruning of axonal branches are simultaneous and very dynamic processes where major changes occur on the time-scale of hours (Witte et al. 1996; Portera-Cailliau et al. 2005). Therefore, a sequential process of synaptogenesis, immunoreactivity appearance and pruning seems untenable. Changes in bouton densities seen on the time scale of weeks (as investigated here) is likely a product of the balance of synaptogenesis and pruning (Portera-Cailliau et al. 2005), which over time could favor increases or decreases in the number of axon terminals.

Assuming that these processes are simultaneous, the current results indicate that between P10 and P15, the rate of formation of somatic terminals is relatively higher than the rate of their pruning. Over the days between these age groups, then, a high number of terminals are formed, and a subset of them are pruned, so that the result after five days would be a net increase in their number. When comparing P15 and P30, on the other hand, a net decrease in the number of somatic terminals was seen in this study. This indicates that during this period, more terminals are pruned than are formed. Taken together, this line of thought suggests that some time between P15 and P30, the balance between formation and pruning of terminals is shifted. Due to the time gap between the two older age groups, it cannot be concluded exactly

when. It might be that an even larger peak occurs prior to P15 and that the pruning had already started at this stage. Alternatively, the number of terminals might increase even more after P15 before decreasing to the levels seen here at P30. However, the end of the second postnatal week in rodents is a time for developmental milestones: GABA has obtained its adult functional role as an inhibitory transmitter, indicating that the morphological growth and elaboration of neurons is largely finished (Ganguly et al. 2001; Ben-Ari 2002); interneurons in the hippocampus show adult-like ultrastructure (Seress & Ribak 1990), and arguably so does PV+ neurons in LII of the MEC (Paulsen 2016); eye-lids are generally unsealing and outbound experience can start. This last point is important, because given the role of experience in refinement of other systems (Chattopadhyaya et al. 2004; Jiao et al. 2006; Li et al. 2011), outbound spatial experience is likely to play a role in the refinement of the connectivity in LII of the MEC. Hence, the start of this process is likely coupled to eye-opening, which in rats occurs between P13 and P15 (Brunjes & Alberts 1981), and upon which exploration can begin. Taken together, several lines of evidence suggest that the end of the second postnatal week would be a good time point for starting the refinement of the connectivity to finally achieve intricate adult neural networks.

The pruning might be done prior to, or continue after P30. The latter alternative might seem likely given that Wouterlood et al. (1995) in their study of the whole adult rat EC only observed up to six PV+ terminals per cell body per thin section. In the current study, up to 15 PV+ somatic terminals were observed per soma per thin section at P30. However, it is important to emphasize that differences in methods of immunohistochemistry can have large effects on the amount of labelled profiles seen.

Pruning of synaptic contacts is thought to be achieved in two main ways (Goda & Davis 2003). Input elimination leads to a loss of *all* synapses between a pre- and postsynaptic cell, thus it is a 'winner-takes-all'-process in which a single presynaptic cell eventually forms all the input to the postsynaptic target. However, pruning can also occur at the level of a single synapse, so-called synapse disassembly. In this case, there is a loss of one or a small number of synapses targeting a cell, without complete input elimination (Goda & Davis 2003). Does the pruning seen here represent input elimination or synapse disassembly? At the neuromuscular junction and in the cerebellum, pruning of synapses eventually leads to elimination of all contact points originating from all but one innervating cell (Brown et al. 1976; Crepel 1982). However, in cortical microcircuits, convergent input from several basket cells are likely to reach the somata of principal cells in a given area (Bezaire & Soltesz 2013). Input elimination might still occur during development in the sense that some but not all of the innervating cells might

retract their axons, i.e. decreased convergence, which has been seen during development of the optic tectum of the frog (Li et al. 2011). Furthermore, elimination might occur at the level of single synapses (Bastrikova et al. 2008), in that an input source might retract some but not all of its axonal boutons. These options are not mutually exclusive: some inputs might be eliminated altogether (leading to decreased convergence) while others might disassemble some but not all of their axonal boutons (leading to weakening of input sources).

Interestingly, Portera-Cailliau et al. (2005) demonstrated two modes of axonal pruning in the neocortex of postnatal mice *in vivo*. One led to the degeneration of long-range axons from the thalamus, while the other involved the retraction of individual axonal branches from local interneurons. These two modes may represent input elimination and synapse disassembly, respectively, and the results also indicate that these strategies of pruning differentially affect axons from long-range and local projections. Regardless of exactly how it is achieved, pruning of basket terminals in LII of the MEC probably leads to a relative strengthening and weakening of connections based on experience-dependent activity. These processes are likely to be instrumental in the proper wiring of the adult network, which will in turn be important for the functional properties of the local spatial cells.

4.3.2.2 Ultrastructural changes in parvalbumin positive boutons. While the average area of terminals decreased from P10 to P15, those seen at the age of P30 were significantly larger than at P15. This might be related to other ongoing changes in the network in this period. At P10, GABA has been shown to still depolarize the majority of hippocampal neurons (Ganguly et al. 2001), indicating that a large fraction of the synaptic contacts seen at this stage exert excitatory effects. Furthermore, a study of basket cells in the neocortex of mice revealed that they did not display the adult FS phenotype before approximately P18 (Goldberg et al. 2011), so it is unlikely that PV+ cells in the MEC does so. The rat has not yet opened its eyes and is confined to the nest. The large terminals seen at P10 might be involved in driving this early growth of cells and connections in the local network, possibly by GABAergic, large scale depolarizing activity (Ben-Ari et al. 1989). As mentioned, the increase in number of terminals seen between P10 and P15 likely reflects a rate of terminal formation that is larger than the rate of their pruning. Still, the turnover rate of axonal branches can be extremely high in developing networks, and possibly it might be too high to allow for any growth in size of individual terminals. The result of this balance could be a rapid increase in terminal numbers, where quantity is preferred over size.

Between P15 and P30, it seemed that pruning of PV+ terminals and a strengthening of remaining ones occurred simultaneously. Indeed, it has been showed at the neuromuscular junction that the retraction of one terminal is followed by the expansion of another; in this way, a remaining synapse rapidly takes over the postsynaptic machinery of a retracting terminal (Walsh & Lichtman 2003). The result after the pruning is completed, then, is larger terminals in fewer numbers. In the auditory cortex, the elimination of a large extent of inhibitory synapses is followed by a functional strengthening of the remaining connections (Kim & Kandler 2003). Studying the optic tectum of the frog by time-lapse *in vivo* imaging and EM reconstructions, Li and colleagues (2011) showed that while some terminals retract, others mature and thus grow in strength. These studies supports the notion that pruning and strengthening of terminals are simultaneous processes during development, processes that might even be intimately coupled (Walsh & Lichtman 2003). Thus, the increased bouton size occurring with synapse pruning between P15 and P30 in this study might be the structural basis for a strengthening of selected terminals.

The changes in number and appearance of mitochondria seen in this study further supports the idea that a strengthening of individual terminals occurs in parallel with synaptic pruning between P15 and P30. Far from every one of the terminal boutons examined here contained one or more mitochondria, even at P30. However, the average number of mitochondria was significantly higher at P30 than the other stages. Furthermore, the mitochondria seen at P30 generally looked larger and more developed in terms of cristae. It seems likely that they do get bigger, as large mitochondria is a common feature of adult symmetrical synapses (Bähr & Wolff 1985). These trends might indicate that the terminals at P10 and P15 do not yet show the extent of metabolic activity that is to come, which is consistent with the idea that the FS phenotype is likely not yet expressed at these stages (Goldberg et al. 2011). Similar ultrastructural changes, i.e. larger terminals with more mitochondria, have been seen in the neocortex of the developing rat (Dyson & Jones 1980).

The aspect ratio of the terminals increased significantly from P10 to P15, but then remained virtually the same between P15 and P30. The mean aspect ratios of the two P10 animals were significantly different, which might reflect individual differences during the developmental process. However, the group mean of P10 was still significantly smaller than that of other age groups, hence the boutons obtained a more elliptical shape after P10. One possibility is that this more change in shape results from a larger portion of the axon terminals becoming 'boutons *en passant*', a typical feature of basket cell axons (DeFelipe & Fairén 1982) where the terminals appear as beads on a string. This contrasts with the organization seen at

P10, when most of the boutons form isolated, single terminals; these might be 'boutons terminaux' (Takahashi-Iwanaga 1992), which could make them appear rounder in the EM. The increased aspect ratio of the terminals might thus indicate that basket cells are starting to form their rich complexes around their target cell bodies. Chattopadhyaya et al. (2004) demonstrated a progressive increase in the complexity of such perisomatic rings of PV+ basket axons in the visual cortex of mice, mainly occurring between P18 and P28. Thus, if the increased aspect ratio seen between P10 and P15 in the current study does reflect an increased organization of perisomatic rings, it seems that this occurs on a slightly earlier time-scale in LII of the MEC than in the visual cortex. This is consistent with the idea that PV+ profiles in at least the superficial layers of the MEC might develop on an earlier time scale than those in the neocortex (see section 4.2.1). However, it should be noted that PV+ bridges linking the somatic terminal seemed more abundant at P30, which might indicate that the organization of perisomatic rings does mature further between P15 and P30 in the MEC, as in the neocortex (Chattopadhyaya et al. 2004).

4.3.2.3 Large within group differences in number of terminals. The current study revealed large within-group differences in the number of terminals per cell body at P15 and P30. This could, of course, be caused by sampling at different distances from the tissue surface, so that antibody penetration would differ. It could also result from different locations of the cells along the dorsoventral axis of the MEC, where a gradient in PV+ inputs is known to exist (Beed et al. 2013). However, as the cells comprising the PV– population of the MEC is a large and diverse group with several cell types included (see beginning of section 4.3), another plausible explanation would be that different cell classes receive different proportions of PV+ inputs.

Wouterlood and colleagues (1995) noted that virtually all PV– cells in the MEC received PV+ somatic inputs, hence it is reasonable to believe that the targets of the somatic boutons sampled in this study are both interneurons and principal neurons. Given this, several options emerge as to how the density of PV+ somatic terminals could vary among cell types. There might be differences in the amount of PV+ input reaching interneurons and principal neurons. Additionally, there might be differences in the amount of PV+ inputs received by different classes of principal neurons, i.e. by the stellate versus the pyramidal populations. Different interneuron classes could be differentially targeted. There might even be subpopulations of PV+ basket cells that differ in the number of PV+ boutons they form with a postsynaptic cell.

4.3.2.3.1 Interneurons versus principal neurons. The categorization of cells into putative principal neurons and interneurons yielded a very limited number of interneurons per age group. The main observation was nevertheless that cells categorized as interneurons generally received more PV+ somatic contacts at P15 than did their principal cell counterparts. At P30, however, the number of inputs were similar for the cell groups. Thus, it is possible that the pruning of somatic PV+ boutons is more extensive for the interneuron targets. If so, this underscores the complexity and specificity of connectional development, even within a neural network. If P15 interneurons are under tighter inhibitory control it might implicate that there is less inhibition, i.e. disinhibition, of principal cells at this stage. As inhibition is vital for proper oscillatory activity of cortical networks (Freund & Buzsáki 1996), immature connectivity patterns between interneurons would be consistent with the relative lack of network synchrony seen in LII at this age (Langston et al. 2010).

It should be noted that there are at least three classes of PV– interneurons in LII of the MEC, i.e. bipolar cells, multi-polar cells, and cholecystokinin positive basket cells (Canto et al. 2008), and that these might differ in the amount of PV+ somatic input they receive both at P15 and P30.

4.3.2.3.2 Subgroups of principal neurons. Another plausible explanation that could account for large within-group differences at P15 and P30 would be if different subclasses of principal neurons received varying amounts of contacts. Notably, two major, largely non-overlapping groups of principal neurons are thought to intermingle in LII of the MEC: the reelin+ stellate cells and the calb+ pyramidal cells (Varga et al. 2010). In LII of the juvenile rat MEC, PV+ basket cells have been shown to preferentially target calb+ principal cells, forming almost 40% more perisomatic boutons onto these targets than onto the reelin+ cells (Armstrong et al. 2016). While there was no way of accurately classifying the principal cells into subclasses in this study, it does seem plausible that the large within-group differences in the P15 and P30 groups seen here is at least partly caused by such a quantitative target selectivity of PV+ cells.

Could differences in number of PV+ boutons made onto principal cell groups be linked to subgroups of PV+ basket cells? Donato and colleagues (2015) recently demonstrated that two separate groups of PV+ basket cells exist in the mouse hippocampus, cerebellum and primary motor cortex. Cells that were either born early or late during neurogenesis showed differences in the level of PV and GAD67 expression in adults, as well as in the ratio of afferent excitatory to inhibitory synaptic input they received. Furthermore, the two groups preferentially targeted deeply or superficially situated pyramidal cells in the hippocampal CA1. If subgroups

of PV+ basket cells exist within LII of the MEC, their local output could be target-selective, similarly to those in the hippocampus. However, Armstrong et al. (2015) showed that single PV+ basket cells may target both calb+ and reelin+ cells, thus target-selectivity of potential subgroups on the basis of this dichotomy is unlikely. An alternative scenario is that subgroups of PV+ basket cells, if present in the MEC, are located to different layers and thus not intermingling within LII.

4.4 Beyond the ultrastructure: implications for physiology and behavior

This study indicates that synaptic pruning, with parallel changes in the ultrastructural features of the selected terminals, is part of the maturation of the MEC network. Some speculations might be made about the implications of these changes for network function and the animals' behavior.

4.4.1 Functional effects of pruning

What might the effect be of a decrease in the number of synaptic inputs? The obvious answer might seem to be that it would lead to less functional input, in this case less PV cell-mediated inhibition of the somata of PV– cells. However, the terminals grow in size and number of mitochondria at the same time, which might indicate an effective strengthening of the remaining inputs. Furthermore, as mentioned, findings in other areas demonstrate that pruning of some synapses is indeed coupled to an effective strengthening of others (Kim & Kandler 2003; Walsh & Lichtman 2003). This indicates that functionally, synaptic pruning does not necessarily lead to less powerful input. It might be a process designed for changing not the *amount* of input but its *organization*. The strategy of a developing circuit might be building connections in large quantities, and subsequently rearranging them in an experience-dependent manner. Again, it should be emphasized that growth and pruning of axonal branches are likely to occur simultaneously in the developing CNS (Portera-Cailliau et al. 2005); however, shifts in the balance between these processes will lead to phases of net increases or decreases in terminal densities when studied over larger time-scales. The exact timelines of these processes would be expected to vary depending on the area in question, possibly based on the type of experience needed to refine the network. For example, the maturation of dopaminergic innervation in the prefrontal cortex of the rat continues until P60 (Kalsbeek et al. 1988).

4.4.2 Comparing developmental timelines

If the connectivity and ultrastructure of the intrinsic network, the physiology of the constituent cells, and the spatial capacity of an animal are all interconnected and interdependent parts of the sense of space, then it follows logically that their ontogenetic timelines should correlate. Indeed, early studies on rats' navigational abilities through postnatal development (Schenk 1985; Rudy et al. 1987) fit well with more recent studies on the ontogeny of spatial cells' physiology (Langston et al. 2010; Ainge & Langston 2012; Bjerknes et al. 2015) and intrinsic connectivity of the MEC LII (Couey et al. 2013). Figure 17 compares relevant timelines from the literature with the developmental timelines for PV+ boutons studied here.

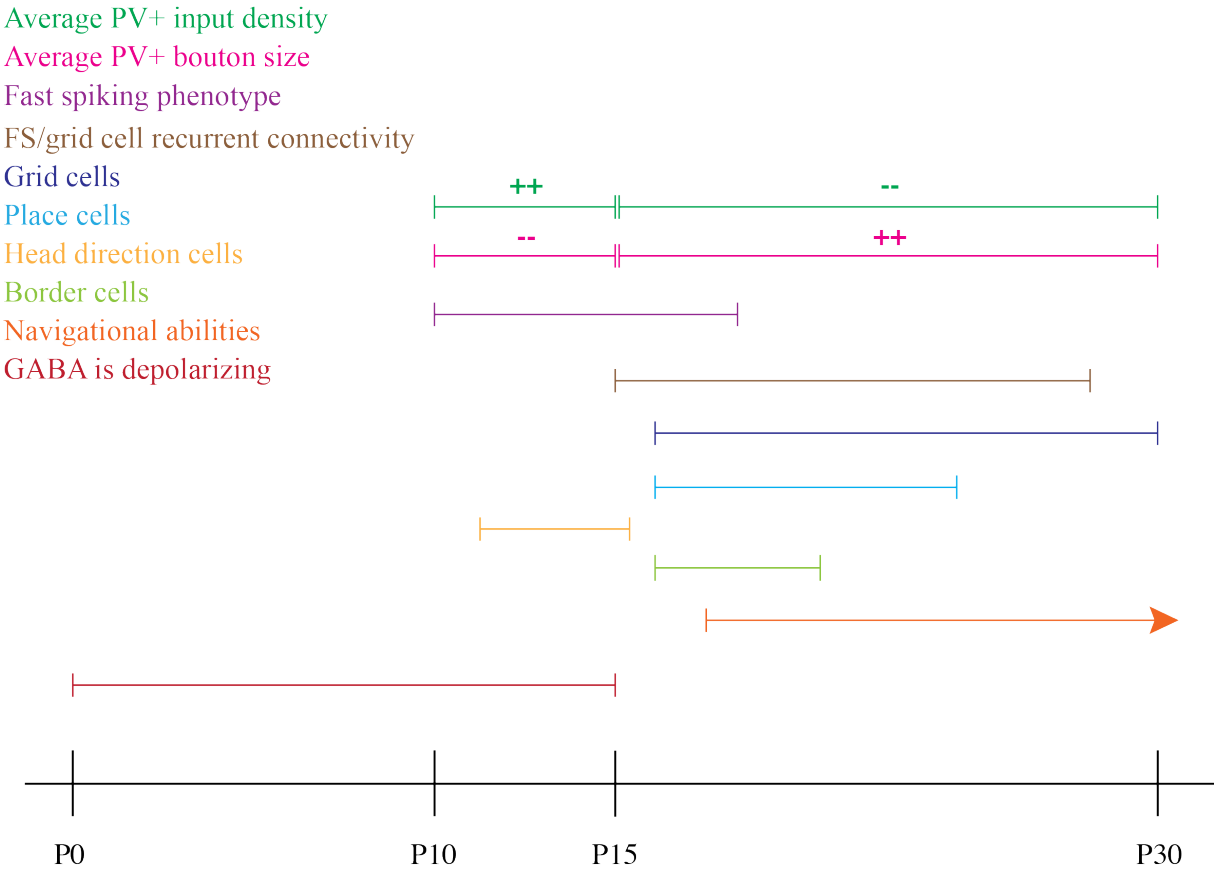

Figure 17. Comparison of developmental timelines. Timelines for development of PV+ bouton density and size (own results), spatial cell physiology (Langston et al. 2010; Wills et al. 2010; Bjerknes et al. 2014; Bjerknes et al. 2015), stellate/FS-cell recurrent connectivity (Couey et al. 2013) and navigational abilities (Schenk 1985; Rudy et al. 1987) are included. The timelines of the GABA switch (Ganguly et al. 2001) and the development of the FS phenotype (Goldberg et al. 2011) are illustrated as well, based on information from hippocampal and neocortical neurons, respectively. Major changes occur mainly after the GABA switch is completed and outbound experience starts (approximately P15). + indicates increasing values, – indicates decreasing values.

Prior to eye-opening, major changes in the effect of GABAergic signaling is likely to occur in the LII network (i.e. the GABA switch; Ganguly et al. 2001). Furthermore, the density of PV+ somatic terminals increases while their average size decreases. At the end of this period, the network in LII is still quite immature, with low levels of network synchrony and no recurrent connectivity (Langston et al. 2010; Couey et al. 2013). This could be at least partly explained by the immature state of FS cells, as these develop their physiological phenotype between P10 and P18 in the neocortex (Goldberg et al. 2011) and a similar timeline might exist in the MEC. Yet, HD cells, located in the MEC in layers deep to LII, are present from P11 and adult-like around P15 (Bjerknes et al. 2015). They are thus the only spatial cell type known to mature prior to eye-opening. It is unlikely that networks in the layers in which HD cells reside are adult-like this early, at least LIII of the rat MEC is not (Ray & Brecht 2016). Rather, the early maturation of HD cells might reflect their strong dependence on the vestibular system, the latter which matures early in postnatal development (Wills et al. 2014).

Border cells and grid cells are found in LII of the MEC. As Figure 17 shows, the grid cells show the most protracted development of all the spatial cell types, and are considered mature only around P30 (Langston et al., 2010). The distinct firing patterns of these cells thus emerge as the network builds recurrent connections between stellate and FS cells (Couey et al. 2013), and these connections are instrumental in the regulation of grid cell firing of adult mice (Buetfering et al. 2014). At least for the basket cells that target stellate cells, the pruning of PV+ somatic terminals seen in this study between P15 and P30 could be part of a rearrangement process where recurrent connectivity is the outcome. In auditory areas, pruning processes lead to sharpening of the tonotopic map (Kim & Kandler 2003); possibly, such a process in LII of the MEC contributes to a similar sharpening of grid fields. This study also indicated a strengthening of the PV+ terminals onto PV– somata in MEC LII between P15 and P30. Achieving the right strength in the inhibitory connections between PV+ cells and grid cells is probably vital for adult firing patterns to emerge. Border cells develop on a shorter time scale than grid cells (Bjerknes et al. 2014), indicating that they might rely less on recurrent connectivity with PV+ cells. Furthermore, place cells of the hippocampus mature prior to grid cells, suggesting they might not be as dependent on grid cell input as previously imagined (Moser et al. 2008).

Early studies used the Morris water maze to assess young rats' navigational skills under various training conditions, revealing a protracted postnatal development of these abilities (Schenk 1985; Rudy et al. 1987). While some rudimentary and very limited spatial abilities has been seen at P17, more robust spatial behavior has only been noted from approximately P20

(Rudy et al. 1987). Optimal adult navigational behavior regardless of training condition has been reported from P40 onwards (Schenk 1985). The extensive development of grid cells and their connectivity thus occurs during a time when rats' navigational abilities are also emerging. The fact that spatial abilities becomes more robust and adult-like even after the spatial cells' physiology and connectivity mature possibly reflects the more protracted development of relevant abilities depending on other circuits, e.g. working memory (Kalsbeek et al. 1988).

4.5 Future directions

The findings from this study indicate that in the dorsal LII of the MEC, there are extensive changes occurring in both the density and ultrastructure of PV+ basket terminals onto PV– cell bodies during postnatal development of the rat. Naturally, it would be necessary to confirm the findings in a study including more animals, especially because only one animal from the P15 group was used here. Furthermore, there seems to be large within-group differences in the number of PV+ terminals approaching PV– cell bodies, at least at P15 and P30. The techniques used here cannot reveal whether these differences can be attributed to the diversity of cell types included here. Is the pruning of terminals approaching interneurons more extensive than for those targeting principal neurons – and if so, why? There is still controversy about how grid and border cell properties relate to the cytochemical and morphological principal cell types in the MEC; are there further differences in the pruning process of input to stellate and pyramidal cells? Studies of PV+ inputs to identified cell types through development, by use of e.g. double-labelling techniques, intracellular filling or retrograde labelling could help resolve these questions.

The conclusions drawn from this study are also very tentative due to the large gap between the two older age groups. Should the findings here be confirmed in a larger-scale study, another interesting target would be to more accurately determine the age at which such maturational changes, i.e. size changes and pruning of PV+ terminals occur, and also whether changes continue through adolescence and into older adulthood.

5 Conclusion

The present study was undertaken to investigate changes in the local output from PV+ cells in LII of the MEC through the first postnatal month of the rat. To this end, immunohistochemistry protocols for LM and EM were worked out and used on sections from P10, P15 and P30 brains. 80 PV– cells were sampled from each age group and compared on several measures, with special attention to the number and morphometric features of the PV+ terminals that targeted them. The main finding was that of overshoot and pruning processes of PV+ somatic terminals onto PV– cell bodies, occurring prior to and after eye-opening (P15), respectively. Furthermore, ultrastructural features of remaining PV+ terminals mature over the period between P15 and P30. As such, this study provides some basic insights into the changes that occur in the PV+ network of LII through development. These changes occur on a similar time scale as, and might be instrumental for, the development of grid cells and the physiological maturation of the intrinsic LII network connectivity.

References

Ainge, J.A. & Langston, R.F., 2012. Ontogeny of neural circuits underlying spatial memory in the rat. *Frontiers in Neural Circuits*, 6.

Alcántara, S. & Ferrer, I., 1994. Postnatal development of parvalbumin immunoreactivity in the cerebral cortex of the cat. *The Journal of Comparative Neurology*, 348(1), pp.133–149.

Alcántara, S., Ferrer, I. & Soriano, E., 1993. Postnatal development of parvalbumin and calbindin D28K immunoreactivities in the cerebral cortex of the rat. *Anatomy and Embryology*, 188(1), pp.63–73.

Altman, J., 1972. Postnatal development of the cerebellar cortex in the rat. II. Phases in the maturation of Purkinje cells and of the molecular layer. *The Journal of Comparative Neurology*, 145(4), pp.399–463.

Armstrong, C., Wang, J., Lee, S.Y., Broderick, J., Bezaire, M.J., Lee, S-H. & Soltesz, I., 2016. Target-Selectivity of Parvalbumin-Positive Interneurons in Layer II of Medial Entorhinal Cortex in Normal and Epileptic Animals. *Hippocampus*, 26(6), pp.779–793.

Bahr, G.F., Bloom, G. & Friberg, U., 1957. Volume changes of tissues in physiological fluids during fixation in osmium tetroxide or formaldehyde and during subsequent treatment. *Experimental Cell Research*, 12(2), pp.342–355.

Bastrikova, N., Gardner, G.A., Reece, J.M., Jeromin, A. & Dudek, S.M., 2008. Synapse elimination accompanies functional plasticity in hippocampal neurons. *Proceedings of the National Academy of Sciences of the United States of America*, 105(8), pp.3123–7.

Bayer, S.A., 1980. Development of the hippocampal region in the rat. I. Neurogenesis examined with 3H-thymidine autoradiography. *The Journal of Comparative Neurology*, 190(1), pp.87–114.

Beed, P., Gundlfinger, A., Schneiderbauer, S., Song, J., Böhm, C., Burgalossi, A., Brecht, M., Vida, I. & Schmitz, D., 2013. Inhibitory gradient along the dorsoventral axis in the medial entorhinal cortex. *Neuron*, 79(6), pp.1197–1207.

Ben-Ari, Y., 2002. Excitatory actions of GABA during development: the nature of the nurture. *Nature Reviews Neuroscience*, 3(9), pp.728–739.

Ben-Ari, Y., Cherubini, E., Corradetti, R. & Gaiarsa, J-L.L., 1989. Giant synaptic potentials in immature rat CA3 hippocampal neurones. *The Journal of Physiology*, 416(1), pp.303–325.

Berger, B., De Grissac, N. & Alvarez, C., 1999. Precocious development of parvalbumin-like immunoreactive interneurons in the hippocampal formation and entorhinal cortex of the fetal cynomolgus monkey. *The Journal of Comparative Neurology*, 403(3), pp.309–31.

Bezaire, M.J. & Soltesz, I., 2013. Quantitative assessment of CA1 local circuits: knowledge base for interneuron-pyramidal cell connectivity. *Hippocampus*, 23(9), pp.751–785.

Bjerknes, T.L., Langston, R.F., Kruge, I.U., Moser, E.I. & Moser, M-B., 2015. Coherence among head direction cells before eye opening in rat pups. *Current Biology*, 25(1), pp.103–108.

Bjerknes, T.L., Dagslott, N.C., Moser, E.I. & Moser, M-B., 2014. Representation of geometrical borders in the developing rat. *Neuron*, 82(1), pp.71–78.

Blue, M.E. & Parnavelas, J.G., 1983. The formation and maturation of synapses in the visual cortex of the rat. II. Quantitative analysis. *Journal of Neurocytology*, 12(4), pp.697–712.

Boccara, C.N., Kjonigsen, L.J., Hammer, I.M., Bjaalie, J.G., Leergaard, T.B. & Witter, M.P, 2015. A three-plane architectonic atlas of the rat hippocampal region. *Hippocampus*, 25(7), pp.838–857.

Boccara, C.N., Sargolini, F., Thoresen, V.H., Solstad, T., Witter, M.P., Moser, E.I. & Moser, M-B., 2010. Grid cells in pre- and parasubiculum. *Nature Neuroscience*, 13(8), pp.987–994.

Brown, M.C., Jansen, J.K. & Van Essen, D., 1976. Polyneuronal innervation of skeletal muscle in new-born rats and its elimination during maturation. *The Journal of Physiology*, 261(2), pp.387–422.

Brunjes, P.C. & Alberts, J.R., 1981. Early auditory and visual function in normal and hyperthyroid rats. *Behavioral and Neural Biology*, 31(4), pp.393–412.

Buetfering, C., Allen, K. & Monyer, H., 2014. Parvalbumin interneurons provide grid cell-driven recurrent inhibition in the medial entorhinal cortex. *Nature Neuroscience*, 17(5), pp.710–718.

Burwell, R.D. & Amaral, D.G., 1998. Cortical afferents of the perirhinal, postrhinal, and entorhinal cortices of the rat. *The Journal of Comparative Neurology*, 398(2), pp.179–205.

Buzsáki, G., Kaila, K. & Raichle, M., 2007. Inhibition and brain work. *Neuron*, 56(5), pp.771–783.

Bähr, S. & Wolff, J.R., 1985. Postnatal development of axosomatic synapses in the rat visual cortex: morphogenesis and quantitative evaluation. *The Journal of Comparative Neurology*, 233(3), pp.405–420.

Canto, C.B. & Witter, M.P., 2012. Cellular properties of principal neurons in the rat entorhinal cortex. II. The medial entorhinal cortex. *Hippocampus*, 22(6), pp.1277–1299.

Canto, C.B., Wouterlood, F.G. & Witter, M.P., 2008. What does the anatomical organization of the entorhinal cortex tell us? *Neural Plasticity*, 2008.

Caviness, V.S., Takahashi, T. & Nowakowski, R.S., 1995. Numbers, time and neocortical neuronogenesis: a general developmental and evolutionary model. *Trends in Neurosciences*, 18(9), pp.379–383.

Chattopadhyaya, B., Di Cristo, G., Higashiyama, H., Knott, G.W., Kuhlman, S.J., Welker, E.

& Huang, Z.J., 2004. Experience and activity-dependent maturation of perisomatic GABAergic innervation in primary visual cortex during a postnatal critical period. *The Journal of Neuroscience*, 24(43), pp.9598–9611.

Chen, C. & Regehr, W.G., 2000. Developmental remodeling of the retinogeniculate synapse. *Neuron*, 28(3), pp.955–966.

Colgin, L.L., Moser, E.I. & Moser, M.B., 2008. Understanding memory through hippocampal remapping. *Trends in Neurosciences*, 31(9), pp.469–477.

Couey, J.J., Witoelar, A., Zhang, S.J., Zheng, K., Ye, J., Dunn, B., Czajkowski, R., Moser, M-B., Moser, E.I., Roudi, Y. & Witter, M.P., 2013. Recurrent inhibitory circuitry as a mechanism for grid formation. *Nature Neuroscience*, 16(3), pp.318–324.

Crepel, F., 1982. Regression of functional synapses in the immature mammalian cerebellum. *Trends in Neurosciences*, 5, pp.266–269.

DeFelipe, J. & Fairén, A., 1982. A type of basket cell in superficial layers of the cat visual cortex. A Golgi-electron microscope study. *Brain Research*, 244(1), pp.9–16.

Donato, F., Chowdhury, A., Lahr, M. & Caroni, P., 2015. Early- and late-born parvalbumin basket cell subpopulations exhibiting distinct regulation and roles in learning. *Neuron*, 85(4), pp.770–786.

Downes, N. & Mullins, P., 2014. The development of myelin in the brain of the juvenile rat. *Toxicologic Pathology*, 42(5), pp.913–922.

Dyson, S.E. & Jones, D.G., 1980. Quantitation of terminal parameters and their interrelationships in maturing central synapses: A perspective for experimental studies. *Brain Research*, 183(1), pp.43–59.

Eayrs, J.T. & Goodhead, B., 1959. Postnatal development of the cerebral cortex in the rat. *Journal of Anatomy*, 93(4), pp.385–402.

Erickson, S.L. & Lewis, D.A., 2002. Postnatal development of parvalbumin- and GABA transporter-immunoreactive axon terminals in monkey prefrontal cortex. *The Journal of comparative neurology*, 448(2), pp.186–202.

Fish, K.N., Hoftman, G.D., Sheikh, W., Kitchens, M. & Lewis, D.A., 2013. Parvalbumin-containing chandelier and basket cell boutons have distinctive modes of maturation in monkey prefrontal cortex. *The Journal of Neuroscience*, 33(19), pp.8352–8358.

Freund, T.F. & Buzsáki, G., 1996. Interneurons of the hippocampus. *Hippocampus*, 6(4), pp.347–470.

Fuchs, E.C., Neitz, A., Pinna, R., Melzer, S., Caputi, A. & Monyer, H., 2015. Local and distant input controlling excitation in layer II of the medial entorhinal cortex. *Neuron*, 89(1), pp.194–208.

Fyhn, M., Hafting, T., Treves, A., Moser, M-B. & Moser, E.I., 2007. Hippocampal remapping

and grid realignment in entorhinal cortex. *Nature*, 446(7132), pp.190–194.

Ganguly, K., Schinder, A.F., Wong, S.T. & Poo, M.M., 2001. GABA itself promotes the developmental switch of neuronal GABAergic responses from excitation to inhibition. *Cell*, 105(4), pp.521–532.

Geiger, J.R., Lübke, J., Roth, A., Frotscher, M. & Jonas, P., 1997. Submillisecond AMPA receptor-mediated signaling at a principal neuron-interneuron synapse. *Neuron*, 18(6), pp.1009–1023.

Giocomo, L.M., Zilli, E.A., Fransén, E. & Hasselmo, M.E., 2007. Temporal frequency of subthreshold oscillations scales with entorhinal grid cell field spacing. *Science*, 315(5819), pp.1719–1722.

Goda, Y. & Davis, G.W., 2003. Mechanisms of synapse assembly and disassembly. *Neuron*, 40(2), pp.243–264.

Goldberg, E.M. Jeong, H-Y., Kruglikov, I., Tremblay, R., Lazarenko, R.M. & Rudy, B., 2011. Rapid developmental maturation of neocortical FS cell intrinsic excitability. *Cerebral Cortex*, 21(3), pp.666–682.

Gozlan, H. & Ben-Ari, Y., 2003. Interneurons are the source and the targets of the first synapses formed in the rat developing hippocampal circuit. *Cerebral Cortex*, 13(6), pp.684–692.

Gulyas, A.I., Miler, R., Hajos, N. & Freund, T.F., 1993. Precision and variability in postsynaptic target selection of inhibitory cells in the hippocampal CA3 region. *European Journal of Neuroscience*, 5(12), pp.1729–1751.

Hafting, T., Fyhn, M., Molden, S., Moser, M-B. & Moser, E.I., 2005. Microstructure of a spatial map in the entorhinal cortex. *Nature*, 436(7052), pp.801–806.

Harris, K.D. & Mrsic-Flogel, T.D., 2013. Cortical connectivity and sensory coding. *Nature*, 503(7474), pp.51–58.

Hennou, S., Khalilov, I., Diabira, D., Ben-Ari, Y. & Gozlan, H., 2002. Early sequential formation of functional GABAA and glutamatergic synapses on CA1 interneurons of the rat foetal hippocampus. *European Journal of Neuroscience*, 16(2), pp.197–208.

Honig, L.S., Herrmann, K. & Shatz, C.J., 1991. Developmental changes revealed by immunohistochemical markers in human cerebral cortex. *Cerebral Cortex*, 6(6), pp.794–806.

Hu, H., Gan, J. & Jonas, P., 2014. Interneurons. Fast-spiking, parvalbumin^{+} GABAergic interneurons: from cellular design to microcircuit function. *Science*, 345(6196), p.529.

Insausti, R., Herrero, M.T. & Witter, M.P., 1997. Entorhinal cortex of the rat: cytoarchitectonic subdivisions and the origin and distribution of cortical efferents. *Hippocampus*, 7(2), pp.146–183.

Jaubert-Miazza, L., Green, E., Lo, F-S., Bui, K., Mills, J. & Guido, W., 2005. Structural and

functional composition of the developing retinogeniculate pathway in the mouse. *Visual Neuroscience*, 22(5), pp.661–676.

Jiao, Y., Zhang, C., Yanagawa, Y. & Sun, Q-Q., 2006. Major effects of sensory experiences on the neocortical inhibitory circuits. *The Journal of Neuroscience*, 26(34), pp.8691–8701.

Jones, R.S.G. & Bühl, E.H., 1993. Basket-like interneurones in layer II of the entorhinal cortex exhibit a powerful NMDA-mediated synaptic excitation. *Neuroscience Letters*, 149(1), pp.35–39.

Kalsbeek, A., Voorn, P., Buijs, R.M., Pool, C.W. & Uylings, H.B., 1988. Development of the dopaminergic innervation in the prefrontal cortex of the rat. *The Journal of Comparative Neurology*, 269(1), pp.58–72.

Kano, M. & Hashimoto, K., 2009. Synapse elimination in the central nervous system. *Current Opinion in Neurobiology*, 19(2), pp.154–161.

Kawaguchi, Y., Katsumaru, H., Kosaka, T., Heizmann, C.W. & Hama, K., 1987. Fast spiking cells in rat hippocampus (CA1 region) contain the calcium-binding protein parvalbumin. *Brain Research*, 416(2), pp.369–374.

Kim, G. & Kandler, K., 2003. Elimination and strengthening of glycinergic/GABAergic connections during tonotopic map formation. *Nature Neuroscience*, 6(3), pp.282–290.

Kjonigsen, L.J., Lillehaug, S., Bjaalie, J.G., Witter, M.P. & Leergard, T.B., 2015. Waxholm Space atlas of the rat brain hippocampal region: three-dimensional delineations based on magnetic resonance and diffusion tensor imaging. *NeuroImage*, 108, pp.441–449.

Klink, R. & Alonso, A., 1997. Morphological characteristics of layer II projection neurons in the rat medial entorhinal cortex. *Hippocampus*, 7(5), pp.571–583.

Knierim, J.J., Neunuebel, J.P. & Deshmukh, S.S., 2014. Functional correlates of the lateral and medial entorhinal cortex: objects, path integration and local-global reference frames. *Philosophical Transactions of the Royal Society of London. Series B, Biological Sciences*, 369(1635).

Korogod, N., Petersen, C.C.H. & Knott, G.W., 2015. Ultrastructural analysis of adult mouse neocortex comparing aldehyde perfusion with cryo fixation. *eLife*, 4.

Kropff, E., Carmichael, J.E., Moser, M-B. & Moser, E.I., 2015. Speed cells in the medial entorhinal cortex. *Nature*, 523(7561), pp.419–424.

Langston, R.F., Ainge, J.A., Couey, J.J., Canto, C.B., Bjerknes, T.L., Witter, M.P., Moser, E.I. & Moser, M-B., 2010. Development of the spatial representation system in the rat. *Science*, 328(5985), pp.1576–1580.

Li, J., Erisir, A. & Cline, H., 2011. In vivo time-lapse imaging and serial section electron microscopy reveal developmental synaptic rearrangements. *Neuron*, 69(2), pp.273–286.

Lichtman, J.W. & Colman, H., 2000. Synapse elimination and indelible memory. *Neuron*,

25(2), pp.269–278.

McCormick, D.A., Connors, B.W., Lighthall, J.W. & Prince, D.A., 1985. Comparative electrophysiology of pyramidal and sparsely spiny stellate neurons of the neocortex. *Journal of Neurophysiology*, 54(4), pp.782–806.

Miettinen, M., Koivisto, E., Riekkinen, P. & Miettinen, R., 1996. Coexistence of parvalbumin and GABA in nonpyramidal neurons of the rat entorhinal cortex. *Brain Research*, 706(1), pp.113–122.

Miller, M., 1981. Maturation of rat visual cortex. I. A quantitative study of Golgi-impregnated pyramidal neurons. *Journal of Neurocytology*, 10(5), pp.859–878.

Miller, M. & Peters, A., 1981. Maturation of rat visual cortex. II. A combined Golgi-electron microscope study of pyramidal neurons. *The Journal of Comparative Neurology*, 203(4), pp.555–573.

Moser, E., Witter, M. & Moser, M.-B., 2010. Entorhinal cortex. In G. Shepherd & S. Grillner, eds. *Handbook of Brain Microcircuits*. Oxford: Oxford University Press, pp. 175–192.

Moser, E.I., Roudi, Y., Witter, M.P., Kentros, C., Bonhoeffer, T. & Moser, M-B., 2014. Grid cells and cortical representation. *Nature Reviews Neuroscience*, 15(7), pp.466–481.

Moser, E.I., Kropff, E. & Moser, M.-B., 2008. Place cells, grid cells, and the brain's spatial representation system. *Annual Review of Neuroscience*, 31, pp.69–89.

Muller, R.U. & Kubie, J.L., 1987. The effects of changes in the environment on the spatial firing of hippocampal complex-spike cells. *The Journal of Neuroscience*, 7(7), pp.1951–1968.

O'Keefe, J. & Dostrovsky, J., 1971. The hippocampus as a spatial map. Preliminary evidence from unit activity in the freely-moving rat. *Brain Research*, 34(1), pp.171–175.

Papp, E.A., Leergard, T., Calabrese, E., Johnson, G.A. & Bjaalie, J.G., 2014. Waxholm Space atlas of the Sprague Dawley rat brain. *NeuroImage*, 97, pp.374–386.

Parnavelas, J.G. & Lieberman, A.R., 1979. An ultrastructural study of the maturation of neuronal somata in the visual cortex of the rat. *Anatomy and Embryology*, 157(3), pp.311–328.

Paulsen, A., 2016. *Postnatal development of parvalbumin-immunoreactive cells in the medial entorhinal cortex of the rat: Morphology, connectivity and ultrastructure*. Master thesis. Norwegian Institute of Science and Technology.

Pawelzik, H., Hughes, D.I. & Thomson, A.M., 2002. Physiological and morphological diversity of immunocytochemically defined parvalbumin- and cholecystokinin-positive interneurones in CA1 of the adult rat hippocampus. *Journal of Comparative Neurology*, 443(4), pp.346–367.

Portera-Cailliau, C., Weimer, R.M., De Paola, V., Caroni, P. & Svoboda, K., 2005. Diverse

modes of axon elaboration in the developing neocortex. *PLoS biology*, 3(8), pp.1473–1487.

Queisser, G., Wiegert, S. & Bading, H., 2011. Structural dynamics of the cell nucleus: basis for morphology modulation of nuclear calcium signaling and gene transcription. *Nucleus*, 2(2), pp.98–104.

Ray, S. & Brecht, M., 2016. Structural development and dorsoventral maturation of the medial entorhinal cortex. *eLife*, 5(e13343).

del Río, J.A., de Lecea, L., Ferrer, I. & Soriano, E., 1994. The development of parvalbumin-immunoreactivity in the neocortex of the mouse. *Developmental Brain Research*, 81(2), pp.247–259.

Rivera, C., Voipio, J., Payne, J.A., Ruusuvuori, E., Lahtinen, H., Lamsa, K., Pirvola, U., Saarma, M. & Kaila, K., 1999. The K+/Cl- co-transporter KCC2 renders GABA hyperpolarizing during neuronal maturation. *Nature*, 397(6716), pp.251–255.

Rivera, C., Voipio, J. & Kaila, K., 2005. Two developmental switches in GABAergic signalling: the K+-Cl- cotransporter KCC2 and carbonic anhydrase CAVII. *The Journal of Physiology*, 562(1), pp.27–36.

Rudy, J.W., Stadler-Morris, S. & Albert, P., 1987. Ontogeny of spatial navigation behaviors in the rat: dissociation of "proximal"- and "distal"-cue-based behaviors. *Behavioral Neuroscience*, 101(1), pp.62–73.

Sargolini, F., Fyhn, M., Hafting, T., McNaughton, B.L., Witter, M.P., Moser, M-B. & Moser, E-I., 2006. Conjunctive representation of position, direction, and velocity in entorhinal cortex. *Science*, 312(5774), pp.758–762.

Schenk, F., 1985. Development of place navigation in rats from weaning to puberty. *Behavioral and Neural Biology*, 43(1), pp.69–85.

Seress, L. & Ribak, C.E., 1990. Postnatal development of the light and electron microscopic features of basket cells in the hippocampal dentate gyrus of the rat. *Anatomy and Embryology*, 181(6), pp.547–565.

Seress, L. & Ribak, C.E., 1992. Ultrastructural features of primate granule cell bodies show important differences from those of rats: axosomatic synapses, somatic spines and infolded nuclei. *Brain Research*, 569(2), pp.353–357.

Sohal, V.S., Zhang, F., Yizar, O. & Deisseroth, K., 2009. Parvalbumin neurons and gamma rhythms enhance cortical circuit performance. *Nature*, 459(7247), pp.698–702.

Solbach, S. & Celio, M.R., 1991. Ontogeny of the calcium binding protein parvalbumin in the rat nervous system. *Anatomy and Embryology*, 184(2), pp.103–124.

Solstad, T., Boccara, C.N., Kropff, E., Moser, M-B. & Moser, E.I., 2008. Representation of geometric borders in the entorhinal cortex. *Science*, 322(5909), pp.1865–1868.

Soriano, E., del Rio, J.A., Ferrer, I., Auladell, C., de Lecea, L. & Alcantara, S., 1992. Late appearance of parvalbumin-immunoreactive neurons in the rodent cerebral cortex does not follow an “inside-out” sequence. *Neuroscience Letters*, 142(2), pp.147–150.

Soriano, E., Cobas, A. & Fairén, A., 1986. Asynchronism in the neurogenesis of GABAergic and non-GABAergic neurons in the mouse hippocampus. *Developmental Brain Research*, 30(1), pp.88–92.

Stensola, H., Stensola, T., Solstad, T., Frøland, K., Moser, M-B. & Moser, E.I., 2012. The entorhinal grid map is discretized. *Nature*, 492(7427), pp.72–8.

Strange, B.A., Witter, M.P., Lein, E.S. & Moser, E-I, 2014. Functional organization of the hippocampal longitudinal axis. *Nature Reviews Neuroscience*, 15(10), pp.655–669.

Takahashi, T., Nowakowski, R. & Caviness, VS, J., 1995. The cell cycle of the pseudostratified ventricular epithelium of the embryonic murine cerebral wall. *The Journal of Neuroscience*, 15(9), pp.6046–6057.

Takahashi-Iwanaga, H., 1992. Reticular endings of Purkinje cell axons in the rat cerebellar nuclei: scanning electron microscopic observation of the pericellular plexus of Cajal. *Archives of Histology and Cytology*, 55(3), pp.307–314.

Tang, Q., Burgalossi, A., Ebbesen, C.L., Ray, S., Naumann, R., Schmidt, H., Spicher, D. & Brecht, M., 2014. Pyramidal and stellate cell specificity of grid and border representations in layer 2 of medial entorhinal cortex. *Neuron*, 84(6), pp.1191–1197.

Taube, J.S., 2007. The Head Direction Signal: Origins and Sensory-Motor Integration. *Annual Review of Neuroscience*, 30(1), pp.181–207.

Taube, J.S., Muller, R.U. & Ranck, J.B., 1990. Head-direction cells recorded from the postsubiculum in freely moving rats. I. Description and quantitative analysis. *The Journal of Neuroscience*, 10(2), pp.420–435.

Tsao, A., Moser, M.-B. & Moser, E.I., 2013. Traces of Experience in the Lateral Entorhinal Cortex. *Current Biology*, 23(5), pp.399–405.

Tyzio, R., Represa, A., Jorquera, I., Ben-Ari, Y., Gozlan, H. & Aniksztejn, L., 1999. The establishment of GABAergic and glutamatergic synapses on CA1 pyramidal neurons is sequential and correlates with the development of the apical dendrite. *The Journal of Neuroscience*, 19(23), pp.10372–10382.

Varga, C., Lee, S.Y. & Soltesz, I., 2010. Target-selective GABAergic control of entorhinal cortex output. *Nature Neuroscience*, 13(7), pp.822–824.

Walsh, M.K. & Lichtman, J.W., 2003. In Vivo Time-Lapse Imaging of Synaptic Takeover Associated with Naturally Occurring Synapse Elimination. *Neuron*, 37(1), pp.67–73.

Wills, T.J., Cacucci, F., Burgess, N. & O'Keefe, J., 2010. Development of the hippocampal cognitive map in preweanling rats. *Science*, 328(5985), pp.1573–1576.

Wills, T.J., Muessig, L. & Cacucci, F., 2014. The development of spatial behaviour and the hippocampal neural representation of space. *Philosophical Transactions of the Royal Society of London. Series B, Biological Sciences*, 369.

Witte, S., Stier, H. & Cline, H.T., 1996. In vivo observations of timecourse and distribution of morphological dynamics in Xenopus retinotectal axon arbors. *Journal of Neurobiology*, 31(2), pp.219–234.

Witter, M.P., Canto, C.B., Couey, J.J., Koganezawa, N. & O'Reilly, K.C., 2014. Architecture of spatial circuits in the hippocampal region. *Philosophical Transactions of the Royal Society of London. Series B, Biological Sciences*, 369(1635).

Witter, M.P., Naber, P.A., van Haeften, T., Machielsen, W.C., Rombouts, S.A., Barkhof, F., Scheltens, P. & Lopes da Silva, F.H., 2000. Cortico-hippocampal communication by way of parallel parahippocampal-subicular pathways. *Hippocampus*, 10(4), pp.398–410.

Wittmann, M., Queisser, G., Eder, A., Wiegert, J.S., Bengtson, C.P., Hellwig, A., Wittum, G. & Bading, H., 2009. Synaptic activity induces dramatic changes in the geometry of the cell nucleus: interplay between nuclear structure, histone H3 phosphorylation, and nuclear calcium signaling. *The Journal of Neuroscience*, 29(47), pp.14687–14700.

Wouterlood, F.G., Härtig, W., Brückner, G. & Witter, M.P., 1995. Parvalbumin-immunoreactive neurons in the entorhinal cortex of the rat: localization, morphology, connectivity and ultrastructure. *Journal of Neurocytology*, 24(2), pp.135–153.

Zecevic, N., Bourgeois, J.P. & Rakic, P., 1989. Changes in synaptic density in motor cortex of rhesus monkey during fetal and postnatal life. *Developmental Brain Research*, 50(1), pp.11–32.

Appendix I: Additional images from electron microscopy

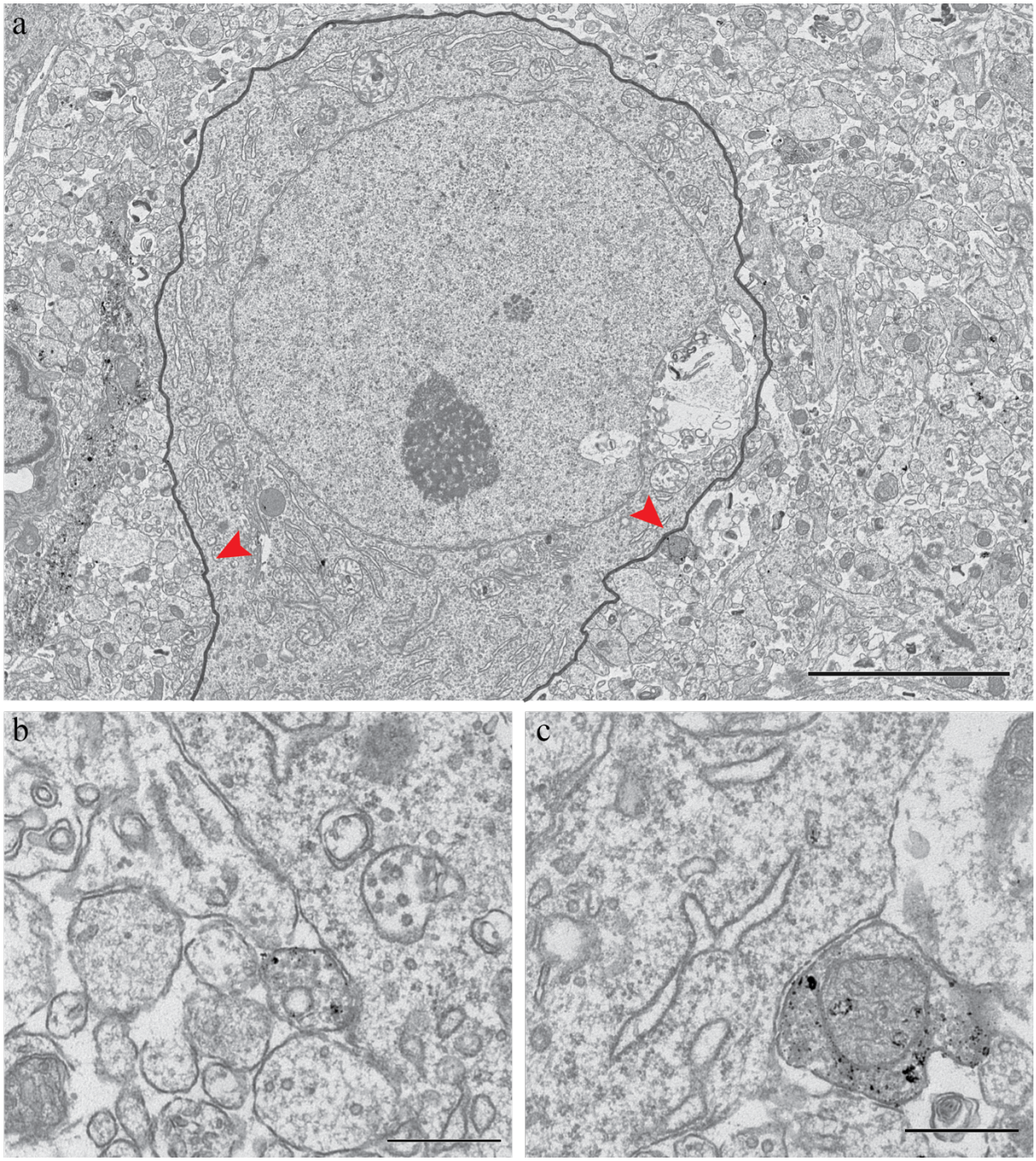

Figure A1. A cell body receiving PV+ input at P10. The dark line in **a)** indicates the cell membrane. The cell body is round, with a large dendrite extending. The nucleus is also round and it displays a dark nucleolus. Two PV+ terminals can be seen apposing the soma of this cell, indicated by red arrows in **a)** and depicted at higher magnification in **b)** and **c)**. Scale bars are **a)** 5 μm and **b-c)** 500 nm.

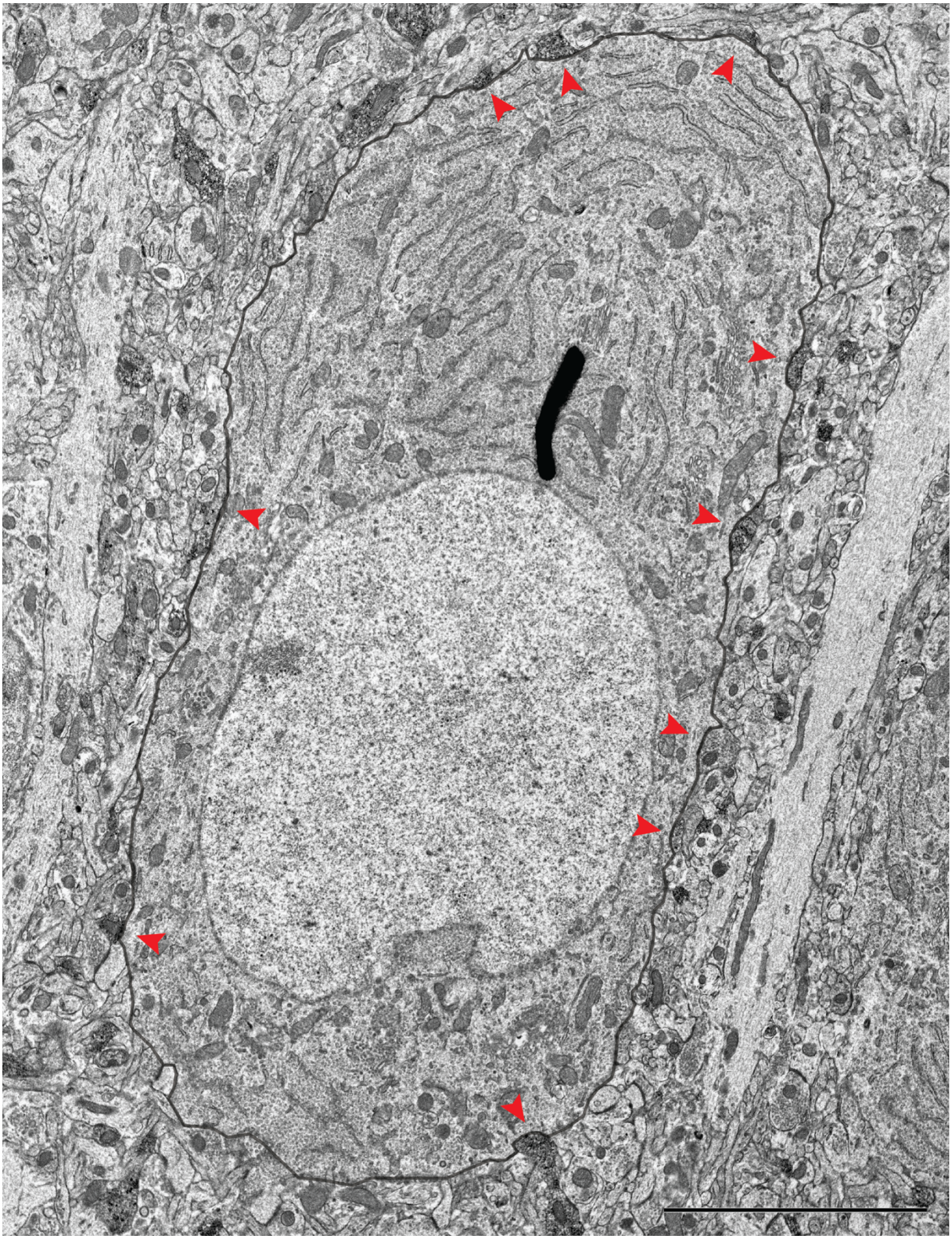

Figure A2. A cell body receiving PV+ input at P15. The dark line indicates the cell membrane. This cell body has an elongated shape and a round nucleus with a small indentation. Ten PV+ terminals can be seen apposing the cell body, indicated by red arrows. Individual boutons at higher magnification are shown in Figure A3. Scale bar: 5 μm.

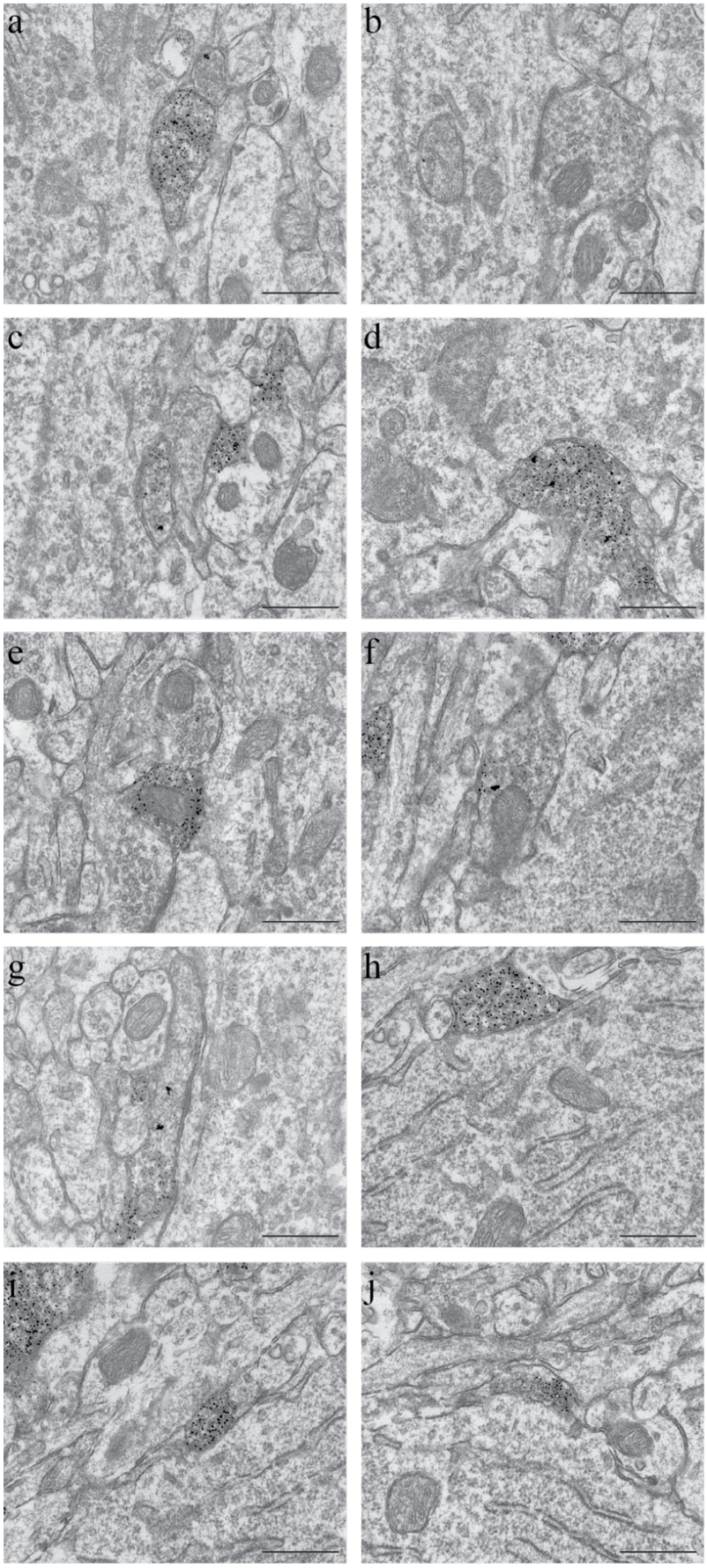

Figure A3. PV+ boutons targeting a cell body at P15. The cell body is depicted in Figure A2. The bouton seen in **b)** is very lightly stained, but the presence of labelling could be confirmed at higher magnification. Scale bars are 500 nm.

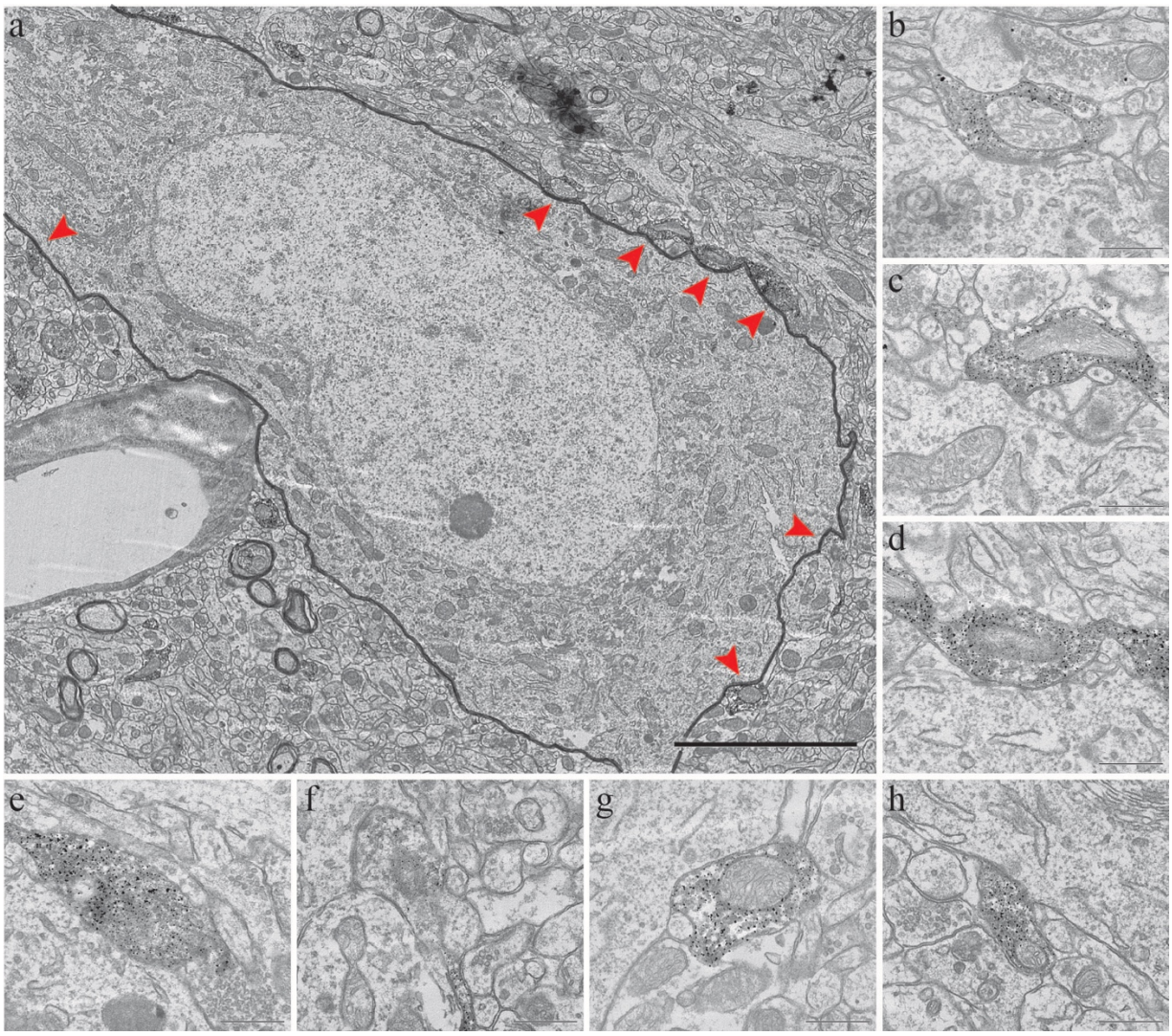

Figure A4. A cell body receiving PV+ input at P30. This cell body is triangular with a large dendrite extending, thus classified here as pyramidal. The nucleus is ovoidal with a small indentation and a small nucleolus. The dark line in **a)** indicates the cell membrane. Seven PV+ terminals can be seen around this cell body, indicated in **a)** by red arrows, and depicted at higher magnification in **b)-h)**. Three of the terminals, those in **c)-e)**, are linked by PV+ axonal bridges. Scale bars are **a)** 5 μm and **b-h)** 500 nm.

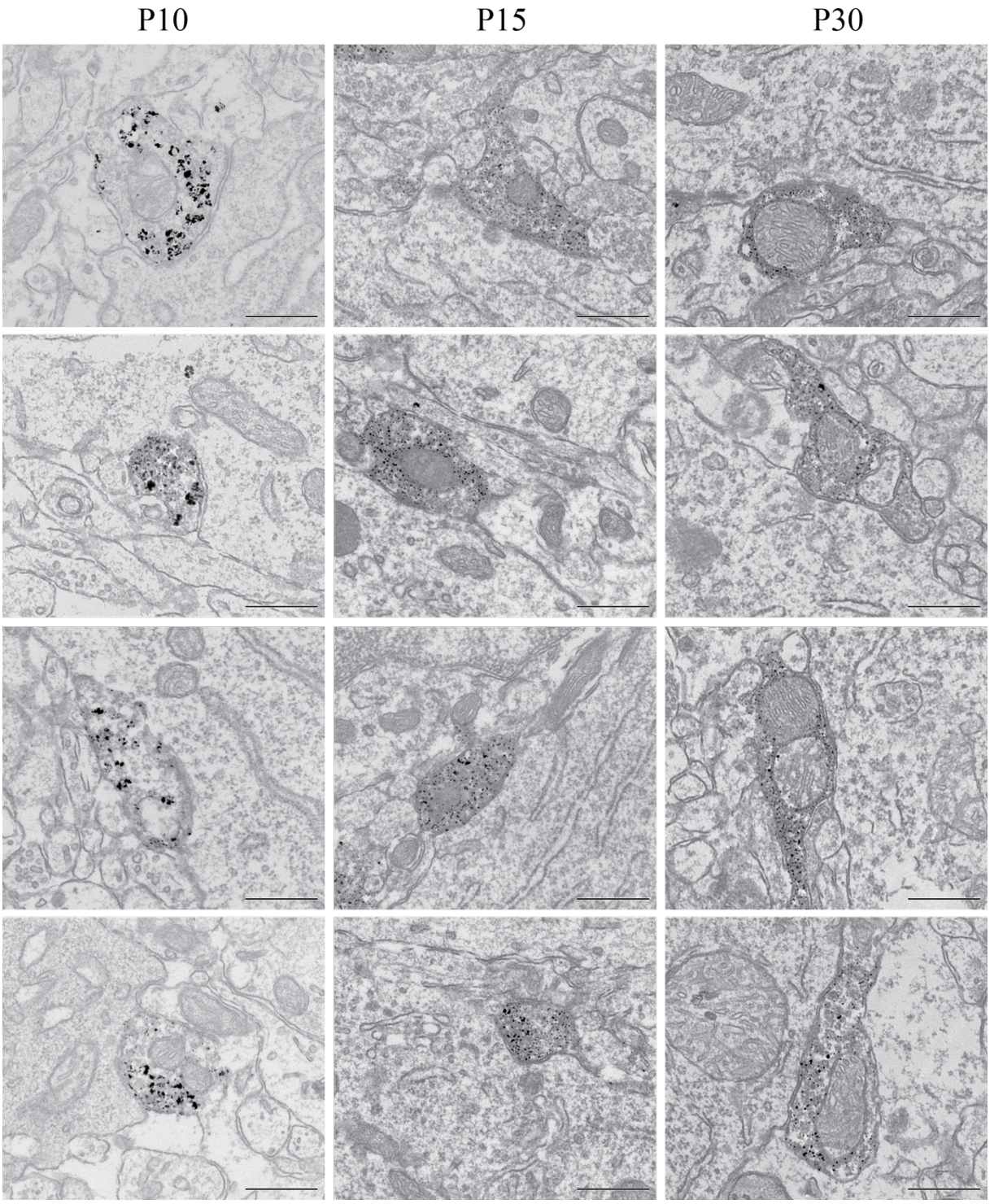

Figure A5. PV+ somatic terminals from different age groups.

Appendix II: Figures from immunohistochemical tests

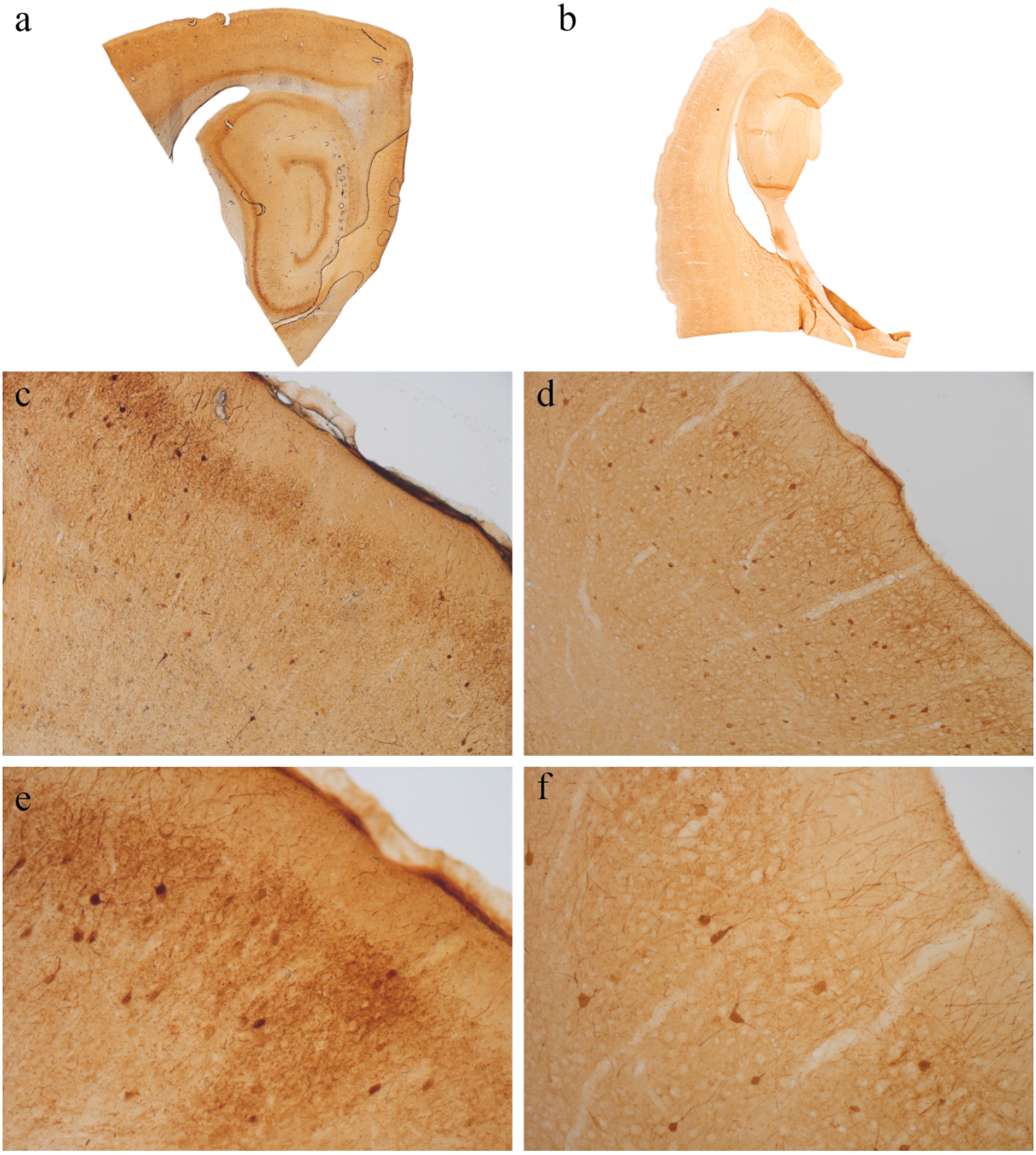

Figure A6. Light micrographs showing results from using the normal protocol for immunohistochemistry for EM (***a, c, e***), detailed in appendix IVc, versus results from using a fluorescence protocol from the Kavli Institute adapted to DAB (***b, d, f***), detailed in appendix IVb. Images are obtained with an objective of **a-b)** 5X, **c-d)** 10X, and **e-f)** 20X. Although both protocols gave strong and specific labelling, the Kavli protocol proved superior in that it gave better visualization of dendritic and axonal processes.

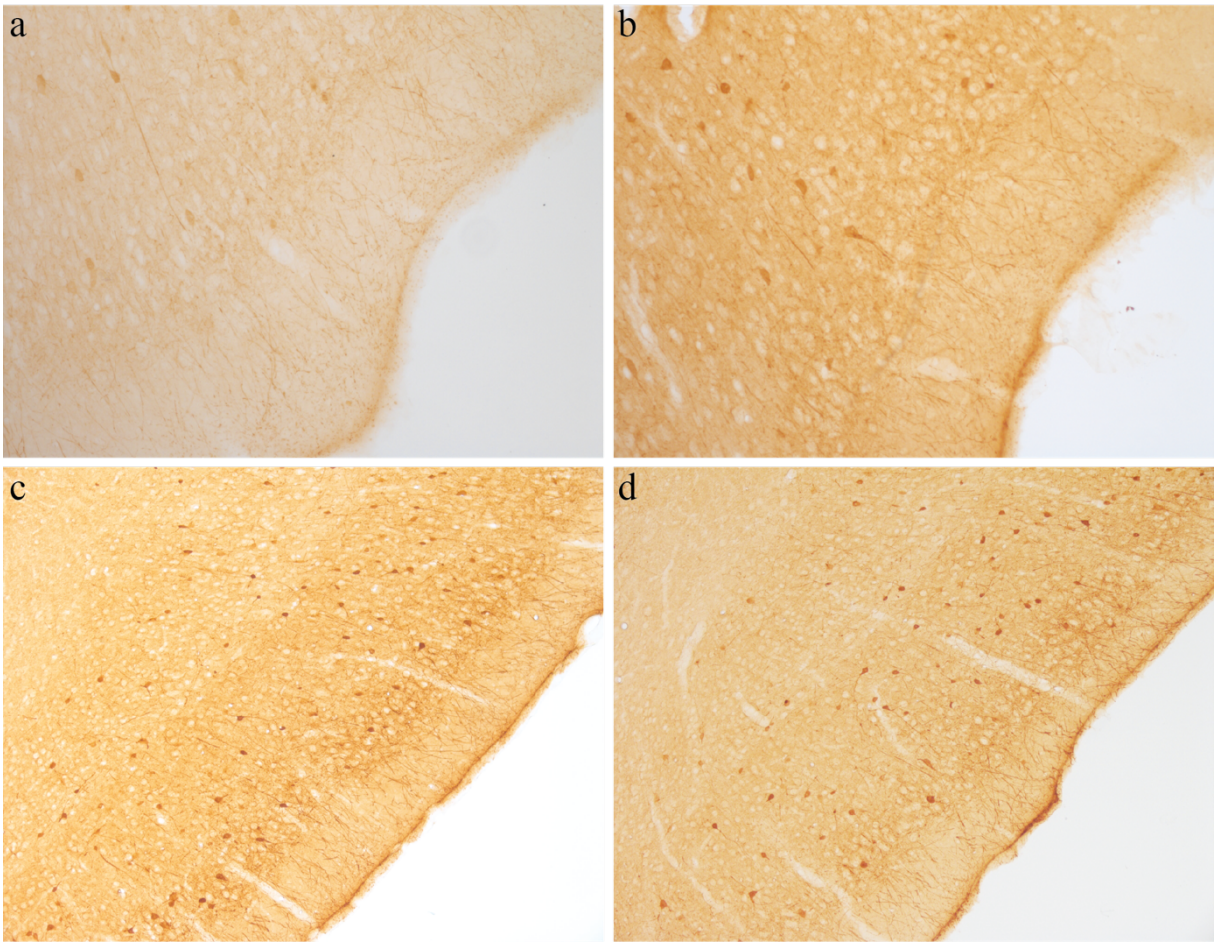

Figure A7. Light micrographs showing results from testing for immunohistochemistry for LM. The images display sections that have been treated with the following antibody concentrations and DAB reaction times:
a) 1:20 000, 1 minute of DAB reaction;
b) 1:20 000, 4 minutes DAB reaction;
c) 1:20 000, 8 minutes DAB reaction; and
d) 1:40 000, 4 minutes DAB reaction.
The rest of the protocol was the one given in appendix IVb. Images are obtained with a 20X objective.

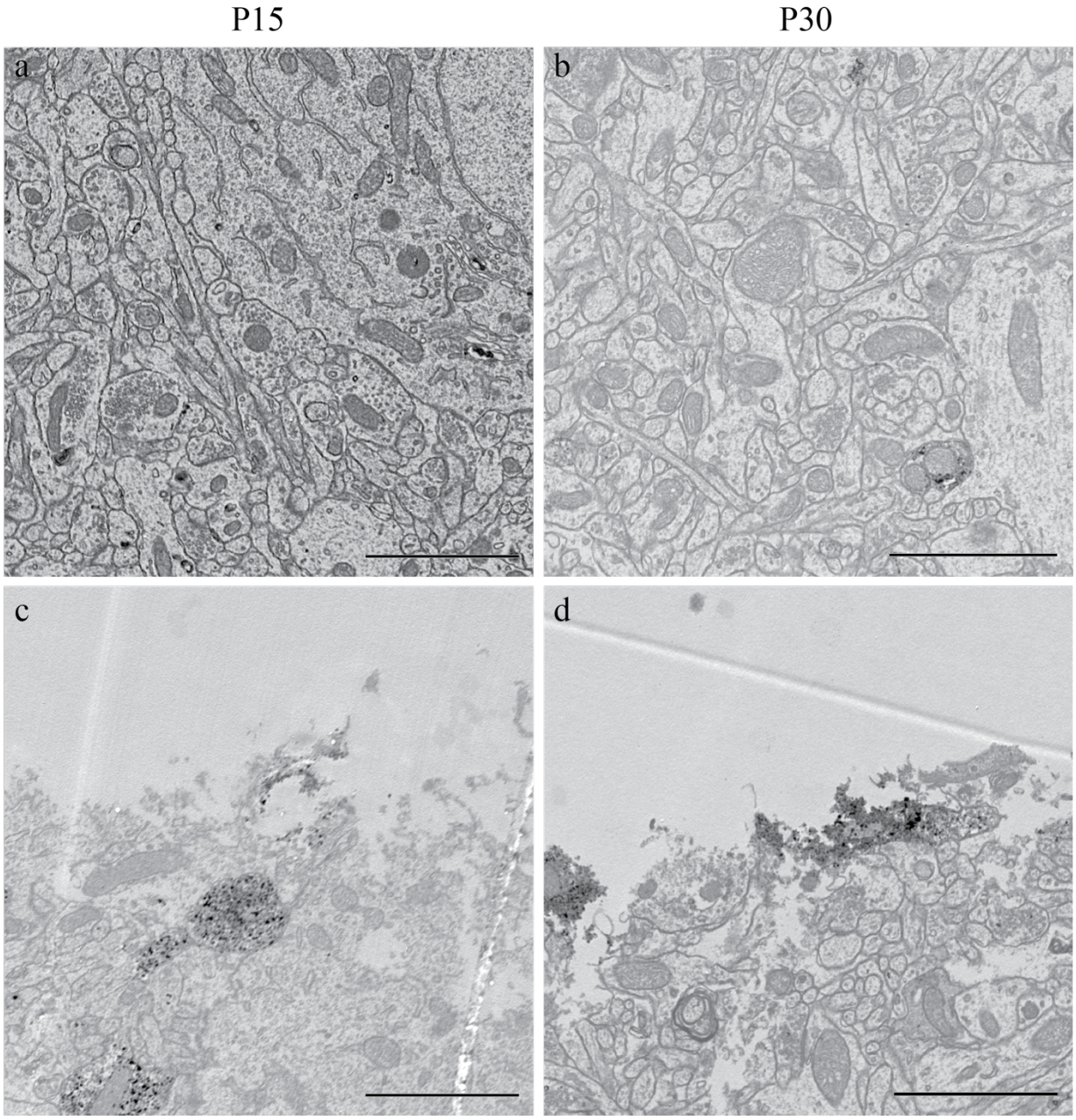

Figure A8. Testing of a protocol with very little TrX for P15 and P30. In this protocol, 0.05% TrX was only used for a single permeabilization step of 20 minutes. The morphology was good, but staining was almost exclusively present at the surface of the tissue, illustrated by images **c)** and **d)**. Scale bars are 2 μm.

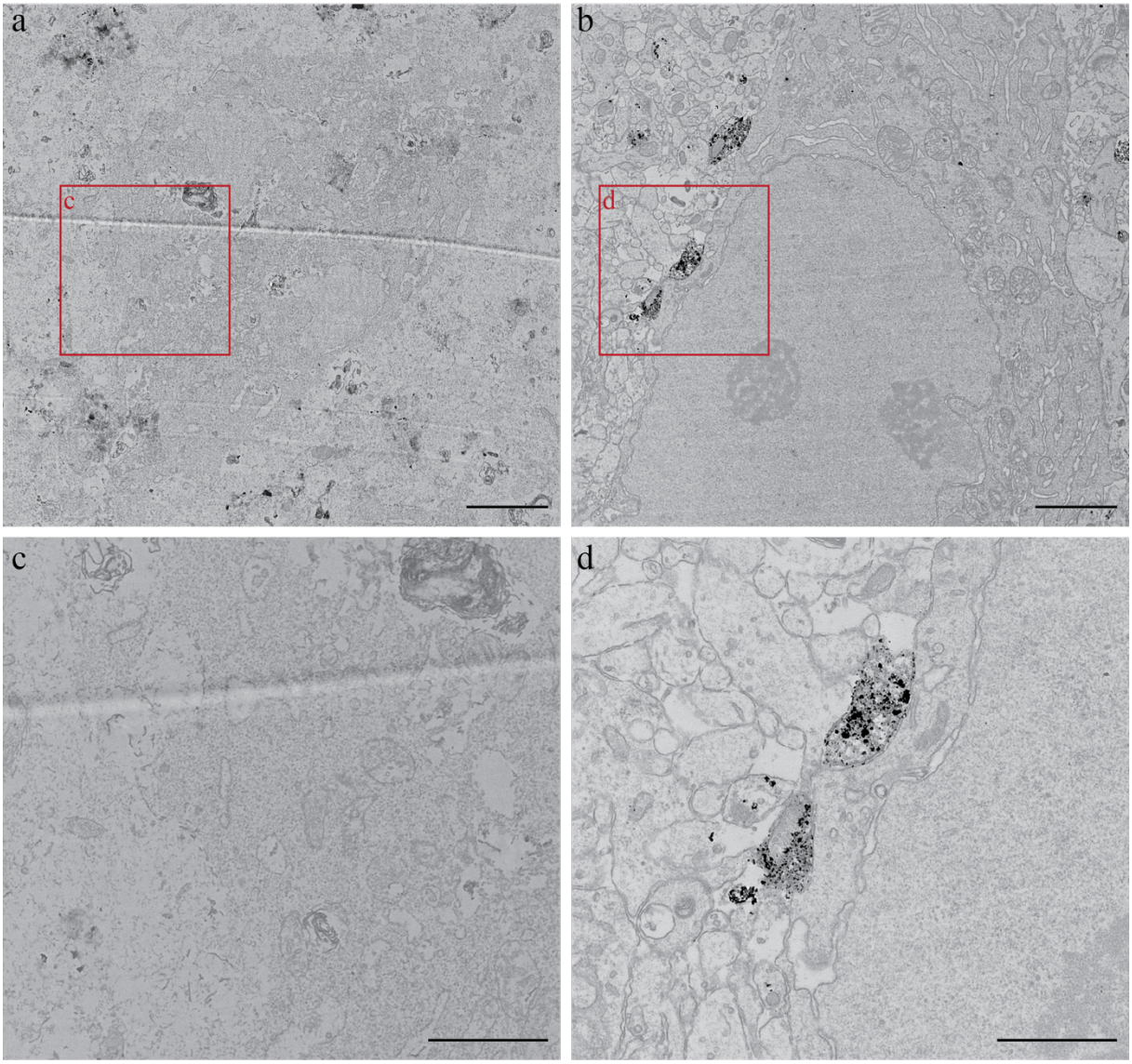

Figure A9. First and final protocols used for EM at P10. Images **a)** and **c)** depict results from the first protocol that was tested (found in appendix IVd). The tissue has been severely damaged by this treatment and hence the morphology does not allow for visualization of any details. As such, it was not really possible to evaluate the amount or quality of labelling in these sections. Images **b)** and **d)** show results from the final protocol used for P10, details of which can be found in appendix IVe. This material was insufficiently rinsed between incubation in ABC and DAB, which probably caused the slight amount of gold deposits. However, the treatment gave acceptable morphology, as well as strong labelling. Scale bars are 2 μm in **a)** and **b)**, and 1 μm in **c)** and **d)**.

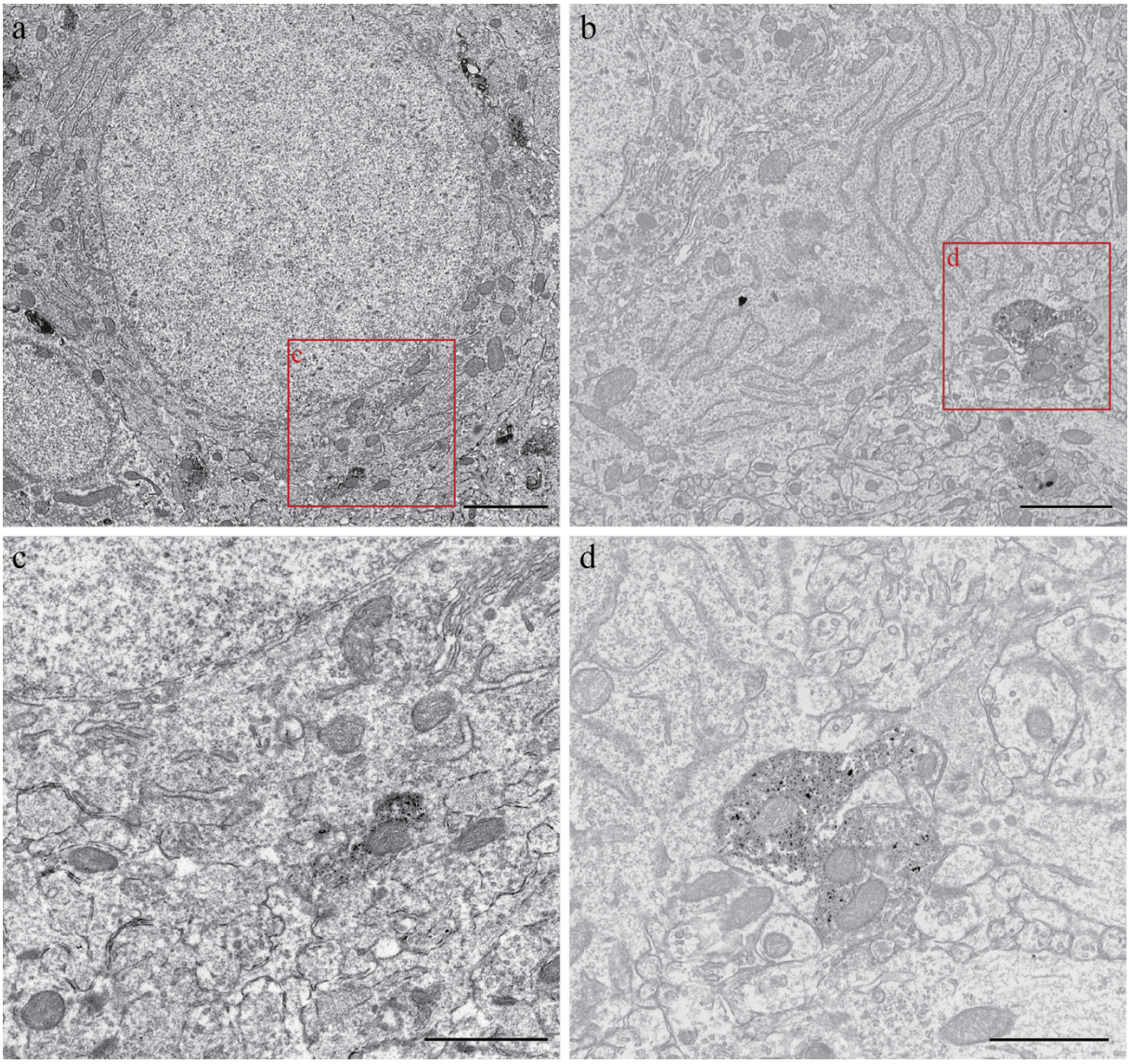

Figure A10. First and final protocols used for EM at P15. Images **a)** and **c)** depict results from the first protocol that was tested, given in appendix IVd. Staining is strong and specific, but the morphology, especially the visualization of membranes, is very poor. The staining is so intense that vesicles inside terminal boutons cannot be seen. Images **b)** and **d)** show results from the final protocol used for P30, detailed in appendix IVe. Staining is strong and specific, but less dense than in the other protocol, and the morphology is considerably better. Scale bars are 2 μm in **a)** and **b)**, and 1 μm in **c)** and **d)**.

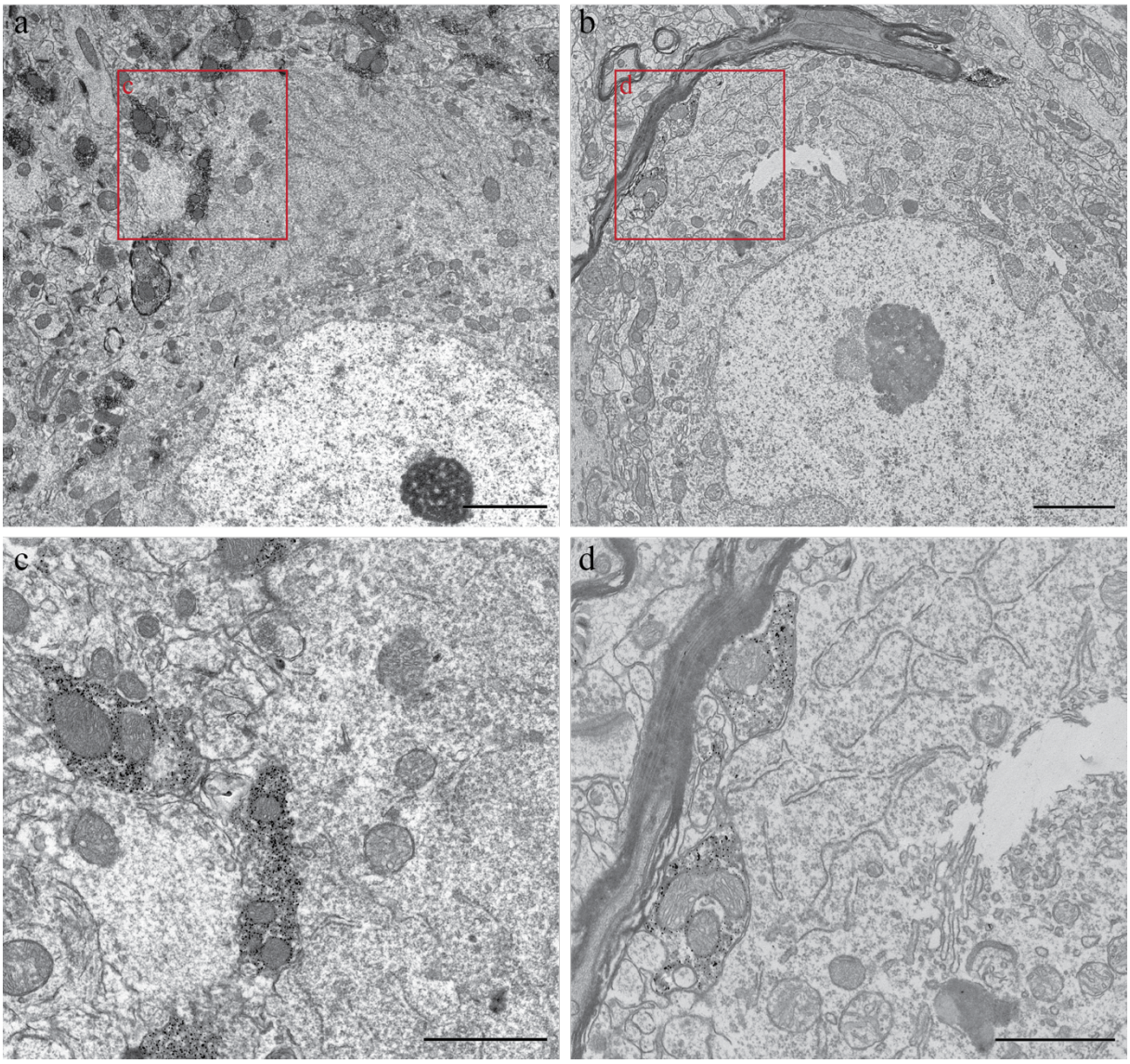

Figure A11. First and final protocols used for EM at P30. Images **a)** and **c)** depict results from the protocol given in appendix IVd. As was the case for the material from P15 using this protocol (Figure A10), there is strong and specific labelling but poor morphology. Images **b)** and **d)** show results from the final protocol used for P15, detailed in appendix IVe. The results from using this protocol resembles that for material from P15, possibly with slightly better morphology. Scale bars are 2 μm in **a)** and **b)**, and 1 μm in **c)** and **d)**.

Appendix III: Results from statistical analyses

In the following tables, 'nr of boutons' refers to the number of PV+ boutons apposing the soma, and 'bouton density' refers to the number of PV+ boutons per μm membrane.

Table A1. Descriptive statistics and confidence intervals for soma variables from the different age groups

					95% CI for mean		Range	
		N	*M*	*SD*	Lower	Upper	Min.	Max
Soma mean axis	P10	78	15.24	3.27	14.50	15.98	7.81	22.59
	P15	80	17.32	4.02	16.43	18.21	9.30	26.28
	P20	80	16.84	3.50	16.07	17.62	9.04	24.60
Nucleus mean axis	P10	77	8.94	2.21	8.44	9.45	3.97	13.32
	P15	80	10.28	3.04	9.60	10.96	2.60	15.07
	P30	76	10.49	2.44	9.93	11.05	3.29	14.13
Soma perimeter	P10	75	58.88	13.53	55.76	61.99	32.19	91.70
	P15	80	64.47	15.07	61.11	67.83	34.51	100.0
	P30	79	61.48	12.80	58.61	64.34	32.36	91.41
Nr of boutons	P10	80	2.44	1.47	2.11	2.76	1.00	6.00
	P15	80	6.78	3.32	6.04	7.51	2.00	16.00
	P30	80	5.38	2.84	4.74	6.01	2.00	15.00
Bouton density	P10	75	0.04	0.02	0.04	0.05	0.01	0.10
	P15	80	0.11	0.05	0.10	0.12	0.03	0.24
	P30	79	0.09	0.04	0.08	0.10	0.02	0.18

Table A2. Levene's test of homogeneity of variances between age groups for soma variables

	Levene statistic	df1	df2	*sig.*
Soma mean axis	2.48	2	235	.086
Nucleus mean axis	2.53	2	230	.082
Soma perimeter	1.39	2	231	.251
Nr of boutons	19.55	2	237	<.001*
Bouton density	9.64	2	231	<.001*

Asterisks indicate significant differences.

Table A3. Descriptive statistics and confidence intervals for bouton variables from the different age groups

					95% CI for mean		Range	
		N	*M*	*SD*	Lower	Upper	Min.	Max
Nr of mitochondria	P10	195	0.35	0.57	0.27	0.43	0.00	2.00
	P15	542	0.44	0.65	0.38	0.49	0.00	6.00
	P30	430	0.76	0.74	0.69	0.83	0.00	4.00
Bouton area	P10	188	0.53	0.41	0.47	0.59	0.05	2.99
	P15	526	0.36	0.27	0.34	0.38	0.04	2.11
	P30	427	0.48	0.28	0.46	0.51	0.04	1.69
Aspect ratio	P10	190	1.71	0.69	1.61	1.81	1.00	5.69
	P15	527	2.29	1.06	2.20	2.38	1.00	8.91
	P30	427	2.33	1.02	2.23	2.42	1.00	6.73
Short axis	P10	190	0.61	0.23	0.58	0.64	0.20	1.73
	P15	527	0.45	0.18	0.44	0.47	0.16	1.09
	P30	427	0.55	0.21	0.53	0.57	0.13	1.33
Long axis	P10	190	1.01	0.47	0.94	1.08	0.26	2.54
	P15	527	0.98	0.50	0.94	1.03	0.30	3.47
	P30	427	1.11	0.40	1.11	1.12	0.28	2.62

Table A4. Levene's test of homogeneity of variances between age groups for bouton variables

	Levene statistic	df1	df2	sig.
Nr of mitochondria	6.22	2	1164	.002*
Bouton area	15.55	2	1138	<.001*
Aspect ratio	13.30	2	1141	<.001*
Short axis	8.87	2	1141	<.001*
Long axis	4.55	2	1141	.011*

Asterisks indicate significant differences.

TABLE A5. Post hoc analysis comparing soma variables at different ages

			Mean difference	*SE*	*p*	*d*
Soma mean axis	P10	P15	–2.08	0.58	.001*	0.57
	P15	P30	0.48	0.60	.700	0.13
	P30	P10	1.60	0.54	.010*	0.47
Nucleus mean axis	P10	P15	–1.34	0.42	.005*	0.50
	P15	P30	–0.21	0.44	.879	0.08
	P30	P10	1.55	0.38	<.001*	0.67
Soma perimeter	P10	P15	–5.59	2.30	.042*	0.39
	P15	P30	3.00	2.21	.369	0.21
	P30	P10	2.60	2.12	.442	0.20
Nr of boutons	P10	P15	–4.34	0.41	<.001*	1.69
	P15	P30	1.40	0.49	.013*	0.45
	P30	P10	2.94	0.36	<.001*	1.30
Bouton density	P10	P15	–0.06	0.01	<.001*	1.72
	P15	P30	0.02	0.01	.036*	0.40
	P30	P10	0.05	0.01	<.001*	1.38

Results from multiple comparisons of somatic measurements at different ages, using a Games-Howell post hoc analysis. Asterisks indicate significant differences.

TABLE A6. Post hoc analysis comparing bouton variables at different ages

			Mean difference	*SE*	*p*	*d*
Nr of mitochondria	P10	P15	–0.09	0.05	.183	0.15
	P15	P30	–0.32	0.05	<.001*	0.46
	P30	P10	0.41	0.05	<.001*	0.62
Bouton area	P10	P15	0.17	0.03	<.001*	0.49
	P15	P30	–0.12	0.02	<.001*	0.44
	P30	P10	–0.05	0.03	.287	0.14
Aspect ratio	P10	P15	–0.58	0.07	<.001*	0.65
	P15	P30	0.03	0.07	.868	0.03
	P30	P10	0.62	0.07	<.001*	0.71
Short axis	P10	P15	0.16	0.02	<.001*	0.76
	P15	P30	–0.10	0.01	<.001*	0.49
	P30	P10	–0.06	0.02	.005*	0.28
Long axis	P10	P15	0.03	0.04	.801	0.05
	P15	P30	–0.16	0.03	<.001*	0.36
	P30	P10	0.14	0.04	.001*	0.32

Results from multiple comparisons of bouton measurements across age groups, using a Games-Howell post hoc analysis. Asterisks indicate significant differences.

TABLE A7. Independent t-test comparing features of somata from P30 animals

	Animal					
	P30-4	**P30-6**	***t***	**df**	***p* (2-tailed)**	***d***
Soma variables						
Soma mean axis	15.71 ± 0.48	18.22 ± 0.57	–3.40	78	.001*	0.77
Nucleus mean axis	9.65 ± 0.36	11.53 ± 0.38	–3.59	74	.001*	0.83
Soma perimeter	56.95 ± 1.79	66.87 ± 2.01	–3.70	77	<.001*	0.84
Nr of boutons	5.84 ± 0.47	4.81 ± 0.40	1.64	78	.105	0.37
Bouton density	0.10 ± 0.01	0.07 ± 0.01	3.64	78	<.001*	0.82
Bouton variables						
Bouton area	0.44 ± 0.02	0.54 ± 0.02	–3.95	425	<.001*	0.36
Bouton aspect ratio	2.28 ± 0.06	2.40 ± 0.08	–1.19	425	.234	0.12
Nr of mitochondria	0.70 ± 0.04	0.83 ± 0.07	–1.76	306	.095	0.17

Group means together with their standard error are presented for each variable for each of the animals. Asterisks indicate significant differences.

TABLE A8. Independent t-test comparing features of somata from P10 animals

	Animal					
	P10-3	**P10-4**	***t***	**df**	***p* (2-tailed)**	***d***
Soma variables						
Soma mean axis	15.10 ± 0.61	15.32 ± 0.47	–0.29	76	.770	0.07
Nucleus mean axis	9.11 ± 0.48	8.85 ± 0.29	0.49	75	.623	0.11
Soma perimeter	56.98 ± 2.44	60.07 ± 2.03	–0.96	73	.339	0.23
Nr of boutons	2.47 ± 0.21	2.42 ± 0.23	0.14	78	.891	0.04
Bouton density	0.05 ± 0.004	0.04 ± 0.004	0.66	73	.512	0.39
Bouton variables						
Bouton area	0.53 ± 0.04	0.53 ± 0.04	–0.14	186	.888	0.02
Bouton aspect ratio	1.60 ± 0.06	1.78 ± 0.07	–1.97	188	.050*	0.27
Nr of mitochondria	0.35 ± 0.06	0.35 ± 0.05	0.03	193	.979	0.00

Group means together with their standard error are presented for each variable for each of the animals. Asterisks indicate significant differences.

Appendix IV: Detailed protocols

Abbreviations used in following protocols:

BSA	Bovine serum albumin
DAB	3,3-diaminobenzidine
EM	Electron microscopy
H_2O_2	Hydrogen peroxide
LM	Light microscopy
MeOH	Methanol
MQ water	Milli-Q water
NGS/NHS	Normal goat/horse serum
P	Postnatal day
PB	Phosphate buffer
TBS	Tris buffered saline
TrX	Triton X-100

In the following protocols, all steps are performed at room temperature unless otherwise specified.

IVa Fluorescence protocol from the Kavli Institute

1. Rinsing: 0.125M PB, 3 x 15 min
2. Permeabilization: 0.125M PB + 1% TrX, 2 x 10 min
3. Pre-incubation: 0.125M PB + 1% TrX+ 5% NGS, 60 min
4. Incubation with primary antibody. Diluted 1:1000 in 0.125M PB + 1% TrX + 5% NGS, 24 hours at 4˚C
5. Rinsing: 0.125M PB, 4 x 15 min
6. Incubation with secondary antibody. Diluted 1:400 in 0.125M PB + 1% TrX, 24 hours at 4˚C
7. Rinsing: 0.125M PB, 4 x 15 min

IVb Adapted protocol used for LM

This is the protocol used for the final LM experiment, adapted to DAB from the Kavli fluorescence protocol (appendix IVa) and optimized through testing of different primary antibody concentrations and DAB reaction times (Figure A3).

Day 1

1. Rinsing: 0.1M PB (pH 7.4), 3 x 15 min
2. Permeabilization: 0.1M PB + 1% TrX (pH 7.4), 2 x 10 min
3. Blocking endogenous peroxidase activity: 1% H_2O_2 in 50% MeOH in PB, 30 min
4. Rinsing: 0.1M PB, 3 x 15 min
5. Pre-incubation: 0.1M PB + 1% TrX + 5% NHS (pH 7.4), 60 min
6. Incubation with primary antibody. Diluted 1:40 000 in 0.1M PB + 1% TrX + 5% NHS, overnight (approximately 24 hours) at 4˚C

Day 2

7. Rinsing: 0.1M PB, 4 x 15 min
8. Incubation with secondary antibody. Diluted 1:200 in 0.1M PB + 1% TrX, overnight at 4˚C

Day 3

9. Rinsing: 0.1M PB, 4 x 15 min
10. Incubation with ABC reagent: diluted in 0.1M PB, 1 hour
11. Rinsing: 0.1M PB, 4 x 15 min
12. DAB staining. Use 0.05% DAB and 0.01% H_2O_2 in 0.1M PB, 8 minutes in dark
13. Stopping reaction and rinsing: 0.1M PB, 3 x 10 min
14. Rinsing: MQ water, 2 x 10 min
15. Mounting on glass slides
16. Drying: Air dry or at 37˚C for 30 minutes
17. Coverslip: Add a drop of tissue mount to cover glass and coverslip sections. Let dry in a fume hood overnight before examining the sections in the microscope.

IVc Original protocol for immunohistochemistry for EM

This is the immunohistochemistry and embedding protocol that is used for EM in the lab.

Day 1

1. Rinsing: 0.1M TBS (pH 7.4), 3 x 10 min
2. Quenching of free aldehydes: 0.1% sodium borohydride, 30 min
3. Rinsing: 0.1M TBS, 3 x 10 min
4. Permeabilization: 0.1M TBS + 0.05% TrX (pH 7.4), 30 min
5. Rinsing: 0.1M TBS, 2 x 5 min
6. Blocking endogenous peroxidase: 1% H_2O_2 in 50% MeOH in 0.1M TBS, 30 min
7. Rinsing: 0.1M TBS, 3 x 10 min
8. Blocking step in incubation medium* with 10% NHS (pH 7.4), 2 hours
9. Incubation with primary antibody. Diluted (usually 1:20 000 for anti-PVG) in incubation medium with 1% NHS, overnight at 4˚C

Day 2

10. Rinsing: 0.1M TBS + 0.05% TrX, 3 x 10 min
11. Incubation with secondary antibody, diluted 1:200 in incubation medium, 2 hours
12. Rinsing: 0.1M TBS + 0.05% TrX, 3 x 10 min
13. Incubation with ABC reagent in 0.1M TBS (pH 7.6), 1 hour
14. Rinsing: 0.1M TBS + 0.05% TrX, 3 x 10 min
15. DAB staining: 0.05% DAB + 0.01% H_2O_2 in 0.1M TBS, 8 minutes in dark
16. Stopping reaction and rinsing: 0.1M TBS, 3 x 10 min**
17. Rinsing: Sørensen's 0.1M PB 3 x 10 min
18. Postfix in 2.5% glutaraldehyde in Sørensen's 0.1M PB: 1 hour
19. Rinsing: Sørensen's 0.1 M PB, 3 x 10 min
20. Inspect sections for labeling in LM (take pictures)
21. Rinsing: 2% sodium acetate (pH 8.7), 3 x 10 min. Use a new 24-well dish
22. Overnight at 4˚C in 10% sodium thioglycolate

Day 3

23. Rinsing: Fresh 2% sodium acetate (pH 8.7), 3 x 10 min
24. Physical development with a mixture of fresh developing solution***. Add 4 µL C to 1 mL B, then add B + C to 1 mL A. Develop for 8 minutes in dark

25. Stop development: 1% acetic acid, 2 min
26. Rinsing: 2% sodium acetate, 3 x 10 min
27. Incubation with 0.05% gold chloride, 15 min in dark
28. Rinsing: 2% sodium acetate, 3 x 10 min
29. 10 min in 3% sodium thiosulphate
30. Rinsing: 2% sodium acetate, 3 x 10 min
31. Rinsing: 0.1M cacodylate buffer, 2 x 10 min
32. Transfer the samples to dram glass before secondary fixation
33. Secondary fixation in 1% osmium tetroxide + 1.5% potassium ferrocyanide in 0.1 M cacodylate buffer, 15 min in dark
34. Rinsing: 0.1M cacodylate buffer, 2 x 10 min
35. 50% ethanol, 10 min
36. 70% ethanol, 10 min
37. 90% ethanol, 10 min
38. 100% ethanol, 4 x 15 min
39. Acetone: 2 x 15 min
40. Acetone + epoxy: 2+1, 2 hours
41. Acetone + epoxy 1+1, 2 hours
42. Acetone + epoxy: 1+2, overnight on rotator

Day 4

43. New epoxy: 8 hours, change once after 6 hours
44. Flat embedding overnight. Put the sections between two sheets of Aclar film and then between two microscope slides. Polymerize at 60˚C, 1 day

Day 5

45. Select area and glue onto epoxy resin block with a drop of fresh epoxy
46. Polymerize for 3-4 days at 60˚C

*The recipe for the incubation medium is given in appendix V

**This protocol, up until this point, was tested for LM (results of which are depicted in Figure A1). Mounting was done as described for the final LM protocol (appendix IVb).

***Information about the developing solution is given in appendix V

IVd Protocol based on LM protocol as tested for EM

This protocol was based on the new LM protocol (appendix IVc) with some changes, including antibody concentration and concentration and number of steps with TrX. We also added a rinsing step between permeabilization and peroxidase blocking, and used a lower DAB concentration. The latter change was due to a change in manufacturer. This protocol worked well for adult rats (P90+) and was thus the first protocol we tested for young (P10-P30) brains.

Day 1

1. Rinsing: 0.1M PB, 3 x 15 min
2. Permeabilization: 0.1M PB + 0.05% TrX, 20 min
3. Rinsing: 0.1M PB, 3 x 15 min
4. Blocking endogenous peroxidase activity: 1% H_2O_2 in 50% MeOH in 0.1M PB, 30 min
5. Rinsing: 0.1M PB, 3 x 15 min
6. Pre-incubation: 0.1M PB + 0.05% TrX + 5% NS, 60 min
7. Incubation with primary antibody. Diluted 1:20 000 in 0.1M PB + 0.05% TrX + 5% NHS, overnight (approximately 24 hours) at 4˚C

Day 2

8. Rinsing: 0.1M PB, 4 x 15 min
9. Incubation with secondary antibody. Diluted 1:400 with 0.1M PB, 2 hours
10. Rinsing: 0.1M PB, 4 x 15 min
11. Incubation with ABC reagent: diluted in 0.1M PB, 1 hour
12. Rinsing: 0.1M PB, 4 x 15 min
13. DAB staining: 0.03% DAB and 0.01 % H_2O_2 in 0.1M PB, 8 minutes in dark
14. Stopping reaction and rinsing: 0.1M PB, 3 x 10 min
15. Inspect sections for labeling in LM (take pictures)
16. Rinsing: 2% sodium acetate (pH 8.7), 3 x 10 min. Use a new 24-well dish
17. Overnight at 4˚C in 10% sodium thioglycolate
18. Proceed as in original protocol for EM (given in A4.3)

IVe Final protocol used for immunohistochemistry for EM

This is the protocol used for the final EM experiments, optimized through testing as described in the methods section. Changes from the protocol in appendix IVd include the time of washing steps, reduction in the number of steps including TrX, inclusion of 1% BSA in the blocking step and in the primary antibody diluent buffer, a reduced concentration of NHS and of the primary antibody, and a shorter DAB-reaction time.

Day 1

1. Rinsing: 0.1M PB, 5 x 7 min
2. Permeabilization: 0.1M PB + TrX, 20 min
3. Rinsing: 0.1M PB, 5 x 7 min
4. Blocking endogenous peroxidase activity: 1% H_2O_2 in 50% MeOH in 0.1M PB, 30 min
5. Rinsing: 0.1M PB, 5 x 7 min
6. Blocking: 90 min

    0.1M PB + 0.05% TrX + 1% BSA + 1% NHS for P15 and P30

    0.1M PB + 1% BSA + 1% NHS for P10

7. Incubation with primary antibody. Diluted 1:40 000 in 0.1M PB + 1% BSA + 1% NHS, overnight (approximately 24 hours) at 4˚C

Day 2

8. Rinsing: 0.1M PB, 5 x 7 min
9. Incubation with secondary antibody. Diluted 1:400 with PB, 2 hours
10. Rinsing: 0.1M PB, 5 x 7 min
11. Incubation with ABC reagent: dilute in 0.1M PB, 1 hour
12. Rinsing: 0.1M PB, 5 x 7 min
13. DAB staining: 0.03% DAB and 0.01 % H_2O_2 in 0.1M PB, 5 minutes in dark
14. Stopping reaction and rinsing: 5 x 7 min
15. Inspect sections for labeling in LM (take pictures)
16. Rinsing: 2% sodium acetate (pH 8.7), 3 x 10 min. Use a new 24-well dish
17. Keep overnight at 4˚C in 10% sodium thioglycolate
18. Proceed as in original protocol

IVf Procedure for counterstaining

4% uranyl acetate in 50% ethanol in sterile water and 1% lead citrate in 0.1M sodium hydroxide in boiled, sterile water is used.

1. Measure uranyl acetate and lead citrate in Eppendorf tubes. Up to six grids can be stained per round.
3. Centrifuge at 12-13 000 rpm for 10 minutes. Balance the centrifuge.
3. Add Parafilm to two petri dishes. Use pipette to place one drop uranyl acetate per grid that is to be counterstained onto the piece of Parafilm.
5. Use tweezers to collect grids from the grid box, place one grid (section-side down) onto each drop of uranyl acetate, cover with non-transparent lid.
6. Stain for 8 minutes.
7. Rinse baths to be used for washing the grids with distilled water. Wash the grids by dipping in four baths of distilled water, approximately 10 seconds per bath.
8. Wipe grids and tweezers with filter paper.
9. Use pipette to place one drop of lead citrate per grid that is to be counterstained onto the other piece of Parafilm.
10. Place one grid (section-side down) onto each drop of lead citrate, cover with lid.
11. Stain for 3-4 minutes.
12. Rinse baths with distilled water again.
13. Wash the grids again by dipping in four baths of distilled water.
14. Wipe grids and tweezers with filter paper.
15. Allow grids to dry for approximately one hour before microscopy.

Appendix V: Recipes for solutions

Stock solution PB 0.4M

Consists of two parts, an acid (A) and a base (B).

Solution A: monosodium phosphate, 0.4M

Solution B: sodium phosphate dibasic, 0.4M

Add solution A to 500 ml solution B until the pH is 7.4. The stock solution can be stored at room temperature up to one month in a dark cabinet.

Stock solution Sørensen's PB 0.3M

19.23 g sodium hydrogen phosphate dihydrate

5.79 g sodium dihydrogen phosphate monohydrate

3.68 g sodium chloride

Add 500 ml distilled water, and mix until the solution is clear. Store in room temperature.

Stock solution TBS 1M (used in original EM protocol, appendix IVc)

For 1 liter:

121 g trizma base

90 g sodium chloride

Add 400 ml sterile water

Adjust to pH 7.4 with 32% hydrochloric acid, then make volume up to 1 liter with sterile water.

Store at 4˚C.

Incubation medium (used in original EM protocol, appendix IVc)

1% BSA

0.1% glycine

0.1% lysine monohydrochloride

0.1% cold water fish gelatin

0.05% TrX

1% NS

DAB 3% stock solution

Add 0.15 g DAB powder to 5 ml water. Add concentrated hydrochloric acid, one drop at a time until the solution is clear. Store in freezer.

Working solution is 0.03% DAB in 0.1M PB, to which 0.01% H_2O_2 is added immediately prior to use.

Silver development solution

Solution A:

5% sodium carbonate in MQ water

Solution B:

50 ml boiled MQ water

0.1 g silver nitrate

0.1 g ammonium nitrate

0.5 g tungstosilicic acid (TSA)

Dissolve first silver nitrate in boiled MQ water. Add ammonium nitrate and TSA.

Solution C: 37% Formaldehyde (contains 10-15% methanol)

For working solution, add 10 µl of solution C to 2.5 ml of solution B under vigorous stirring. Add drops of solution C + B to 2.5 ml of solution A under continuous stirring. The solution should be clear and transparent, and is only stable for 30 minutes.

Epoxy resin

153.4 g LX-112 resin
81.1 g DDSA
65.5 g NMA

Mix thoroughly until the mixture is homogenous and store in freezer. Prior to use, add 0.15 ml DMP-30 for every 10 ml epoxy resin.

Appendix VI: List of antibodies, sera, and chemicals

Antibodies and sera	Manufacturer	Product no.
Goat anti-parvalbumin	Swant	PVG-214
Horse anti-IgG (biotinylated)	Vector Laboratories	BA-9500
Normal horse serum	Sigma	H-0146

Chemicals	Manufacturer	Product no.
3, 3 Diaminobenzidine tetrahydrochloride	Sigma	32750
Acetic acid	Merck	100063
Acetone	VWR Chemicals	20063.365
Ammonium nitrate	Sigma	A9642
Avidin-biotin complex kit	Vector Laboratories	PK-4100
Cold water fish gelatin	Sigma	G7041
Bovine serum albumin	Sigma Aldrich	1001927547
DDSA	Chemi-Teknik	21850
DMP-30	Chemi-Teknik	21370
LX112	Chemi-Teknik	21650
Ethanol	Kemetyl Norge	
Formaldehyde	Sigma	F1635
Porcine skin gelatin	Sigma	1000722767
Glutaraldehyde	Chemi-Teknik	16310
Glycine	Merck	1.04201.0250
Gold chloride	Merck	1582
Hydrochloric acid	Sigma Aldrich	258148
Hydrogen peroxide	Sigma	316442
Lead citrate 3-hydrat	Chemi-Teknik	17800
Lysine monohydrochloride	Sigma	L-5625
Methanol	Sigma Aldrich	101309083
Monosodium phosphate	Sigma Aldrich	71504
NMA	Chemi-Teknik	20800
Sodium phosphate dibasic	Sigma Aldrich	71645

Osmium tetroxide	Chemi-Teknik	19110
Paraformaldehyde	Merck	1.04005.1000
Phosphate buffered saline	Oxoid	BR0014G
Potassium ferrocyanide trihydrate	Sigma	P3289
Sodium chloride	Merck	1.06404.1000
Silver nitrate	Merck	1.01512.0025
Sodium acetate	Sigma	S8750
Sodium carbonate	Merck	6392
Sodium cacodylate trihydrat	Sigma Aldrich	101537318
Sodium dihydrogen phosphate monohydrate	Merck	1.06346.1000
Sodium hydrogen phosphate dihydrate	Merck	1.06580.1000
Sodium thioglycolate	Sigma	T0632
Sodium thiosulphate	Sigma	72049
Tissue mount	Sakura	SAK1467
Toluidine blue	Merck	1.15930.0025
Tris (hydroximethyl) aminomethane	Merck	1.08382.0500
Triton X-100	Chemi-Teknik	22140
Tungstosilicic acid	Merck	10659
Uranyl acetate 2-hydrat	Chemi-Teknik	22400